# DOCTORAL THESIS

# Microstructural Classification of Al-Si Casting Alloys with Machine Learning Techniques

（機械学習技術による Al-Si 鋳造合金の微細構造分類）

**Zixiang Qiu**

**邱 子翔**

***March 2023***

# Microstructural Classification of Al-Si Casting Alloys with Machine Learning Techniques

（機械学習技術による Al-Si 鋳造合金の微細構造分類）

**Zixiang Qiu**

**邱 子翔**

**Advisor: *Prof.* Kenjiro Sugio**

**指導教員：杉尾　健次郎**

***Department of Mechanical Science and Engineering***
***Graduate School of Engineering***
***Hiroshima University, Japan***

***March 2023***

# CONTENTS

# List of Figures

# List of Tables

# *Chapter 1*

## Background and Objectives

## 1.1 Introduction

Economic and environmental requirements make it increasingly important to reduce the weight of vehicles.[1-3] The specific gravity of aluminum is about 1/3 that of steel, and even when rigidity is taken into account, it is 1/2 that of steel. aluminum is therefore a very effective lightweight material, and its applications are expanding.[4-8] Aluminum alloys with Si as the main alloying element are the most important component of all cast manufacturing materials in this category.[9-13] Due to their combination of excellent castability and better mechanical properties, as well as their outstanding corrosion and wear resistance, aluminum and silicon casting alloys are widely used to produce automotive parts that operate in high temperature environments (up to 200 ºC). Copper and magnesium are often added to such alloys to improve strength at room and high temperatures and to make heat treatment possible.[9, 11, 14-19] The microstructure of these cast alloys is dominated by α-Al dendrites decorated with eutectic silicon particles and many intermetallic phases such as $Al_2Cu$, $Mg_2Si$ and Fe-bearing phases.[20-22] The size, morphology and distribution of microstructural features of the cast alloys determine the mechanical properties of the alloys. Microstructural characterization and analysis are fundamental to materials science, linking material structure to composition, process history and properties. Traditionally, microstructure quantification requires a human to decide what to measure and to design a measurement method to measure it. However, there are many microstructural analysis tasks that require human judgment and are therefore inherently subjective, difficult to automate, and prone to bias.

With the development of computer technology, artificial intelligence and related techniques are applied in various industries, and great progress has been made in techniques to extract the necessary information from large-scale data and to classify it automatically. One of these techniques is machine learning.[23, 24] Machine learning is a research topic in artificial intelligence where computers learn from data iteratively to find patterns in the input data that are relevant to the data. Machine learning allows us to extract pattern information from the input data and predict which category it belongs

to. If we can create a classifier that can perform advanced pattern recognition, it will be very useful as it can be applied to various fields such as fingerprint recognition and speaker recognition. Over the years, many researchers have designed and built such pattern recognition machines. As a result, various pattern recognition techniques, such as character recognition and face recognition, have been put into practical use and reached commercial levels.[25] In recent years, as machine learning research has intensified and the technology has become more widespread, more and more materials scientists are applying machine learning to materials science to improve material processing parameters and to assist in microstructural characterization as well as to try to predict mechanical properties.[26-34] This is expected to greatly accelerate future advances in materials science, including more efficient development of new materials, effective identification and differentiation of microstructures, and fabrication of high-performance materials by optimizing material properties.

## 1.2 Aluminum-silicon based casting alloys

Si is one of the most important alloying elements in Al-Si casting alloys.[35, 36] The hypoeutectic Al-Si alloy is when the Si content between 5 and 12 *wt.%* of the alloy. Silicon contributes significantly to the wear resistance of the alloy, the reason of which is that Si is consisted as a very hard phase. Si also improves the casting properties of the alloy, allowing the alloy to easily fill the mold and harden the casting without thermal cracking or thermal cracking problems. The more Si in an alloy will cause the lower coefficient of thermal expansion. Si, in combination with other elements, increases the strength of the alloy while making it heat treatable.

Si content in Al-Si based casting alloys affects tensile properties at room and elevated temperatures. This effect is more pronounced without alloying elements such as Cu, Mg, Fe, and Zn, etc. The strength contribution of Al-Si alloys is attributed to load transfer from the α-Al matrix to the strong, highly interconnected eutectic Si plate-like structure. The spheroidization can reduce the load carrying capacity of the eutectic Si, which improves the machinability, ductility, and fatigue resistance of the alloy. When Al-Si cast alloys are exposed to high temperatures, the eutectic silicon particles decompose, becoming spherical and coarse, with a reduced aspect ratio and loss of interconnectivity of the eutectic phase. The rate of loss of interconnectivity is highly dependent on temperature and exposure time. Increasing Si content from 7 *wt%* to 12 *wt%* in low-alloy element Al-Si casting alloys has been reported to increase yield strength and ultimate tensile strength to 22 MPa and 25 MPa at the temperature of 250ºC, respectively.[37]

Cu and Mg are two important alloying elements that widely added to Al-Si casting alloys. The additive of them not only increase the strength of the alloy at room and up to 190 ºC high temperatures, but also make it responsive to heat treatment. These kinds of alloys have wide range of applications, from automotive industry to aerospace structural parts.[36, 38] For example, compressor pistons, engine cooling fans, crankcase, compressor housings and mechanical components such as timing gears and rocker arms.

The major alloy strengthening phases are including $Al_2Cu$, $Mg_2Si$ and $Al_2CuMg$. When the alloy exposed to high temperatures, usually above 200 ºC, these phases become unstable and tend to coarsen rapidly and subsequently decompose, causing the products made by the alloys to be unsuitable for very high temperature applications.[39)]

Both of the additions of Mg and Cu are associated with improved tensile properties and the creep resistance of Al-Si alloys at high temperatures of up to 200ºC.[7, 39)] Therefore, Mg could also reduce the rate of strength loss of the alloys at high temperatures. After solid solution treatment, the high-temperature strength is significantly improved due to precipitation hardening activated by the magnesium-containing phase. The increase in the high-temperature strength of the Mg-containing alloy can be attributed entirely to the precipitation of β-$Mg_2Si$ in the second phase.[39)]

### 1.2.1 Solidification and microstructure of Al-Si alloys

The classical microstructure of an Al-Si casting alloy is shown in Fig 1.1. Solidification occurs from primary crystallization of Al phase (α-Al), with the dendritic α-Al embedded in Al-Si eutectics. In hypoeutectic Al-Si alloys, they are solidified as primary Al dendrites growing along the <100> direction. For cubic crystal systems, there are four auxiliary arms growing around the main axis at each connection, which are often referred to as dendrites.[40)] The degree of undercooling depends on the cooling rate, the concentration of alloying elements in the melt, and the type of alloying elements. The degree of subcooling is known to increase with cooling rate and alloying element concentration.[41)]

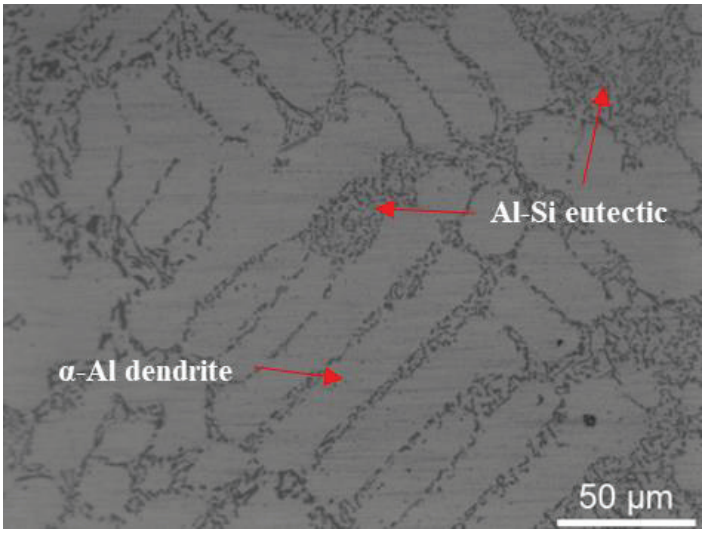


Fig. 1.1 Solidification structure of hypoeutectic Al-Si alloy.

Al-Si eutectic formation marks the beginning of the alloy's next stage of solidification. Both the Al and Si phases crystallize out of the liquid at the same time during eutectic solidification while maintaining in a constant temperature (eutectic temperature).[42] Fig. 1.2 provides the phase diagram of the Al-Si system with a eutectic point. The eutectic temperature is 577 °C, and the eutectic point is 12.2 wt% Si. Eutectic alloys provide a natural composite material that gives the alloy good properties.[42] In addition to Si, commercial aluminum alloys often incorporate the alloying elements Cu and Mg. These alloys' eutectic properties could be more complicated than what can be seen by analyzing binary systems. Following eutectic development, intermetallic compound phases with Cu and Mg are frequently formed.

Al-Si cast alloys include a α-Al primary phase and a eutectic Al-Si phase in the microstructure. The quantity of eutectic in the microstructure is dependent on the amount of silicon present, and eutectic is made up of hard Si particles embedded in a soft Al matrix. After the modification procedure, the Si particles' plate-like morphology could be improved. Numerous intermetallic compounds can be formed in the alloy's microstructure as a result of the inclusion of Cu, Mg, and Fe. Therefore, $Al_2Cu$, $Mg_2Si$, and β-$Al_5FeSi$ are the three most prevalent intermetallic compounds.[13]

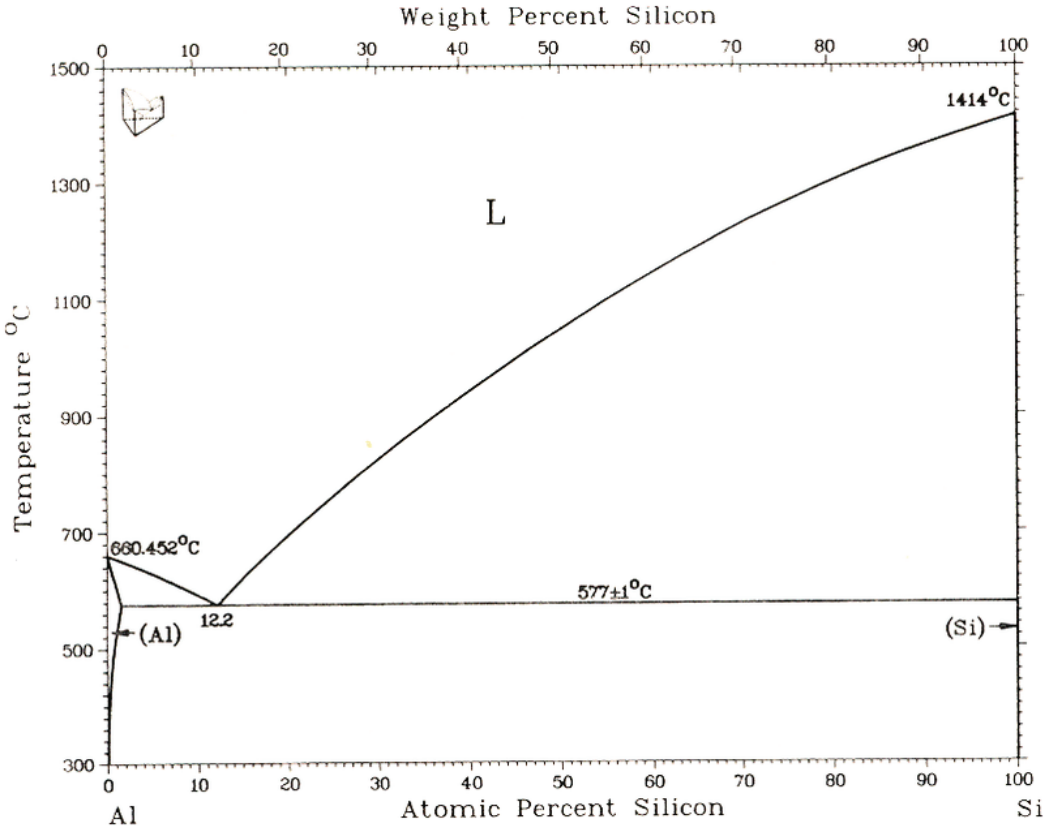


Fig. 1.2 The schematic phase diagram of Al-Si.[43)]

### 1.2.2 Cooling rate refinement and mechanisms

The size, morphology, and distribution of each microstructural component are significantly influenced by the cooling rate. Increasing the cooling rate refines the size of all microstructural features, reduces secondary dendrite arm spacing (SDAS), changes the morphology of eutectic Si from large, elongated plates to small, round plates, and reduces the size of all intermetallic compounds, regardless of their type. The eutectic Si particles are refined by the faster cooling rate, but their plate-like morphology is not changed.

As one of the widely accepted theories of quench modification, the refinement of the cooling rate of eutectic Si particles is explained on the basis of surface energy at the Al-Si solid interface. This theory states that the rate at which the solidification interface progresses depend on the balance between the heat flow velocity from the liquid through the interface to the solid and the latent heat of fusion released during

solidification. This theory explains the formation of modified eutectic structures at high cooling rates.[44] The thermal conductivities of pure Al and Si are 205 and 83 W/(mK), respectively, and their latent heats of melting are 396 and 1411 J/g. The solidification rate of Al is much faster than that of Si because of the large difference in the magnitude of the thermal conductivity of pure Al and Si and the magnitude of the latent heat of melting of pure Al and Si. Therefore, Al acquires lead during eutectic solidification as shown in Fig. 1.3 (a). As the cooling rate increases, the leading of Al to Si increases, resulting in the lagging Si crystals being completely wrapped by the advancing Al, as shown in Fig. 1.3 (b) and (c).

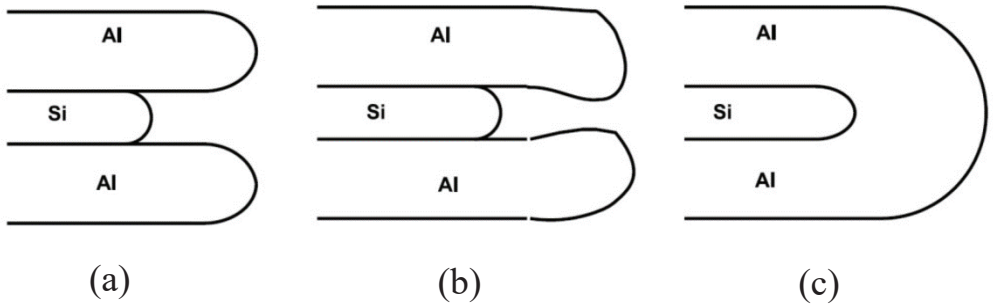


Fig. 1.3 Eutectic solidification in unmodified cast aluminum-silicon alloys.[44]

### 1.2.3 Modification of eutectic silicon

One of the methods to improve the mechanical properties of Al-Si casting alloys is the metamorphism method. Since the Al-Si eutectic has a hard and brittle Si phase in a soft Al matrix, the mechanical properties of the casting, especially the elongation at break, are mainly determined by the eutectic structure. Modification refers to the addition of an inoculant in the form of a master alloy to molten Al to promote the formation of a fine fibrous eutectic Si structure during solidification. To modify a plate-like Al-Si eutectic (Fig. 1.4a) into a fine coralline-like Si structure (Fig. 1.4b), there are two kinds of methods: addition of specific elements (chemical modification) and quenching (quenching modification). Several modifiers (such as Sr, Na, Sb, Ba, and Ca, *etc.*) are known for modification of the alloys. Moreover, Sr has the advantage of being easy to handle and effective as well as having a low discoloration effect compared to several

other modifiers. For these reasons, Sr has become the most used additive as a chemical modifier in the aluminum alloy industry in recent years. The addition of hundreds of ppm Sr changes the morphology of eutectic Si from coarse flakes to fine fibers, and the fracture mode changes from crystalline penetration and brittle fracture to crystalline gap and dendrite fracture, which is beneficial for both strength and ductility.

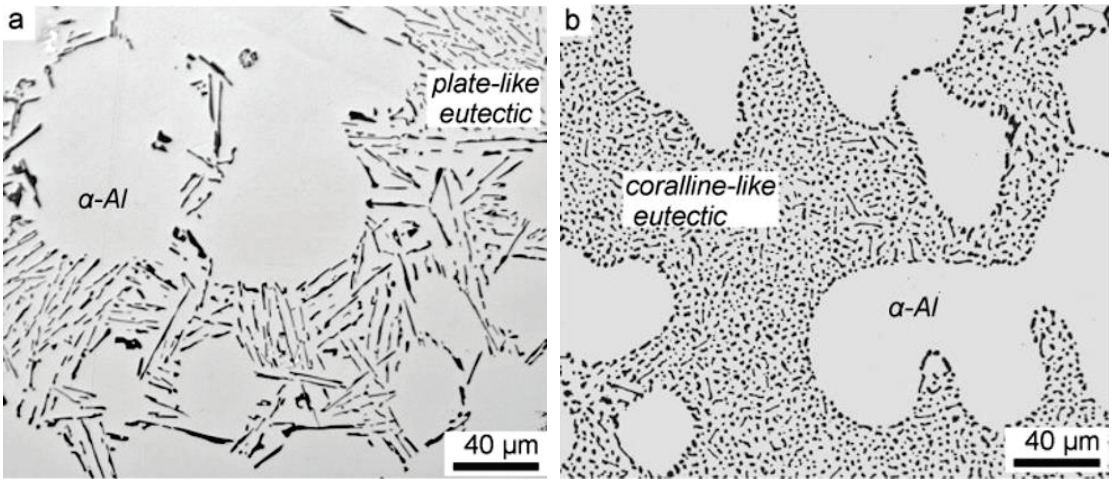


Fig. 1.4 The morphology of eutectic Si; (a) Unmodified and (b) Modified structure.[45)]

In hypereutectic compositions (Si content above 12.2 wt%), the addition of phosphorus to the molten alloy greatly affects the distribution and morphology of the primary Si phase. It has been shown that keeping trace P concentrations between 0.0015 and 0.03% effectively produces microstructures. There is no known element that can favorably modify only the eutectic and hypereutectic phases. Modifications are thought to alter the number, nature and distribution of voids. Although not widely accepted, many studies have shown that modification tends to increase porosity, which is closely related to casting parameters, and this is one of the obstacles to eutectic modification as a method of improving the mechanical properties of castings. The addition of large amounts of modifiers (Na > 0.02 *wt%* and Sr > 0.1 *wt%*), called over-modification, usually results in the formation of $Al_2Si_2Sr$ brittle compounds and reduces alloy properties. There is another reason why eutectic modification does not guarantee that the properties of Al-Si alloys are necessarily improved, namely the presence of other undesirable compounds, iron-rich intermetallic compounds for example, and casting

defects that can negatively affect the alloy properties. Several techniques have been used to assess the extent of eutectic silicon modification in aluminum alloy casting alloys, including metallographic studies, thermal analysis, and methods based on physical properties of the alloy. While the assessment based on cooling curve analysis has been presented as the most accurate and non-subjective technique to achieve this purpose.[46)]

#### 1.2.3.1 The growth mechanism of lamellar silicon

For the purpose to understand the mechanisms of eutectic silicon modification, quenching and chemical modification, one must have prior knowledge of the growth mechanism of unmodified pre-sheet silicon. Most theories explaining modification are premised on the assumption that the growth mechanism of silicon has changed. Therefore, the modification theory remains incomplete unless the growth process of lamellar silicon is fully understood. However, the exact growth mechanism of lamellar silicon is still controversial. The following describes the currently accepted and more plausible growth mechanism of lamellar silicon, followed by a theory of possible modification mechanisms.

##### 1.2.3.1.1 Two-plane re-entry edge (TPRE) mechanism

TPRE mechanism was first used to describe the growth of germanium dendrites and was later extended to the growth of silicon. The equilibrium habit of silicon is an octahedron with eight (111) planes around it. The twins are half of the equilibrium crystal, and the planes along which the twins are composed are reflected in the rest of the solid. Thus, the external shape of a twinned silicon crystal consists of six edges where the paired (111) planes intersect, as shown in Fig. 1.5 (a). The outer planes between these boundaries are 141° and 219°. The boundary plane forming the 141° outer angle forms a concave angle, while the boundary plane forming the 219° outer angle forms a ridge. The re-entrant angle is the preferred nucleation site compared to the ridges, because the binding of atoms to the re-entrant angle is more favorable than the binding by joining the ridges.[47)]

Therefore, a rapid growth along the [211] direction is possible because of the presence of the re-entrant corner. But when a triangular solid completely surrounded by ridges is formed, the rapid growth at the re-entrant corner stops, as shown in Fig. 1.5 (b). However, at the situation of Fig. 1.5 (c), the crystal containing two twins instead of one, then there are six re-entrant angles along the [211] direction. As shown in Fig. 1.5 (d), the growth of the re-entrant angles generates more reentrant angles and the newly generated reentrant angles alleviate the blockage of the nucleation sites by the formation of ridges. Fig. 1.5 (e) shows the simultaneous growth of an entity with multiple steps through the reentrant edge mechanism. The TPRE mechanism was then experimentally verified to be responsible for the growth of germanium dendrites.

#### 1.2.3.1.2 Layer growth mechanism

Si crystals are materials with high melting entropy and tend to form atomically smooth and dense interfaces during solidification. Thus, if atoms moving away from the liquid attach to a flat solid surface, the interfacial energy increases and the atoms may jump back into the liquid. However, as shown in Fig. 1.6, if a ledge is present at the interface, the liquid atoms can easily bond with the solid without increasing the interfacial energy. Flake form silicon is grown mainly by a layer growth mechanism. The average spacing of the twins was measured and was found to be between 0.4 and 1.0 μm for the slowly cooled samples. It was observed that this twinning spacing was much larger than expected from the TPRE mechanism. TEM microstructure analysis showed that twinning occurred in the non-surface portions of the silicon crystals, without the formation of re-entrant edges or grooves. Although the layer growth mechanism explains the growth after ledge formation, the layer nucleation mechanism is also important. Screw dislocation is one of the main reasons for nucleation of new layers. The study of the effect of screw dislocations on the nucleation of new layers and their interaction with re-entrant edges suggests that the ubiquitous helical dislocations in real crystals need to be taken into account when studying the growth mechanism of faceted

crystals. Therefore, in Fig. 1.7 shows four cases that can be considered depending on the presence of screw dislocations and twin junctions on the crystal surface.[44)]

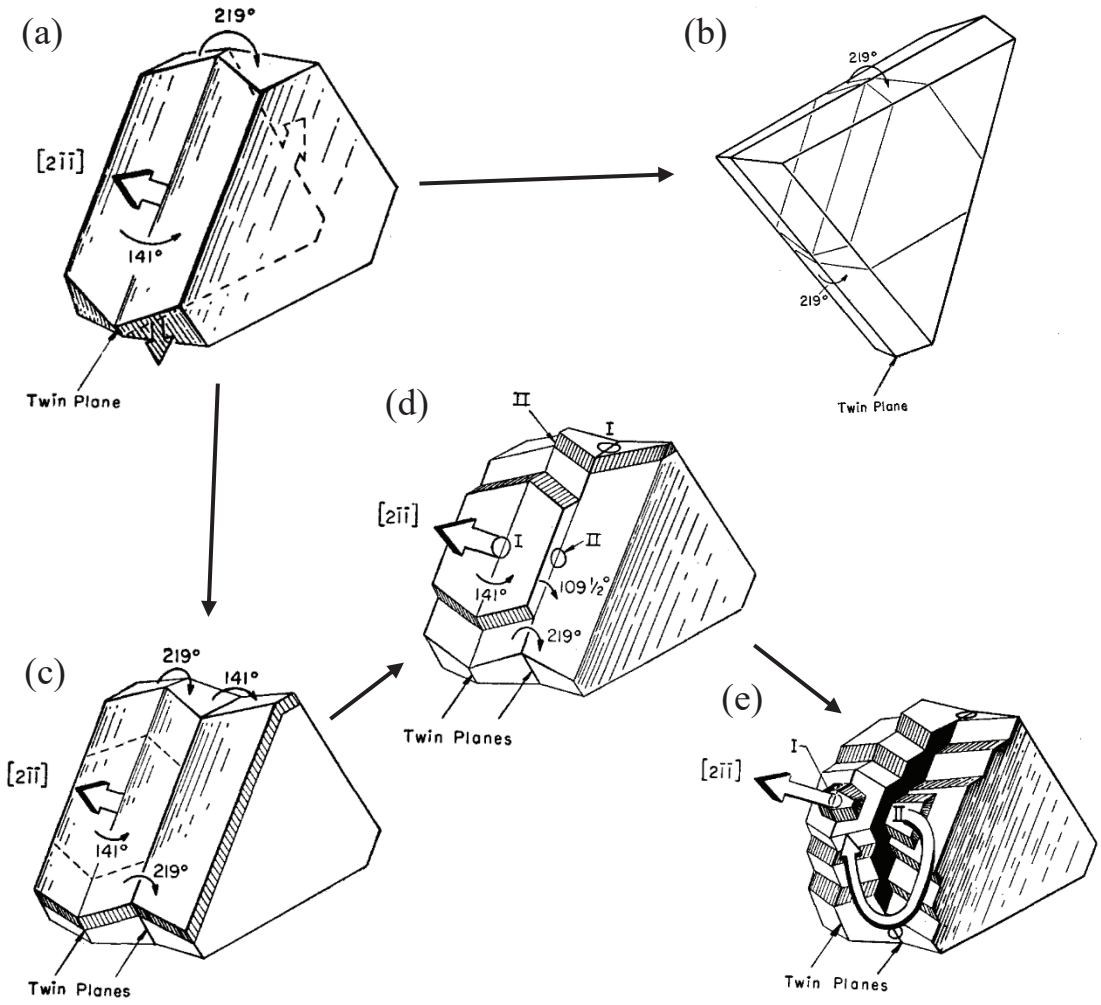


Fig. 1.5. Schematic of TPRE Mechanism: (a) Crystal with a single twin, (b) Closure of twins due to ridge formation, (c) Crystal with two twins, (d) Creation of extra re-entrant corners I and II, and (e) Propagation of crystal due to re-entrant corners.[47)]

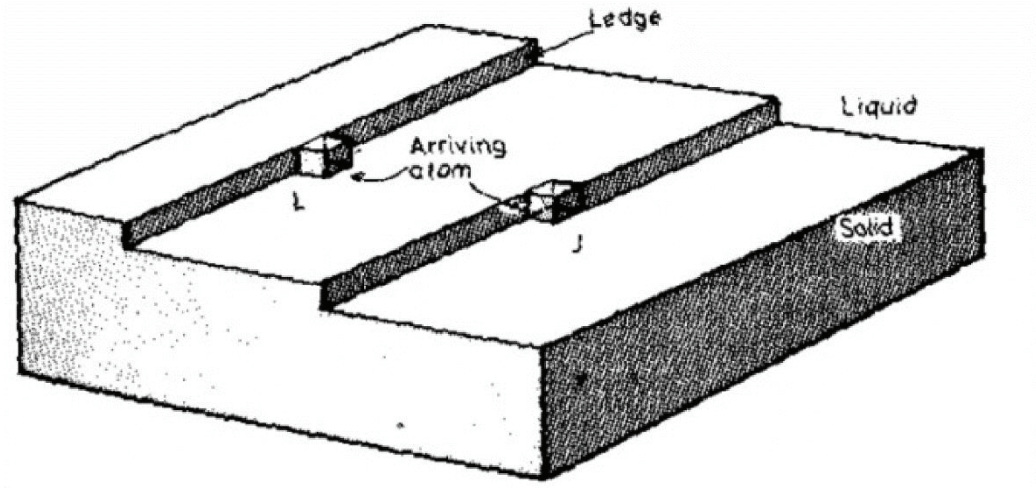


Fig. 1.6 Layer growth mechanism of atomically smooth interfaces by formation of ledges.[48)]

Kink, step, re-entrant corners, and surface nucleation are basically four preferential growth sites in a given faceted crystal. In Fig. 1.7 (a), there are no surface-exposed screw dislocations in both twinned crystals and crystal surfaces. Therefore, the effective growth mechanism in this case is the TPRE mechanism. Screw dislocations are exposed in the twin-crystal part and grow preferentially in the twin-crystal part in the case of Fig. 1.7 (b). In this case, the crystal grows forward and backward. The screw dislocations are exposed on the crystal surface, as shown in Fig. 1.7 (c). In this case, the screw dislocations act as the origin of the surface-shaped nuclei, so the entire surface of the crystal grows uniformly and the TPRE mechanism does not contribute to the growth. Fig. 1.7 (d) shows the case where the helical dislocations are exposed to the twin junction and the crystal surface. Crystal growth depends on the density of helical dislocations at the surface and at the twins in this situation. If the density of screw dislocations at the twin junction is higher than at the crystal surface, growth occurs preferentially along the twin junction, resulting in crystals similar to those grown by the TPRE mechanism.

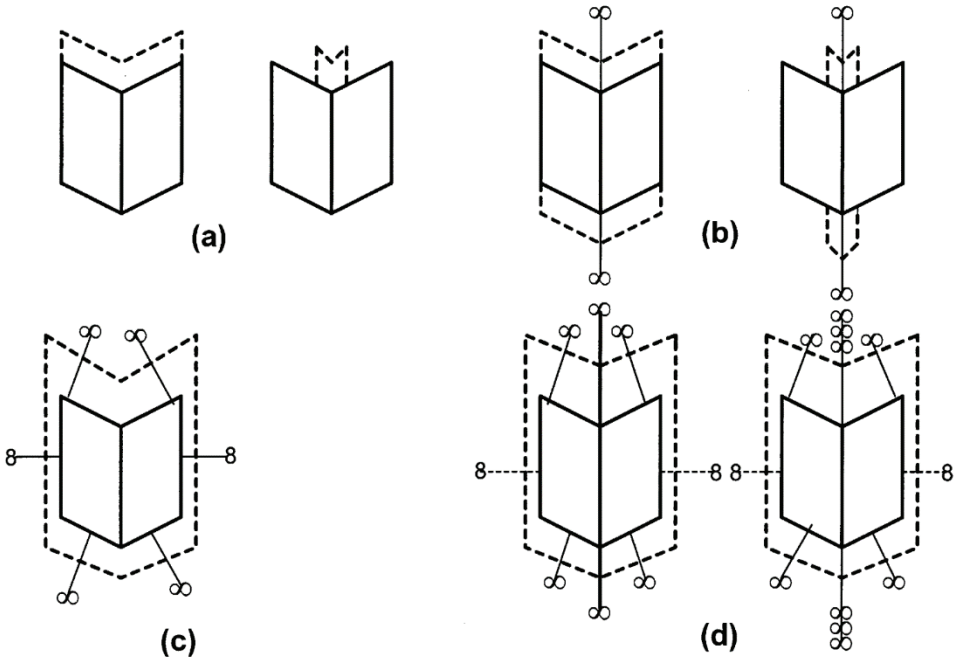


Fig. 1.7 Hypothetical conditions of a screw dislocation and a re-entrant corner.[44)]

#### 1.2.3.2 Modification Theory

Recently, most theories explain that the process of modification is caused by the presence of impurity atoms in the melt that restrict the growth of silicon. However, in such theories there are different views on how impurity atoms affect silicon growth, and thus a number of possible mechanisms have been proposed, including changes in surface energy, TPRE poisoning, and growth ledges.

##### 1.2.3.2.1 Surface energy theory

This theory is one of the widely accepted theories of quench modification that attempts to explain chemical modification of Al-Si eutectic in terms of surface energy at the Al-Si solid interface, although there are still many arguments in favor of chemical modification.[49)] As shown in Fig. 1.8, the addition of chemical modifiers decreased the surface energy of the Al-Si solid interface and increased the interfacial angle $\theta$. This inhibited the growth of Si crystals, leading to changes in the eutectic structure and subcooling. It was subsequently demonstrated that reduction of the surface tension of the eutectic liquid was because of the sodium addition. The growth of Al-Si eutectic

alloys on polycrystalline silicon substrates was compared in the presence and absence of sodium atmosphere, in order to investigate the effect of this change in surface tension on the interfacial angle. In the presence of Na, no change was recorded, but the importance of the apparent difference between the non-negligible surface tensions is still under discussion.[44)]

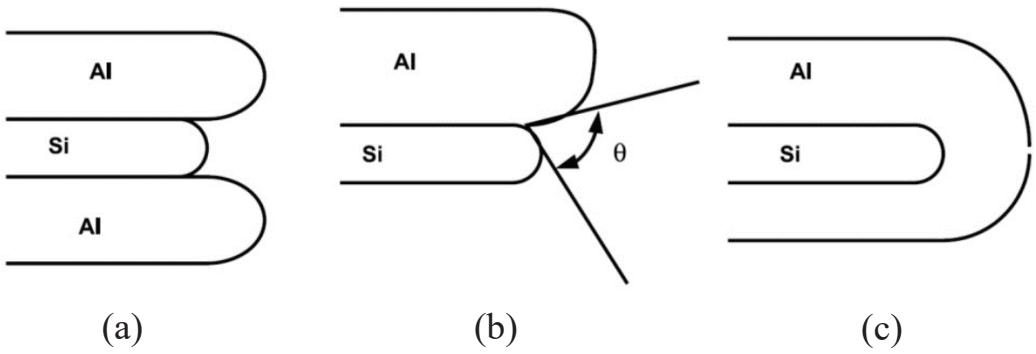


Fig. 1.8 Eutectic solidification in sodium modified Al–Si alloys.[44)]

#### 1.2.3.2.2 Theories of interfacial poisoning

These theories describe the way in which chemical modifications poison the Si growth sites when impurity atoms (e.g. Na, Sr) start to progress at the interface. There are two different groups of views on the theory. One believes that the interfacial poisoning of Si at the interface leads to a reduction in the growth rate of Si. The other group suggests that the poisoning of the modification atoms at the reentrant edge may hinder growth through the TPRE mechanism.[44)]

A group of researchers proposed that the interfacial poisoning of the modification atoms on the re-entrant edge of the TPRE mechanism is responsible for the modification, which is called TPRE poisoning. The typical growth of Si is sawtooth-like. Examination of the electron diffraction pattern of the fibers shows the growth mechanism shown in Fig. 1.9. The lower part of the AB twinning diagram on the left branches out into BC twinning through multiple twinning. In addition, the AB twin is in the [112] direction and the BC twin is in the [112] direction.

Due to the poisoning of impurity atoms, the fibers are oriented by multiple twins, usually in a coral-like morphology. This hypothesis of TPRE poisoning mechanism does not accurately predict how poisoning at the reentrant edge occurs and which features determine whether an element can act as a modifier.[50)]

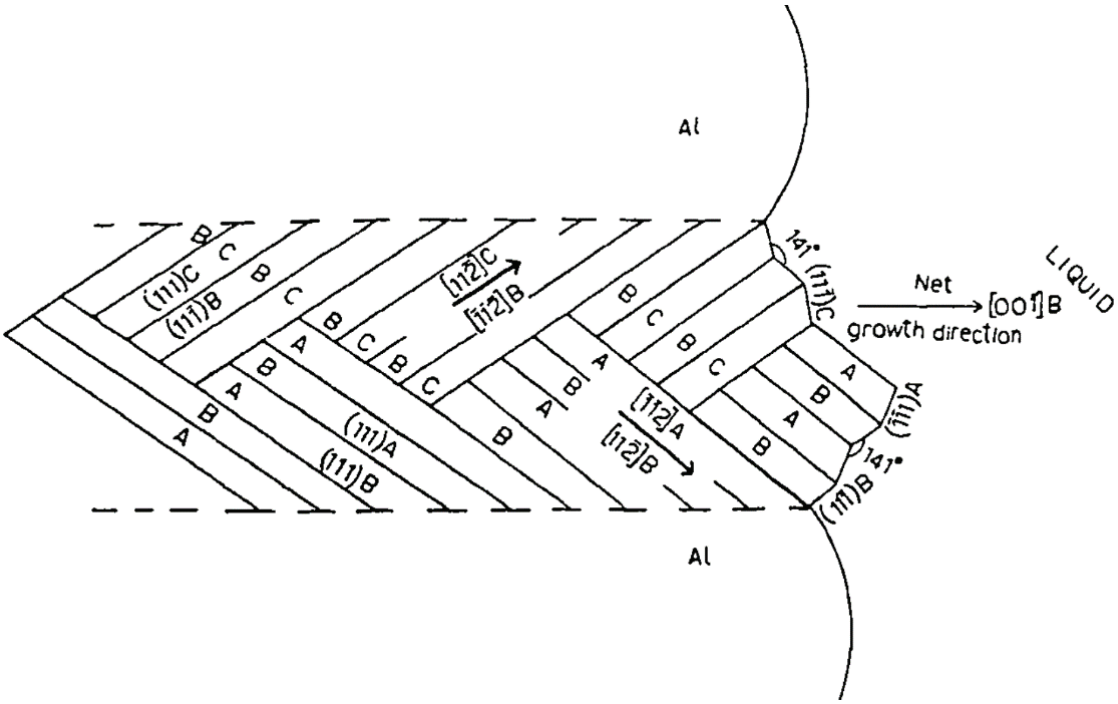


Fig. 1.9 Schematic diagram of twins and their growth directions in a modified Si fiber.[50)]

In the theory of instability-induced twinning, interfacial contamination occurs by contaminating the growing edges of silicon. Impurity atoms, such as Na or Sr, act as poisons to the already growing atomic layers. As shown in Fig. 1.10, it is believed that impurities adsorb to steps or twist points and prevent atoms or molecules from attaching to the crystal. These poisoned atoms can induce twinning by changing the stacking order of the atomic layers in order to grow around the impurity.[51)]

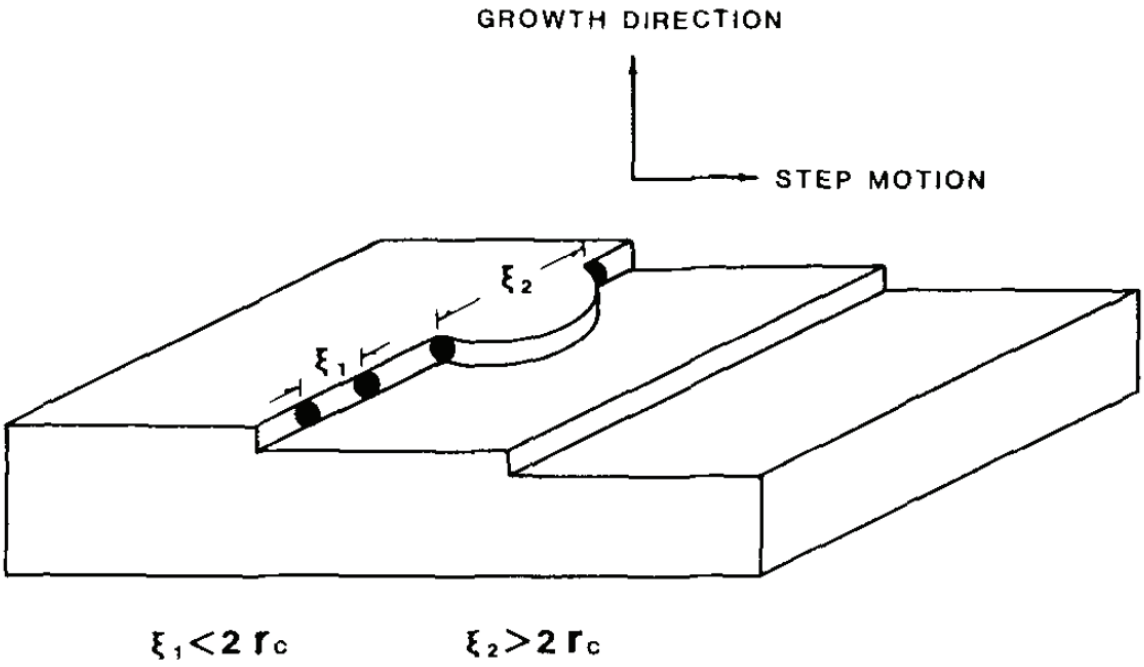


Fig. 1.10 Schematic view of impurity atoms pinning the steps of a Si crystal growing by the layer growth mechanism at the solid/liquid interface.[51)]

### 1.2.4 Aging treatment

Casting is commonly used to produce aluminum alloys for machine parts, and the die-casting method is one of the main methods, especially for the production of automotive parts. Die casting is a method of solidifying molten metal with a cooled mold under high pressure. After the automobile parts are manufactured by die-casting method, in order to improve the strength, it is often used in the solid solution treatment followed by water quenching and then artificial aging heat treatment method (T6 treatment) before it will be used for the product.

In 1906, Germany's A. Wilm first discovered the aging hardening phenomenon of aging treatment. Age hardening is mainly due to precipitation strengthening by the formation of fine precipitates in the matrix during heat treatment. Precipitation strengthening is a method of strengthening obtained by heat treatment, such as solution treatment, quenching and aging, which causes fine precipitates to disperse in the matrix and become a single-phase at high temperatures and a two-phase alloy system at low temperatures. These precipitates are diffusive phase changes that occur through the

diffusion of solute atoms in the solid. In age-hardened aluminum, fine metastable phases, such as the GP zone and intermediate phases, form in the early stages of aging. These metastable phases often induce coherent strains, are highly resistant to dislocation migration, and strengthen the alloy. In general, in the Al-Si-Mg alloy used in this study, the GP zone is first formed from the supersaturated solid solution after solution treatment, followed by the formation of the β" (needle-like GP zone). With further development of aging, the β' phase is formed, followed by precipitation of the stable β phase (cubic crystalline $Mg_2Si$). Here, the clusters or GP zones are essentially aggregates of solute atoms, which are typically about 2 to 20 nm in size. Therefore, it is difficult to determine the structure by X-ray diffraction techniques and it is not possible to obtain information about the composition. A high-resolution transmission electron microscope (TEM) is required to observe and analyze the structure of the precipitates. Furthermore, after the mid-aging period, the concentration of the matrix reaches almost constant, the volume fraction of the precipitates remains almost constant and the precipitates become coarser while competing with Ostwald growth. Ostwald growth is a phenomenon in alloys where particles of different sizes are dispersed in the matrix, where small particles shrink and disappear and large particles grow.

In order to evaluate the current aging treatment, it is necessary to observe the precipitates through nanoscale microstructure observations, such as TEM observations, which require a lot of time and effort. On the other hand, if big data can be constructed by applying machine learning-based image recognition techniques, it can be argued that the alloy selection and evaluation process, which traditionally requires labor and experience, can be significantly shortened. Therefore, in this study, as a first step, machine learning-based image classification techniques were applied to the microstructure of Al-Si-Mg alloys subjected to T6 treatment and changes in the microstructure of the alloy accompanying the solid solution treatment and aging process were identified. The aim is to verify if this is possible. If quantitative identification is made possible by machine learning-based image classification techniques, it will be possible to improve the efficiency of the material production line.

## 1.3 Application of machine learning in microstructure analysis

With the development of computer science, especially the fields of artificial intelligence, machine learning is becoming an important tool for materials scientists and engineers to accelerate the development of new materials, processes and technologies. To accomplish high-throughput identification and quantification of critical aspects in the process-structure-property chain is one of the goals of utilizing such approaches in materials science.[26] Machine learning as a scientific field is still new and changing as a result. Many of the techniques and algorithms used are already known, but new methods have matured in recent years, which makes machine learning considered a new field, even though it has existed for quite some time. As a result, the definition of machine learning as distinct from descriptive statistics remains vague. As data-driven approaches are being accepted in fields such as materials science, new variants and adapted machine learning methods are being designed and adapted to the unique challenges and data profiles of materials science.

### 1.3.1 Data mining and machine learning

Velichko *et al.* propose a new method for classifying microstructures using data mining methods.[52] Data mining is the process of discovering knowledge from a data set. It brings together all the analytical steps needed to identify interesting trends and patterns in the data, including data preparation and modeling. Depending on the research objectives, different models can be constructed. Standard evaluation and statistical procedures are needed to properly interpret these models.[53] In their study, Velichko and colleagues used support vector machines (SVM) as classifiers to classify cast iron in different graphite forms using data mining methods. SVMs are binary classification algorithms that allocate newly created unlabeled/labeled data to various classes using input and output labeled data from various classes. Basically, optical micrographs of numerous reference samples were used to deduce morphological features, and data mining algorithms were used to evaluate massive amounts of data. This allows the identification of trends, clusters or anomalies in the data, and relationships between

morphological parameters that can be used to characterize graphite morphology and derive classification models. When the model was evaluated using independent samples, the classification accuracy for the majority of the various graphite morphologies reached 95%.

The study by DeCost and Holm showed that by using a SVM model for each image category, seven different materials with visual properties could be classified (ductile iron, gray iron, malleable iron, annealed baryons, brass hyper-eutectic steel, and high temperature alloys). Their classifier system achieved a cross-validation accuracy of 83%.[54)]

Unlike classical metallographic procedures, data mining methods have the advantage that there is no room for subjective interpretation of microstructures. Liu *et al.* used a similar data mining-based approach for the classification of complex steel structures.[55)] In their study, a workflow was developed using a nearest neighbor (kNN) classifier and pixel-based parameters to classify steel using optical microscopy images of single-phase pearlite samples and mixed microstructure samples. For both types of steels, good agreement was found in terms of phase fraction compared to manual classification results. In the case of pearlite, there was no classification workflow, so the manually created structures were tested with the first method with an accuracy of 93.8%.

The aim of the work of Gola *et al.* was to demonstrate that the data mining process combined with traditional microstructural parameters can be used as a means to objectively classify the microstructure of ferritic matrix duplex stainless steels, using support vector machines as classifiers. The structure of the data mining process, the different preprocessing and data and partitioning options are described. In contrast to the graphitic morphology of cast iron, the typical microstructure of steel is more complex due to the presence of substructures. Therefore, morphological features that were extracted from optical and electron microscope images served as the basis for the classification. The model is trained using a lot of data in order to achieve a high level of generalization. The model is initially trained using a database made up of several structures and objects that represent various kinds of microstructures. The results

demonstrated the feasibility of data mining techniques for the objective classification of various steel structures based on morphological features.[56)]

In addition to data mining, deep learning methods can also be applied to microstructure classification. For example, automatic microstructure recognition was achieved by Chowdhury *et al.* A case study of an image-driven machine learning approach. Dendritic morphology is particularly relevant for classification with minimal prior expertise. As a result, the expected knowledge gain is claimed to be comparable to human performance, but not better. The first classification task is to distinguish between dendritic and non-dendritic microstructures. The second classification task aims to determine the orientation of longitudinal and transverse dendrites by means of a continuous binary classification task performed in cross-section. Images consisting of different materials of various sizes were used as initial data input. The micrographs are represented as feature vectors by feature extraction and dimensionality reduction. Different classification models are trained, validated, and tested using these feature vectors. They are made up of a collection of features depicted in the images. A high-dimensional feature vector is used to represent an image, as shown in Fig. 1.11. Feature selection is used to increase computing efficiency by reducing the feature vector while retaining all crucial image information (e.g., reducing the sparsity of the vector). Different dimensionality reduction methods were evaluated, but overall, the convolutional neural network performed the best generalization and scored the highest in both classification tests with 92-98% accuracy.[57)]

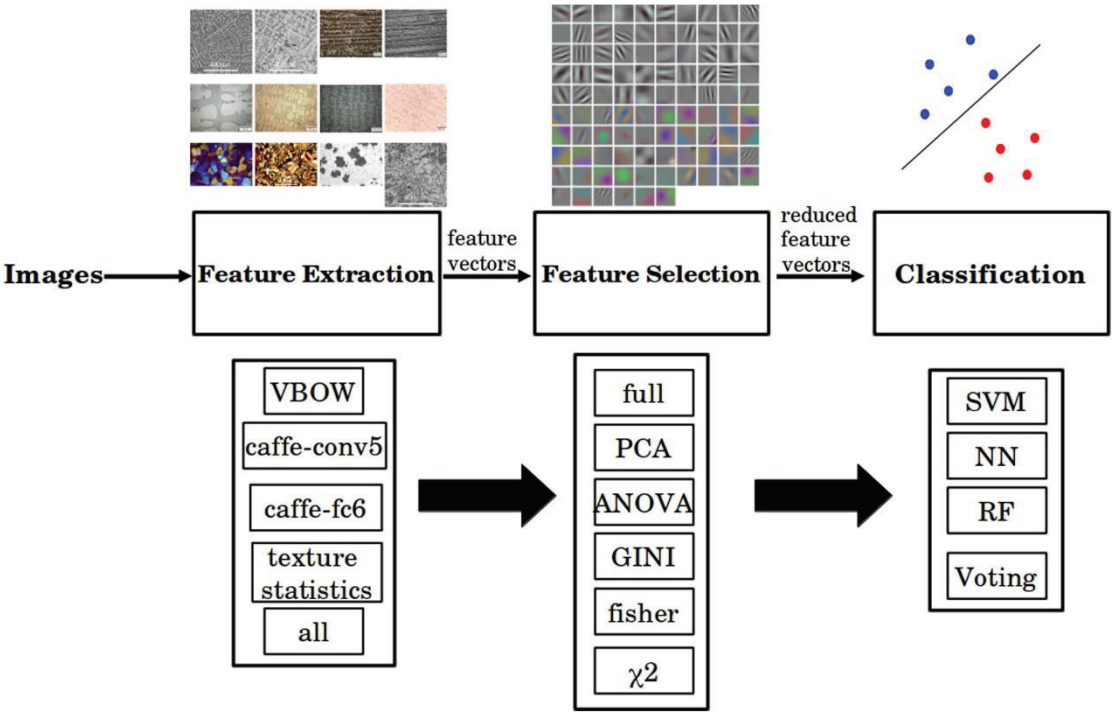


Fig. 1.11 Overview of approach used in classification of micrograph data. The approach summarized here shows 140 different combinations of feature extraction, feature selection and classification methods completed. The same approach presented here was completed first for Task 1 (Data Set 1), then for Task 2 (Data Set 2).[57)]

### 1.3.2 Computer vision and CNN

A number of techniques are used in computer vision (CV) to produce feature vectors, which are numerical representations of visual images. The majority of these techniques are designed for certain purposes like face recognition, object recognition, and texture analysis, etc.[58-69)] There are, however, just two fundamental CV strategies used throughout the application sector. Convolutional neural network (CNN)-based and feature-based representations. An image representation—basically a statistical representation of the visual features of an image—is created using the feature-based approach. The original image is given a filter,[54, 70-73)] which is applied and activated when a feature[64)] (usually an edge, corner, or speckle) is encountered. The image representation is made up of a collection of feature descriptors, [74, 75)] each of which is

digitally encoded with a descriptor.[60, 64] The activation of filters is another visual feature used by CNNs. The major difference between CNNs and feature-based picture representations is that whereas CNN filters are taught during CNN training and optimization, feature-based techniques use filters selected by human experts. Furthermore, in a typical CNN task, the activation of the filter is not abstracted into the image representation. As a feature map of the image, it is utilized directly instead.[76] As a result, with the release of the AlexNet CNN in 2012, CNNs have performed better than feature-based techniques (often those used by human experts[77]) among almost all CV tasks.[78]

The basic goal of computer vision is to represent the visual content of an image in digital form, and there are many ways to do this with CNNs. Among them, CNN layers and super columnar pixels are two methods that are particularly suitable for microstructure images. Convolutional neural networks take an image or image-like data as input, apply various signal processing operations to encode it as a vector, and use artificial neural networks or other ML methods to draw conclusions about the visual content of the image. The first part of the CNN pipeline, encoding images into feature vectors, is called the feature learning phase, while the second part is the classification phase that drawing conclusions. In the feature learning phase, the CNN raster filter patch set is moved pixel by pixel and the activation values of the filters are recorded, as shown in Fig. 1.12. This operation starts with the image, generating the first convolutional layer, and proceeds in subsequent layers generating the second to *n*th convolutional layers. After several convolutions, the activation is modified (usually by a modified linear unit ReLU, where the filter converts negative values to zero). Pooling (or down sampling) merges several pixels of one layer into one pixel of the next layer and performs another series of convolutions. After several iterations of convolution and pooling, the final layer, the complete combined layer, is expanded and written as a vector to form the representation used for decision making in the classification stage.[76, 79] It is worth noting that the convolution process produces CNN features that are translation invariant, but not rotation or scale invariant. This means that a feature may

require multiple representations, for example, to capture different geometric orientations in the microstructure.

Designing and training CNNs requires deep expertise and large datasets (often millions of images), which is not realistic for most microstructure datasets. However, CNNs optimized and trained on a large number of natural images have been successfully used for other types of images containing microstructures. The transferability of this result may be due to the fact that images of very different things share common visual features, such as edges, spots, and visual textures. Thus, pre-trained CNNs, such as the VGG16 network[76] trained on the ImageNet dataset, can be used to represent microstructures by transfer learning. However, since assigning microstructure images to ImageNet categories such as broccoli, barrels, and haggis does not make sense to material scientists, the network is usually truncated before the classification stage. Instead, the CNN layer itself was used as the image representation for the ML task. Typically, dimensionality reduction coding, such as principal component analysis (PCA) or vector of local aggregation descriptors (VLAD), is used. It reduces the length of the feature vector used for efficient computation.[70]

Which layer of the CNN representation is the best choice for the feature vector depends on the characteristics of the micrograph.[80] The deep layer captures features at large length scales because the pooling operation produces deep pixels that represent a large area of the original image. In contrast, shallow filter activations represent the local environment. Thus, visually simple micrographs, such as the equiaxed polycrystal, can be more fully represented in the shallow layers, while complex microstructures, such as the carbide structure, can be more fully represented in the deep layers and more fully capture the multiscale structure. However, there is currently no mechanism to determine the best layer to represent a particular type of microstructure a priori. Instead, decisions are made through iterative experiments.[70, 80]

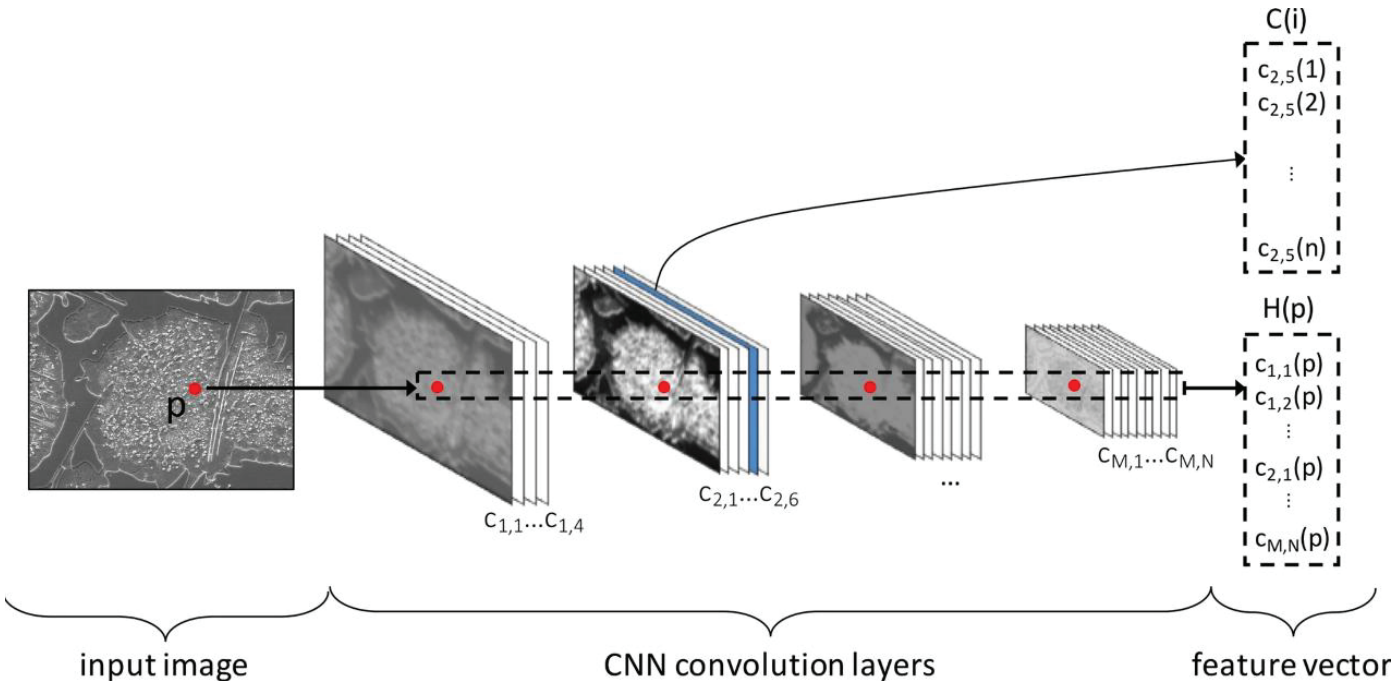


Fig. 1.12 The feature learning stage of a CNN. The input image *i* (left) is processed through layers $c_{1,1}$ through $c_{M,N}$. Pooling decreases image resolution between groups (or blocks) of layers. A feature vector for the image as a whole, C(*i*), may be constructed by flattening any of the layers (here, the $c_{2,5}$ convolution layer shown in blue). Alternatively, a feature vector for each pixel p may be assembled from filter activations in all the layers, giving the hypercolumn pixel vector, H(p).[81)]

To obtain a more complete representation of the image, one may wish to combine information from all convolutional layers. This is the basis for the pixel feature vector at the top of the column[58)], as shown in Fig. 1.12. Holm *et al.*[81)] start with a pre-trained CNN image and its convolutional layers, for each pixel selected in the original image, a super column is constructed by stacking the activations of the convolutional layers at the true spatial location of the pixel. The result is an image representation in which each super column stores information about the feature members of the pixel on multiple length scales. Using a per-pixel super column to represent an image consumes a large amount of memory, so a sparse subset of pixels is usually chosen. Sub-column features are mainly used for image segmentation tasks. Finally, note that CNNs can work in reverse (i.e., using inverse convolution) and generate images from the feature vector. This is the basis for variable autoencoders (VAE)[82)] and generative adversarial networks (GAN). These methods can be used to generate realistic synthetic images[83, 84)] and to improve image resolution[85)], among other applications.[86, 87)]

## 1.4 Objectives of this study

The microstructure of metallic materials significantly affects their properties. Therefore, one of the most critical parts in the characterization of metallic materials is the investigation of microstructure. Traditionally, the classification of microstructure is mostly accomplished manually by human specialists, which introduces subjectivity-related uncertainties. Various intelligent image analysis techniques have developed in recent years with the advancement of computer technology, offering new thoughts to microstructure evaluation. As a result, there have been many attempts at the classification and characterization of the microstructures by using machine learning techniques and related technology, for the purpose of improving the accuracy and efficiency of microstructure analysis compared to the traditional methods.

Numerous outstanding accomplishments have been made in the study of recognizing and classifying the microstructure of the steel. However, there hasn't been much study done on aluminum alloy, a structural material that is as important as steel. The morphology and distribution of second-phase particles play an important role in the mechanical properties of casting Al alloys. In this study, we attempted to classify the microstructures of Al-Si casting alloys at different casting conditions and aging at different times by using machine learning techniques. Besides, quantitatively analyzed the morphology and distribution of second-phase particles in the matrix with our originally developed methods.

In this study, we attempted to classify the microstructures of Al-Si casting alloys at different casting conditions and different time of aging by using machine learning techniques. Besides, quantitatively analyzed the morphology and distribution of second-phase particles in the matrix with our originally developed methods. This work hopes to help improve the accuracy and efficiency of microstructural analysis for quality control and for the design of new aluminum alloys with desirable properties.

## 1.5 Outline of this thesis

In Chapter 1, background information about the Al-Si casting alloy was presented, including the effect of cooling rate, modification treatment, and aging treatment on the microstructures of this alloy and possible mechanisms. In addition, some examples of machine learning and neural network applications in the field of materials science and related research results were listed.

In Chapter 2, the originally developed quantitative analysis method for the spatial distribution of second-phase particles used in this study was described in detail, as well as the specific process of machine learning and the calculation of classification rates. The classification of the microstructures of Al-Si casting alloys at different stages of T6 heat treatment using the above methods was also included.

The classification of the microstructures of Al-Si alloys casting at different cooling rates was accomplished by machine learning techniques, the results and discussions were shown in Chapter 3. The classification rate and its change with the number of images in training data were measured, and a suitable number of images for training was found.

In Chapter 4, the Al-Si casting alloys were modified by Sr, and the microstructural classification of unmodified and Sr modified samples was completed by machine learning techniques. The distribution and morphology of eutectic Si-phase differences before and after modification were quantitatively analyzed using our originally developed methods. The classification results, the effect of Sr additive on the distribution and size of eutectic-Si particles, and the correlations between mechanical properties and microstructural features were discussed.

The results and discussions from the above-mentioned investigation are summarized in Chapter 5.

## Reference


1) G. Cole and A. Sherman, *Materials characterization*, 1995, **35**, 3-9.

2) W. Miller, L. Zhuang, J. Bottema, A. J. Wittebrood, P. De Smet, A. Haszler and A. Vieregge, *Materials Science and Engineering: A*, 2000, **280**, 37-49.

3) J. Benedyk, in *Materials, design and manufacturing for lightweight vehicles*, Elsevier, 2010, pp. 79-113.

4) D. Carle and G. Blount, *Materials & design*, 1999, **20**, 267-272.

5) M. Tisza and I. Czinege, *International Journal of Lightweight Materials and Manufacture*, 2018, **1**, 229-238.

6) T. Dursun and C. Soutis, *Materials & Design (1980-2015)*, 2014, **56**, 862-871.

7) L. Wang, M. Makhlouf and D. Apelian, *International Materials Reviews*, 1995, **40**, 221-238.

8) A. Heinz, A. Haszler, C. Keidel, S. Moldenhauer, R. Benedictus and W. Miller, *Materials Science and Engineering: A*, 2000, **280**, 102-107.

9) R. Rana, R. Purohit and S. Das, *International Journal of Scientific and research publications*, 2012, **2**, 1-7.

10) V. Kumar, H. Mehdi and A. Kumar, *International Research Journal of Engineering and Technology*, 2015, **2**, 1326-1330.

11) R. K. Verma, L. Agrawal and D. Awana, *International journal on emerging technologies*, 2013, **4**, 149-159.

12) B. Mathai, C. Mathew, K. Pratheesh and C. K. Varghese, *International Journal of Engineering Trends and Technology (IJETT)*, 2015, **29**, 299-303.

13) M. Zamani, Jönköping University, School of Engineering, 2017.

14) L. Agrawal, R. Yadav and A. Sexena, *International Journal on Emerging Technologies*, 2012, **3**, 137-140.

15) R. Rana and R. Purohit, *International Journal of Scientific Engineering and Research*, 2012, **3**, 1-5.

16) Y. M. Abdulsahib, *Al-Qadisiya J Eng Sci*, 2014, **7**, 366-381.

17) G. Adeyemi, B. S. Oluwadare and K. O. Olanipekun, *International Journal of Engineering Science Invention*, 2013, **2**, 1-13.

18) N. Nafsin and H. Rashed, *International Journal of Engineering and Advanced Technology (IJEAT)*, 2013, **2**, 533-536.

19) Y. H. Cho, Y.-R. Im, S.-W. Kwon and H. C. Lee, in *Materials Science Forum*, Trans Tech Publications Ltd., Zurich-Uetikon, Switzerland, 2003, pp. 339-344.

20) M. Zamani, S. Seifeddine and A. E. Jarfors, *Materials & design*, 2015, **86**, 361-370.

21) S. Kumar, N. H. Babu, G. M. Scamans, D. G. Eskin and Z. Fan, *International journal of materials research*, 2012, **103**, 1228-1234.

22) K. Tang, Q. Du and Y. Li, *Calphad*, 2018, **63**, 164-184.

23) G. Nguyen, S. Dlugolinsky, M. Bobák, V. Tran, Á. López García, I. Heredia, P. Malík and L. Hluchý, *Artificial Intelligence Review*, 2019, **52**, 77-124.

24) L. Zhou, S. Pan, J. Wang and A. V. Vasilakos, *Neurocomputing*, 2017, **237**, 350-361.

25) A. K. Jain, R. P. W. Duin and J. Mao, *IEEE Transactions on pattern analysis and machine intelligence*, 2000, **22**, 4-37.

26) F. E. Bock, R. C. Aydin, C. J. Cyron, N. Huber, S. R. Kalidindi and B. Klusemann, *Frontiers in Materials*, 2019, **6**.

27) J. Wei, X. Chu, X. Y. Sun, K. Xu, H. X. Deng, J. Chen, Z. Wei and M. Lei, *InfoMat*, 2019, **1**, 338-358.

28) C. Gao, X. Min, M. Fang, T. Tao, X. Zheng, Y. Liu, X. Wu and Z. Huang, *Advanced Functional Materials*, 2022, **32**, 2108044.

29) J. Huang, J. Liew, A. Ademiloye and K. M. Liew, *Archives of Computational Methods in Engineering*, 2021, **28**, 3399-3413.

30) J. Cai, X. Chu, K. Xu, H. Li and J. Wei, *Nanoscale Advances*, 2020, **2**, 3115-3130.

31) Y. Juan, Y. Dai, Y. Yang and J. Zhang, *Journal of Materials Science & Technology*, 2021, **79**, 178-190.

32) A. Agrawal and A. Choudhary, *Mrs Communications*, 2019, **9**, 779-792.

33) G. R. Schleder, A. C. Padilha, C. M. Acosta, M. Costa and A. Fazzio, *Journal of Physics: Materials*, 2019, **2**, 032001.

34) T. Mueller, A. G. Kusne and R. Ramprasad, *Reviews in computational chemistry*, 2016, **29**, 186-273.

35) L. Heusler and W. Schneider, *Journal of Light Metals*, 2002, **2**, 17-26.

36) F. Stadler, H. Antrekowitsch, W. Fragner, H. Kaufmann, E. Pinatel and P. J. Uggowitzer, *Materials Science and Engineering: A*, 2013, **560**, 481-491.

37) F. Stadler, H. Antrekowitsch, W. Fragner, H. Kaufmann and P. J. Uggowitzer, in *Materials Science Forum*, Trans Tech Publ, 2011, pp. 274-277.

38) J. Olofsson, I. L. Svensson, P. Lava and D. Debruyne, *Materials & Design (1980-2015)*, 2014, **56**, 755-762.

39) F. Stadler, H. Antrekowitsch, W. Fragner, H. Kaufmann and P. J. Uggowitzer, *International Journal of Cast Metals Research*, 2012, **25**, 215-224.

40) Z. Liu, Q. Xu and B. Liu, *International Journal of Cast Metals Research*, 2007, **20**, 109-112.

41) R. Elliott, *Eutectic solidification processing: crystalline and glassy alloys*, Elsevier, 2013.

42) H. Fredriksson and U. Akerlind, *Solidification and crystallization processing in metals and alloys*, John Wiley & Sons, 2012.

43) M. Shamsuzzoha and F. R. Juretzko, *Aluminium Alloys for Transportation, Aerospace, and Other Applications*, 2007, 153.

44) M. Makhlouf and H. Guthy, *Journal of light metals*, 2001, **1**, 199-218.

45) J. Barrirero, M. Engstler, N. Ghafoor, N. de Jonge, M. Odén and F. Mücklich, *Journal of alloys and compounds*, 2014, **611**, 410-421.

46) M. Djurdjevic, H. Jiang and J. Sokolowski, *Materials characterization*, 2001, **46**, 31-38.

47) D. Hamilton and R. Seidensticker, *Journal of Applied Physics*, 1960, **31**, 1165-1168.

48) D. A. Porter and K. E. Easterling, *Phase transformations in metals and alloys (revised reprint)*, CRC press, 2009.

49) B. M. Thall and B. Chalmers, *Journal of the Institute of Metals*, 1950, **77**, 79-&.

50) M. Shamsuzzoha and L. Hogan, *Philosophical Magazine A*, 1986, **54**, 459-477.

51) S.-Z. Lu and A. Hellawell, *Metallurgical transactions A*, 1987, **18**, 1721-1733.

52) A. Velichko, 2008.

53) R. J. Roiger, *Data mining: a tutorial-based primer*, Chapman and Hall/CRC, 2017.

54) B. L. DeCost and E. A. Holm, *Computational materials science*, 2015, **110**, 126-133.

55) X. Liu, University of Birmingham, 2014.

56) J. Gola, D. Britz, T. Staudt, M. Winter, A. S. Schneider, M. Ludovici and F. Mücklich, *Computational Materials Science*, 2018, **148**, 324-335.

57) A. Chowdhury, E. Kautz, B. Yener and D. Lewis, *Computational Materials Science*, 2016, **123**, 176-187.

58) A. Bansal, X. Chen, B. Russell, A. Gupta and D. Ramanan, *arXiv preprint arXiv:1702.06506*, 2017.

59) M. Comer, C. A. Bouman, M. De Graef and J. P. Simmons, *Jom*, 2011, **63**, 55.

60) N. Dalal and B. Triggs, in *2005 IEEE computer society conference on computer vision and pattern recognition (CVPR'05)*, Ieee, 2005, pp. 886-893.

61) P. F. Felzenszwalb, R. B. Girshick, D. McAllester and D. Ramanan, *IEEE transactions on pattern analysis and machine intelligence*, 2010, **32**, 1627-1645.

62) R. Girdhar, D. Ramanan, A. Gupta, J. Sivic and B. Russell, in *Proceedings of the IEEE conference on computer vision and pattern recognition*, 2017, pp. 971-980.

63) Y.-G. Jiang, J. Yang, C.-W. Ngo and A. G. Hauptmann, *IEEE Transactions on Multimedia*, 2009, **12**, 42-53.

64) D. G. Lowe, in *Proceedings of the seventh IEEE international conference on*

*computer vision*, Ieee, 1999, pp. 1150-1157.

65) T.-Y. Lin, A. RoyChowdhury and S. Maji, in *Proceedings of the IEEE international conference on computer vision*, 2015, pp. 1449-1457.

66) D. G. Lowe, *International journal of computer vision*, 2004, **60**, 91-110.

67) A. Oliva and A. Torralba, *Trends in cognitive sciences*, 2007, **11**, 520-527.

68) H. Peng, F. Long and C. Ding, *IEEE Transactions on pattern analysis and machine intelligence*, 2005, **27**, 1226-1238.

69) P. Quelhas, F. Monay, J.-M. Odobez, D. Gatica-Perez and T. Tuytelaars, *IEEE transactions on pattern analysis and machine intelligence*, 2007, **29**, 1575-1589.

70) B. L. DeCost, T. Francis and E. A. Holm, *Acta Materialia*, 2017, **133**, 30-40.

71) B. L. DeCost and E. A. Holm, *Computational Materials Science*, 2017, **126**, 438-445.

72) B. L. DeCost, H. Jain, A. D. Rollett and E. A. Holm, *Jom*, 2017, **69**, 456-465.

73) J. Li and N. M. Allinson, *Neurocomputing*, 2008, **71**, 1771-1787.

74) J. Sivic and A. Zisserman, in *Computer Vision, IEEE International Conference on*, IEEE Computer Society, 2003, pp. 1470-1470.

75) T. S. Guzella and W. M. Caminhas, *Expert Systems with Applications*, 2009, **36**, 10206-10222.

76) K. Simonyan and A. Zisserman, *arXiv preprint arXiv:1409.1556*, 2014.

77) A. Jalalian, S. B. Mashohor, H. R. Mahmud, M. I. B. Saripan, A. R. B. Ramli and B. Karasfi, *Clinical imaging*, 2013, **37**, 420-426.

78) I. Goodfellow, Y. Bengio and A. Courville, *Deep learning*, MIT press, 2016.

79) Y. Guo, Y. Liu, A. Oerlemans, S. Lao, S. Wu and M. S. Lew, *Neurocomputing*, 2016, **187**, 27-48.

80) J. Ling, M. Hutchinson, E. Antono, B. DeCost, E. A. Holm and B. Meredig, *Materials Discovery*, 2017, **10**, 19-28.

81) E. A. Holm, R. Cohn, N. Gao, A. R. Kitahara, T. P. Matson, B. Lei and S. R. Yarasi, *Metallurgical and Materials Transactions A*, 2020, **51**, 5985-5999.

82) D. P. Kingma and M. Welling, *arXiv preprint arXiv:1312.6114*, 2013.

83) S. Chun, S. Roy, Y. T. Nguyen, J. B. Choi, H. Udaykumar and S. S. Baek, *Scientific reports*, 2020, **10**, 1-15.

84) A. Gayon-Lombardo, L. Mosser, N. P. Brandon and S. J. Cooper, *npj Computational Materials*, 2020, **6**, 1-11.

85) H. Chen, X. He, Q. Teng, R. E. Sheriff, J. Feng and S. Xiong, *Physical Review E*, 2020, **101**, 023305.

86) J. C. Van Gemert, C. J. Veenman, A. W. Smeulders and J.-M. Geusebroek, *IEEE transactions on pattern analysis and machine intelligence*, 2009, **32**, 1271-1283.

87) J. Zhang, M. Marszałek, S. Lazebnik and C. Schmid, *International journal of computer vision*, 2007, **73**, 213-238.

# *Chapter 2*

# Microstructural Classification of Al-Si Casting Alloy after Aging with Machine Learning Techniques

## 2.1 Introduction

In machine learning, the high-dimensional feature vector is used to extract quantitative visual information. This information may include a classification (such as classification of ferritic, austenitic, and martensitic, etc.), association with a metadata value (such as yield strength), measurement (such as grain size), presence of a specific feature (such as surface defect), or any other value that may be present in the feature vector. There are essential roles for both supervised and unsupervised machine learning (ML) techniques. Supervised ML techniques are taught using known right answers, or "ground truth," whereas unsupervised ML techniques uncover patterns without knowing a "ground truth."

The selection of supervised machine learning technique relies on the application and is made from a broad range of approaches. For visual image feature vector data, supervised ML systems often utilized include support vector machines (SVM)[1, 2], random forest (RF) classifiers[3], and deep learning techniques such artificial neural networks (ANNs)[4-6].

SVMs work by figuring out which set of hyperplanes best divides feature vectors into groups based on the kind or class of the underlying ground truth. Additional vectors may be categorized and associated with the appropriate group after the separation planes are established. Flexibility, generality, and performance are benefits of SVM. However, whether the high-dimensional data structure is amenable to planar separation determines whether an SVM model will be successful.

To determine the class of an image, RF classifiers first build a number of decision trees; choices made inside each tree are dependent on the values of feature vector components. The trees each provide a forecast, and the classification is determined by majority rules. The feature vector components that make up the trees and their decision values are tuned during the training phase of an RF classifier to provide the best agreement with the known ground truth. The trees may be used to categorize new vectors once they have been tuned. Interpretability is a benefit of RFs since the justification for a choice

can be readily validated[7]. However, RFs are not always simple to apply to intricate picture representations.

ANNs use a neural network's hidden layers to analyze the feature vector and provide a prediction about the picture[8]. The ANN's connection and structure may take on a variety of shapes, and its architectural design is chosen to enhance performance, often by trial and error. The weights of the connections between neurons in the input, hidden, and output layers are tuned throughout the learning process to provide the best match with the recognized ground truth. The weights must be chosen before the ANN can predict previously unknown vectors. As a class, ANNs scale to accommodate both massive volumes of data and data with very high dimensions. However, since they are black box models, it might be difficult to understand how decisions are made.

Without the use of human involvement or ground truth data, unsupervised machine learning algorithms identify correlations between visual representations by creating clusters of similar images. One unsupervised clustering technique is k-means[9]. The k-means algorithm divides a collection of N-dimensional feature vectors into a user-specified number of N-dimensional clusters that minimizes a cost function that is a measure of "cluster quality," such as cluster compactness. k-means employs a variety of computing techniques to identify effective solutions since finding a globally optimum clustering is an NP-Hard problem, which demands exponential computing time. This has the effect that, for a given collection of vectors, the output of k-means may differ depending on the computing settings. K-means clustering has the benefit of identifying a collection of cluster centroids, allowing for the direct association of extra vectors with clusters. As a result, it may serve as a foundation for categorization. As a complete N-dimensional representation, one drawback is that it could be difficult to visualize the findings in 2D or 3D.

To find clusters based on picture similarity, there are many techniques available for visualizing high-dimensional image representations in two or three dimensions. In the examples that follow, we employ t-distributed stochastic neighbor embedding (t-SNE)[10,

[11], which heavily favors grouping similar images but fails to recognize relationships between dissimilar images. t-SNE weights image similarity on a nonlinear scale that rapidly diminishes as image similarity decreases. Low-dimensional clusters may frequently be found and seen with t-SNE, which is a benefit. Because t-SNE is built via pairwise comparisons of feature vectors, it has the drawback that it cannot be used for classification because new data cannot be added to an t-SNE map without completely recalculating it.

The kind of input data and the intended result will choose the ML modality and model to use. Frequently, different strategies are tried and their effectiveness as well as other benefits and drawbacks are assessed. Since the best-in-class solutions are always changing, it is advantageous to include a domain specialist in ML algorithms in this process.

Supervised learning was used in this research. The main goal of supervised learning is a method for creating and learning models from pre-labeled training data in order to predict and classify unknown data. "Classification" is positioned as a subfield of supervised learning, the purpose of which is to predict the category labels of new data based on previous learning. In this study, the classification of aging treatments was performed with the samples labeled "Casting", "Solution treatment", "Aging time 10 mins", "Aging time 1 hour", "Aging time 2 hours" and "Aging time 6 hours". We used copper molds with variable temperatures for the casting of Al-Si alloys and obtained samples with three different cooling rates, which were identified by sample labels according to the cooling rate. For the modified treatment, two categories labeled "no modified treatment" and "with modified treatment" were covered, as well as three categories labeled "no Sr addition", "0.01 *wt%* Sr content" and "0.02 *wt%* Sr content".

## 2.2 Machine Learning Processes

Tens to hundreds of microstructure photographs are randomly taken on the sample cross-section using an optical microscope, and after image processing, the feature values associated with them are extracted from the processed microstructure photographs, and then machine learning techniques are applied to identify and classify the microstructure of samples with different time aging treatments and different casting conditions. As shown in Fig. 2.1, the actual learning process of supervised learning is divided into a "learning phase" and an "evaluation phase". In the learning phase, the pre-labeled images are binarized and features are extracted from the binarized images. The binarization process is described in detail in Section 2.2.1. A discriminator is then created based on the various extracted features. The discriminators created in this study use the following two algorithms, Support Vector Machine (SVM) and Random Forest (RF). Both algorithms are explained in detail in Section 2.2.3. Next, the image to be recognized (test image) is similarly binarized and features are extracted. The features used in this study are LN2D, IMFP, area fraction, number density, diameter, long edge, narrow edge, aspect ratio, and roundness. This will be explained in detail in section 2.2.2. These features extracted from the test images are compared with the data from the created discriminator to determine which label they belong to.

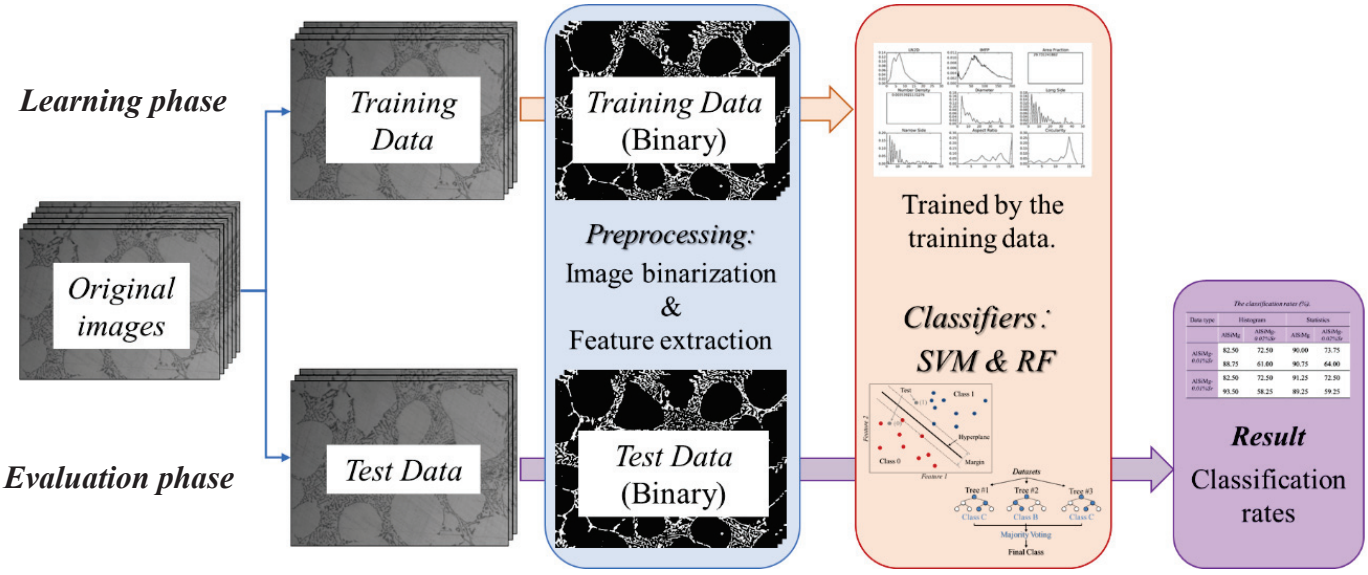


Fig. 2.1 Flow chart of machine learning process.

### 2.2.1 The process of binarization

Binarization is an image processing process that converts the target image into black and white. This process increases the processing speed of machine learning and extracting features from the input image becomes easier. The process of binarization is shown in Fig. 2.2. First, the brightness value of the original image is adjusted to clarify the shadows of the image, and the image is blurred with a bilateral filter, which is used because it preserves the sharp edges of the second phase compared to the Gaussian filter. After that, it is converted to a binary image using adaptive thresholding as shown in Equation (2.1). Here $\theta$ denotes the threshold value (range of possible density values: 0-255), and the density value $f$ (x, y) in a certain coordinate system and the converted density value $f'$ (x, y) are used. In most thresholding methods, the same threshold is applied to all pixels of the image. However, in some cases, it may be useful to apply different thresholds to different parts of the image depending on the local brightness of the pixel. This method is called adaptive thresholding. This method is particularly useful in cases where the image has an uneven brightness. Finally, binarization is performed by noise reduction through an opening procedure. The opening procedure is a basic method of morphological noise reduction that combines the erosion operation and the expansion operation of image processing. A specified amount of reduction is followed by a similar amount of expansion. Dilation is a method that replaces the white pixels of interest with white pixels if there are white pixels in the vicinity of the pixels of interest. Conversely, if there is even one black pixel in the surrounding area, the shrinkage process replaces the focal pixel with a black one.

$$f'(x,y) = \begin{cases} 255 & when\ f(x,y) \geq \theta \\ 0 & when\ f(x,y) < \theta \end{cases} \tag{2.1}$$

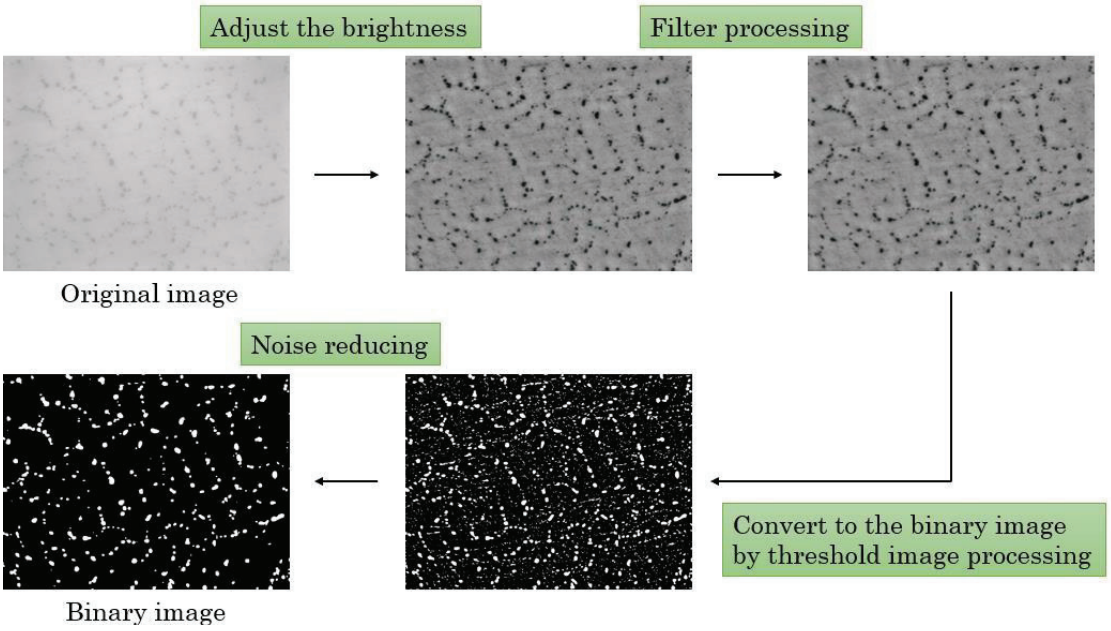


Fig. 2.2 Procedure of the binarization process.

### 2.2.2 Feature extraction

After binarization, every particle in the metal matrix could be located, and the gravity center, area, perimeter, circumscribed rectangle, etc., of the particles will be marked automatically, as shown in Fig. 2.3. Feature extraction is performed and the parameters of the second phase particles, such as the area fraction and number density of the second phase particles, as well as the equivalent circle diameter, long and short side lengths, aspect ratio, and circularity, are measured. The features extracted from the binary images including LN2D, IMFP, Area fraction, Number density, Diameter, Long and Narrow side, Aspect ratio, and Circularity, the descriptions of which are shown in Table 2.1. The mean and standard deviation of the features are used for machine learning features. The LN2D and IMFP are our originally developed methods to quantitatively describe the distribution of second phase particles in the matrix. The details of these two methods will be elaborated at next section.

Table 2.1 Descriptions of the features

| Name | Description |
|---|---|
| LN2D | 2-dimentional local number, quantitative analysis of the distribution of second phase particles. |
| IMFP | Image mean free path, quantitative analysis of mean free path of dislocation motion. |
| Area Fraction | Area fraction of second phase particles in matrix. |
| Number Density | Number of particles per unit volume. |
| Diameter | Equivalent circle diameter. |
| Long side | Long side of second phase particles. |
| Narrow side | Narrow side of second phase particles. |
| Circularity | $C = 4\pi A/L^2$ (A: area size, L: perimeter), The closer the value is to 1, the closer the area is to circle. |
| Aspect ratio | |

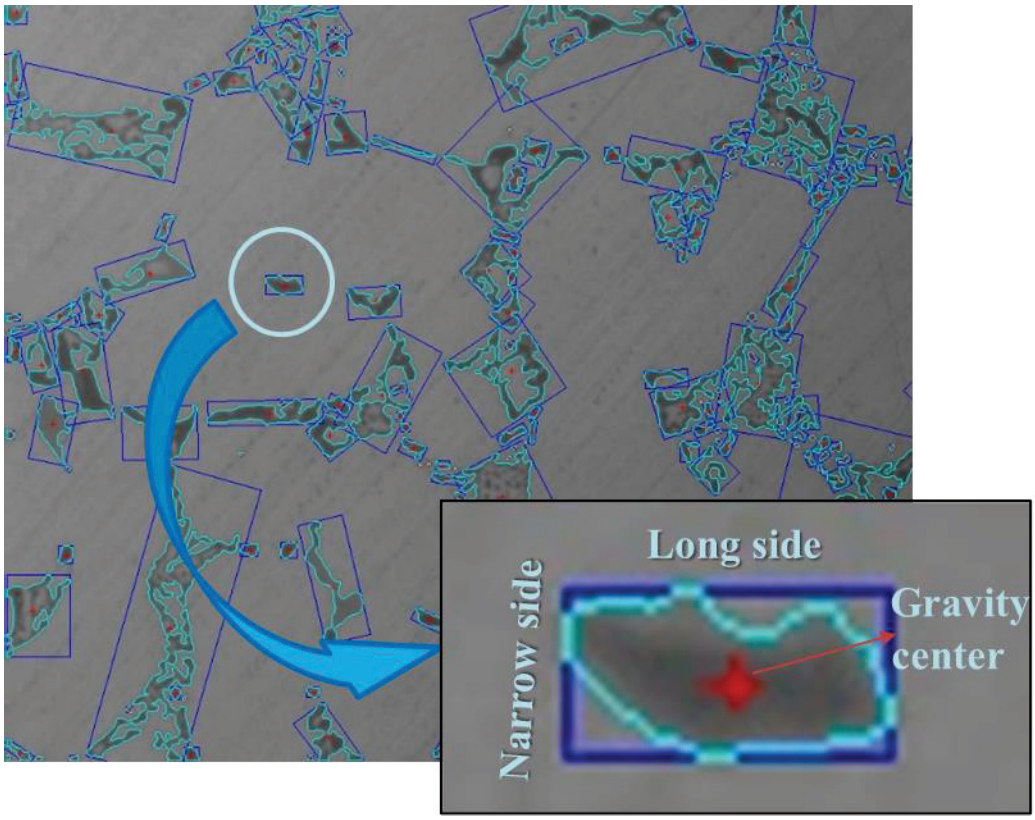


Fig. 2.3 The gravity center, area, perimeter, circumscribed rectangle, etc., of the particles.

#### 2.2.2.1 Definition of LN2D

Two-dimensional local number (LN2D)[12] is a quantitatively evaluating method of the spatial distribution of second phase, Fig. 2.4 shows an overview of the LN2D measurement method. The number of gravity centers (GC) of second phase in the measuring circle is defined as LN2D. Since the center of the measuring circle is located on GC, the number of LN2D samples is equal to the total number of GCs measured in LN2D. The radius of the measuring circle is determined so that the number density of the circle including 7 GCs corresponds to the whole number density in 2-dimension, where 7 means the number of a noticed GC and nearest neighbor GCs in the measuring circle when assuming the closest hexagonal structure, as shown in Fig. 2.4 (a). The measuring radius, $R_{2D}$, is represented by

$$\frac{7}{\pi {R_{2D}}^2} = \lambda_A \implies R_{2D} = \left(\frac{7}{\pi\lambda_A}\right)^{1/2} = \frac{1.493}{{\lambda_A}^{1/2}} \tag{2.2}$$

where $\lambda_A$ is the whole number density of second phase.

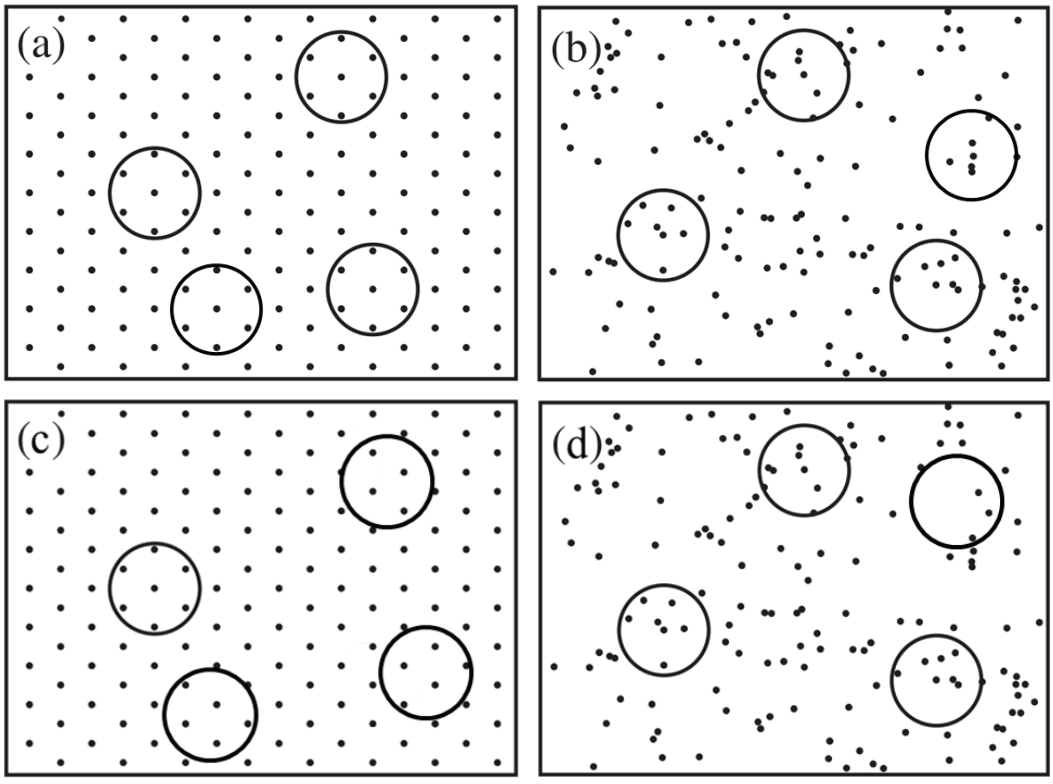

Fig. 2.4 Measuring circles at the closet hexagonal ordered and random arrangements of gravity center (GC) of particles.

If the model shown in Fig. 2.4 is assumed and the measurement circle obtained from equation (2.2) is placed at an arbitrary position (Fig. 2.4 (c) and (d)), the number of particles in the measurement circle will be more in the dense region and less in the sparse region. In this case, two-dimensional local number in random circle (LN2DR) is a measurement method in which the measurement circles are placed randomly. The same measurement circles are used in LN2DR. In this study, the spatial distribution is evaluated by the frequency distribution of the LN2DR. When the distribution is uniformly random in both dimensions, according to the Poisson distribution, the number $k$ of points presents in the measurement circle when a window of area A (hereafter $W_A$) is placed anywhere in the plane is represented by

$$P(k) = \frac{(\lambda_A W_A)^k}{k!} exp(-\lambda_A W_A) \quad k = 0, 1, 2 \cdots \tag{2.3}$$

where $P(k)$ is the probability when the number of points in the measurement sphere is $k$, and $\lambda_A$ is the number of points per unit area (number density). According to the definition of the two-dimensional measurement circle, $\lambda_A W_A = 7$. Therefore, the LN2DR follows the Poisson distribution formula in Equation (2.4). If the measurement circle follows this distribution, then the particle's center-of-mass points are randomly distributed.

$$P(LN2D = k) = \frac{7^k}{k!} exp(-7) \quad k = 0, 1, 2 \cdots \tag{2.4}$$

As mentioned previously in this section, the number of LN2D samples is limited, while LN2DR is an evolved version of LN2D, since the center of measuring circle is randomly located in the measuring process of LN2DR, the number of samples can be increased to the order of one million. The average of this distribution is 7, and the dispersion of the second phase particles is more uniform the lower the variance value of LN2DR. The average and the variance of LN2DR were utilized for machine learning features.

#### 2.2.2.2 Definition of IMFP

Image mean free path (IMFP)[13] is the amount related to the mean free path of dislocation motion, Fig. 2.5 shows an overview of the IMFP measurement method. IMFP is the distance that a randomly occurring dislocation in a native crystal can move in a random direction, which is measured by following procedures. (1) A staring point *A* in aluminum matrix and two traveling directions (red and blue arrows) are selected randomly. (2) A free path length, $l_f$, between the starting point in aluminum matrix and encountered silicon eutectic is measured, but measurement starts again from procedure (1) when some edge of image is found (green arrows). Procedure (1) and (2) were repeated at least one million times, and the image mean free path was calculated by averaging *a* (IMFP Single) or $a + b$ (IMFP Double). The average and the standard deviation of the free path length, $l_f$, were utilized for machine learning features. The IMFP indicates that the smaller the IMFP, the shorter the distance that the misalignment can move. Therefore, it can be assumed that the strength tends to increase as the value of IMFP in the image decreases. On the other hand, elongation is considered to have a tendency to decrease with decreasing IMFP values in the image[13].

### 2.2.3 Classifiers of machine learning

#### 2.2.3.1 Support vector machines (SVMs)

Support vector machines (SVMs) are pattern discriminators developed by Vapnik *et al.* Pattern recognition is the classification of an object consisting of several classes into a particular class. SVMs were initially intended to be used with binary (two-class) situations. A proper multi-category method is required when dealing with challenges that span many categories. Multiclass problems are frequently solved using methods like " one against one " and " one against the rest "[1, 14]. SVMs are widely used not only in electrical and electronic information processing, such as character recognition and

fault diagnosis, but also in medicine and chemistry because of their high discriminative power and flexibility of application.

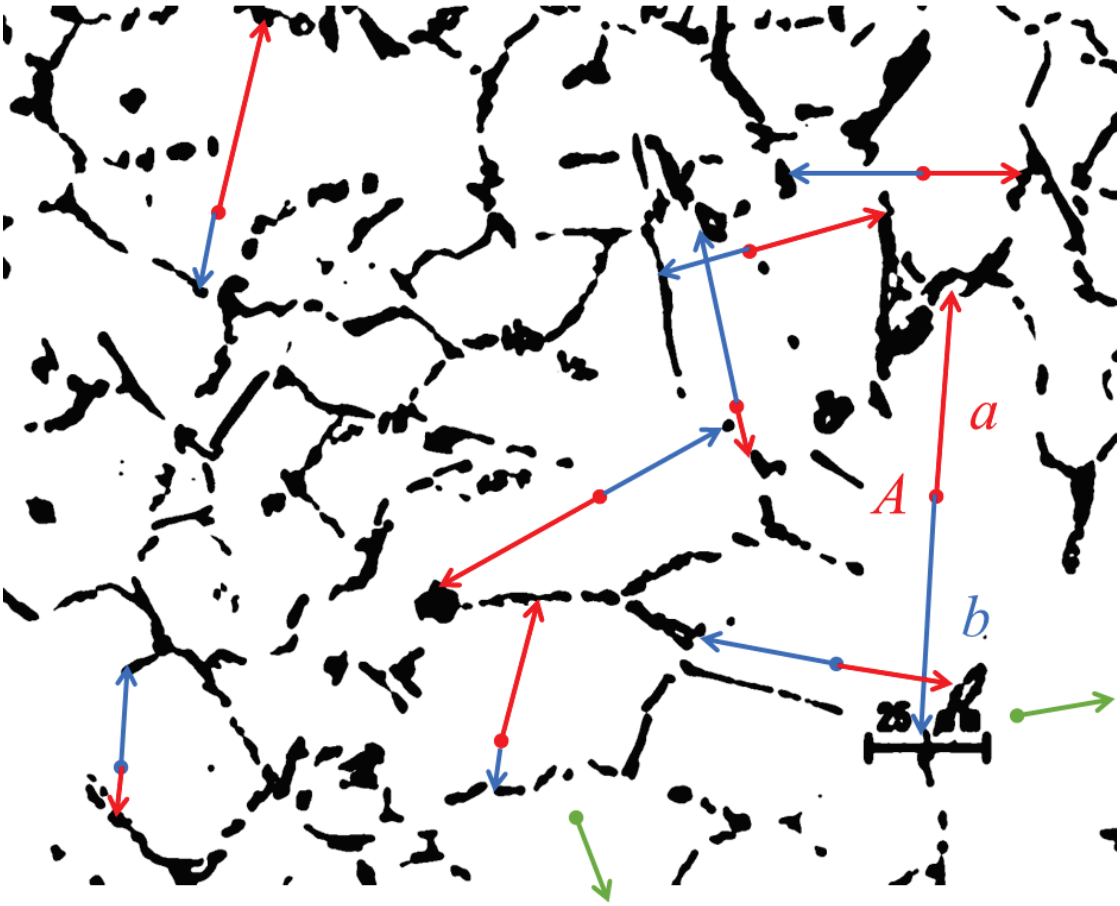


Fig. 2.5 Schematic of the measurement of IMFP.

By utilizing the obtained data for learning, SVMs create patterns. Although SVMs are based on statistical learning theory, their most significant characteristic is their generalization capacity to recognize data that has not been used for training. By learning to identify data that has not been used for training, SVMs may enhance this generalization ability. The goal of SVMs, which are based on statistical learning theory, is to locate the decision boundary that results in the optimal separation class. The SVM chooses a linear decision boundary that leaves the two classes with the greatest possible margin of separation in a two-class pattern recognition task when the classes are linearly separable. The margin is calculated as the sum of the distances between the two classes' closest points and the hyperplane. Quadratic programming (QP) optimization methods

can be used to tackle this margin maximization problem. The margin is calculated using the data points that are closest to the hyperplane. These data points are therefore referred to as "support vectors," and they are always small in number.

SVM can also be applied to nonlinear problems with complex boundaries between two classes. However, instead of dealing with nonlinear problems directly, it maps the space representing the original data to a high-dimensional feature space, trying to find a hyperplane that maximizes the margin while minimizing a quantity proportional to the number of misclassification errors. The tradeoff between margins and misclassification errors is controlled by a user-defined positive parameter C. SVMs can also be extended to handle nonlinear decision surfaces. Boser *et al.*[15] proposed a method that projects the input data into a high-dimensional feature space through some nonlinear mapping and formulates a linear classification problem in that feature space.

Nonlinear classification can also be performed by defining a function (called a kernel) that is appropriate for each specific problem. This is known as a kernel trick, and methods using kernel tricks are collectively referred to as kernel methods. Kernel functions are used to reduce the computational cost of dealing with high-dimensional feature spaces. The following is a description of a support vector machine with a kernel. First, a hyperplane is defined as in Equation (2.5). where $\boldsymbol{w}$ is a weight function, $\boldsymbol{x}$ is data, and $b$ is a constant.

$$\boldsymbol{w} \cdot \boldsymbol{x} - b = 0 \tag{2.5}$$

In equation (2.5), the data closest to the hyperplane is $\boldsymbol{x}^*$, and a good adjustment of the weights and constant multipliers yields equation (2.6).

$$\boldsymbol{w} \cdot \boldsymbol{x}^* - b = 1 \tag{2.6}$$

Then the distance from the hyperplane to the data $\boldsymbol{x}^*$ is $1/|\boldsymbol{w}|$. Now, maximizing the distance from the hyperplane to the data closest to the hyperplane can be replaced by the problem of minimizing $|\boldsymbol{w}|^2$. Since the data closest to the hyperplane has the relationship shown in Equation (2.6), the following conditions hold for the other data.

$$\boldsymbol{w} \cdot \boldsymbol{x} - b \geq 1$$

$$\boldsymbol{w} \cdot \boldsymbol{x} - b \leq -1$$

This, together with the correct classification value $t$ ($t$ = +1 or -1), leads to the condition shown in Equation (2.7).

$$t(\boldsymbol{w}^* \cdot \boldsymbol{x} - b) \geq 1 \tag{2.7}$$

In summary, the problem that SVM must solve is the following optimization problem for $\boldsymbol{w}$ and $b$.

$$\min \quad Q(\boldsymbol{w}, b) = \frac{1}{2}|\boldsymbol{w}|^2$$

$$s.t. \quad t(\boldsymbol{w} \cdot \boldsymbol{x} - b) \geq 1$$

Such an inequality-constrained optimization problem can be solved by the Lagrange undetermined multiplier method as in Equation (2.8).

$$L(\boldsymbol{w}, b, \alpha) = \frac{1}{2}\boldsymbol{w} - \sum \alpha_i (t_i(\boldsymbol{w} \cdot \boldsymbol{x_i} - b) - 1) \tag{2.8}$$

$$\boldsymbol{w} = \textstyle\sum_i \ \alpha_i t_i \boldsymbol{x}_i$$

$$b = \boldsymbol{w} \cdot \boldsymbol{x}^* - 1$$

The hyperplane derived from these equations is as in Equation (2.9).

$$f(x) = \textstyle\sum_i \ \alpha_i t_i \boldsymbol{x}_i \cdot \boldsymbol{x_j} - b \tag{2.9}$$

The optimization problem and the hyperplane equation have an inner product, which is replaced by the kernel function $K$. Equation (2.8) becomes Equation (2.10).

$$\max \quad Q(\alpha) = \sum_i \alpha_i - \frac{1}{2}\sum_{i,j} \alpha_i \alpha_j t_i t_j K(\boldsymbol{x_i}, \boldsymbol{x_j})$$

$$s.t. \quad \sum_i \alpha_i t_i = 0, \ \ \alpha_i \geq 0$$

$$f(x) = \textstyle\sum_i \ \alpha_i t_i K(\boldsymbol{x}_i, \boldsymbol{x}) - b \tag{2.10}$$

Using equation (2.10) to determine a kernel function $K$ that returns some value from the two feature sets, the SVM can solve the optimal problem from there and derive a model that classifies the data into two categories[16].

#### 2.2.3.2 Random Forest (RF)

Random Forest, first proposed by Breiman[17], can be seen as an extension of Bagging integration learning. It is a method of prediction using a large number of randomly generated decision trees, and the most widely used machine learning method today and in many cases does not require parameter tuning or data scaling. Multilevel classification and regression problems can also be easily handled, and many decision trees can be used without causing overtraining. In classification problems, the categories are determined by a majority vote of the categories predicted by each classification tree.

The random forest first uses the bootstrap resampling technique, where n samples (typically 2/3) are repeatedly drawn at random from the original training sample set $T$ in a replayed manner to generate a new set of training samples, and each independently drawn training sample is used to train a tree, and the n decision trees generated based on the self-help sample set form the forest. Each tree has the same distribution and the classification error depends on the classification ability of each tree and the correlation between them. The remaining unextracted data set is called out-of-bag (OOB), and its error is an unbiased estimate that can be used to verify the performance of the model to prevent overfitting.

The generalization error $P^*$ of a random forest is defined as

$$P^* \leq \frac{\rho(1-s^2)}{s^2} \tag{2.11}$$

where $\rho$ is the average value of decision tree correlation, and $s$ is the average strength of the decision tree.

From equation (2.11), it can be seen that to enhance the generalization performance of the random forest, the correlation between each underlying decision tree model needs to be reduced or the strength of the decision tree needs to be enhanced. For this purpose,

random perturbations of feature variables are introduced in the random forest algorithm, i.e., the split nodes involved in each tree may be different. Therefore, the training samples and each node variables are randomly generated in the random forest algorithm. Decision tree algorithms are a large family, and Breiman *etal.*[18] builds random forests based on classification and regression trees. In the process of building each classification and regression tree, the splitting process of each node relies on the calculation of the "purity" of the split sample, and the classification and regression trees use the Gini coefficient to measure this so-called "purity", i.e., the random forest uses the Gini index to The Gini index is used to split the tree to complete the decision. The smaller the Gini coefficient, the higher the purity of the samples and the better the tree partitioning. Assuming that the sample set T contains k categories, the Gini coefficient of the sample set can be expressed as follows

$$gini(T) = 1 - \sum_{i=1}^{k} p_i^2 \tag{2.12}$$

where $p_i$ is the probability of containing class $i$ in $T$. If $T$ is partitioned into two subsets $T_1$ and $T_2$, the Gini coefficient after partitioning can be expressed as

$$gini(T_1, T_2) = \frac{|T_1|}{|T|} gini(T_1) + \frac{|T_2|}{|T|} gini(T_2) \tag{2.13}$$

where |*| represents the number of elements in the current sample set.

The advantages of the random forest classifier including: fewer parameters to be selected and simple implementation; the ability to handle high-dimensional data without feature selection; the ability to internally perform unbiased estimation of generalization error with good generalization capability; and the use of sampling techniques to select samples that can effectively handle class-imbalanced data.

### 2.2.4 Classification

#### 2.2.4.1 Evaluation of classification rate

As shown in Fig. 2.1, the images will be randomly taken out and divided into 2 parts, one part for training, and the other part for test, which means that the images belonging

to training data were only used for machine learning, and the images belonging to test data were only used for classification. After the preprocessing, the data of extracted features will be used to train the model and a classifier will be used for the classification. Two kinds of classifiers, SVM and random forest, were used in this work. Our system is suitable for two-class problems, which is to compare and classify two different structures at one time. Both the training data and the test will contain microstructural images of two different samples (have the same amount), and in the training data, the different images will be marked by label 0 or label 1, depending on whether it belongs to the same sample. After the machine learning process, the test data of mixed images of two samples will be marked label 0 or 1 by the classifier model being trained. If one image marked as label 0 in the result belongs to the same sample as the image with the same label in the training data, it is regarded as a correct recognition, otherwise, it is an error. The classification rate will be the percentage of the total correct recognition number in all images of test data. The classification rate, R, calculated by

$$R = \frac{N_c}{N} \times 100,$$

where $N_c$ is the number of images that classified correctly and $N$ is the total number of images in test sets. Dozens of images for each sample were prepared, and about 50% to 80% images are used for learning phase and about 20% to 50% images were used for evaluation phase.

#### 2.2.4.2 Principal component analysis (PCA)

Principal Component Analysis (PCA)[19] is one of the unsupervised learning. In general, the vector space dealt with in the problem of image recognition is often multidimensional. Therefore, a method that can reduce the dimension while maintaining the maximum amount of information is very useful. PCA is a method of reducing the information contained in p feature values (variables, $x_1, x_2, x_3, \ldots, x_p$) to m synthetic feature values ($m < p$). If a linear subspace that closely approximates the distribution of feature vectors can be constructed, it will be possible to compress the dimensions while preserving the statistical features of the data. Also, by performing

PCA, information such as contribution rate, cumulative contribution rate, and plot diagram of principal components can be obtained. By analyzing these data, it is possible to infer which feature quantity contributes significantly to image classification.

## 2.3 Classification of the aging process samples

### 2.3.1 Experimental material

For comparison before and after aging treatment, an Al-4%Si-0.5Mg alloy was used in the experiments. The specimens were prepared by gravity casting using ingots of pure Al, Al-24.3%Si alloy and Al-10%Mg alloy.

### 2.3.2 Pretreatment steps

Al-4 %Si-0.5 %Mg alloy specimens prepared by gravity casting were polished using #600 sandpaper, #800, #1000, and #2400 in that order, followed by mirror finishing using 3 μm and 1 μm diamond slurries. Thirty images of the microstructure of the mirror-finished surfaces were taken using an optical microscope (OM) at 400x magnification for each of the casting, solution annealing, and aging treatments. Indentations were made using a Vickers hardness tester as landmarks so that similar locations could be photographed for each treatment. The experimental conditions for solution annealing and each aging treatment are shown in Table 2.2. The aging treatments were performed on the same specimens in sequence so that changes in the microstructure of the same component could be observed. The samples were stored in a freezer to prevent spontaneous aging.

Table 2.2 Experimental condition of T6 treatment

| | Holding temperature (K) | Holding time (ks) | Cooling method |
|---|---|---|---|
| Solution treatment | 808 | 21.6 | Water-cooled |
| Aging treatment | 473 | 0.6, 3.6, 7.2, 21.6 | Air-cooled |

### 2.3.3 Analysis methods

There are 2 kinds of data types used in this study, histogram data, which is the relative frequency (R-frequency) distribution of the features, and statistical data, which is the average values and standard deviation of the features. In the case of R-frequency distribution, MPLearn, a machine learning-based image classification software developed in our laboratory, is used for comparison before and after aging treatment. In the case of statistical identification, MaterInfo, a web application developed in our laboratory, is used.

The classification rate calculated is the average of 10 repetitions of the classification process. The number of images used to create the classifier during the training phase is 30 for the comparison of R-frequency distributions, 96 for the training using statistics. The conditions of the feature values used in the classification in the T6 process are shown in Table 2.3. In condition (1), the mean, variance, and standard deviation of each value are used for classification. In condition (2), the minimum, maximum, median, mean and standard deviation are used for the equivalent circle diameter, lengths of long and narrow sides, aspect ratio and circularity. However, the area ratio and number density are constant values.

Table 2.3 Feature conditions using statistical values.

| | Condition (1) | Condition (2) |
|---|---|---|
| LN2D | ave, var | ave, var |
| IMFP | ave, std | ave, std |
| Area fraction | const | const |
| Number density | const | const |
| Diameter | mean, std | min, max, median, mean, std |
| Long side | mean, std | min, max, median, mean, std |
| Narrow side | mean, std | min, max, median, mean, std |
| Aspect ratio | mean, std | min, max, median, mean, std |
| Circularity | mean, std | min, max, median, mean, std |

## 2.4 Result and Discussion

### 2.4.1 Hardness

First, Fig. 2.6 shows the results of Vickers hardness measurements for the samples used in this experiment at each treatment stage. The results show that the sample at 3.6 *ks* has the highest hardness due to aging and the sample at 21.6 *ks* has the lowest hardness. It is considered that the precipitates became coarser and softer at 21.6 *ks* due to over-aging. The change in hardness indicates that the aging treatment changed the microstructures of the alloys.

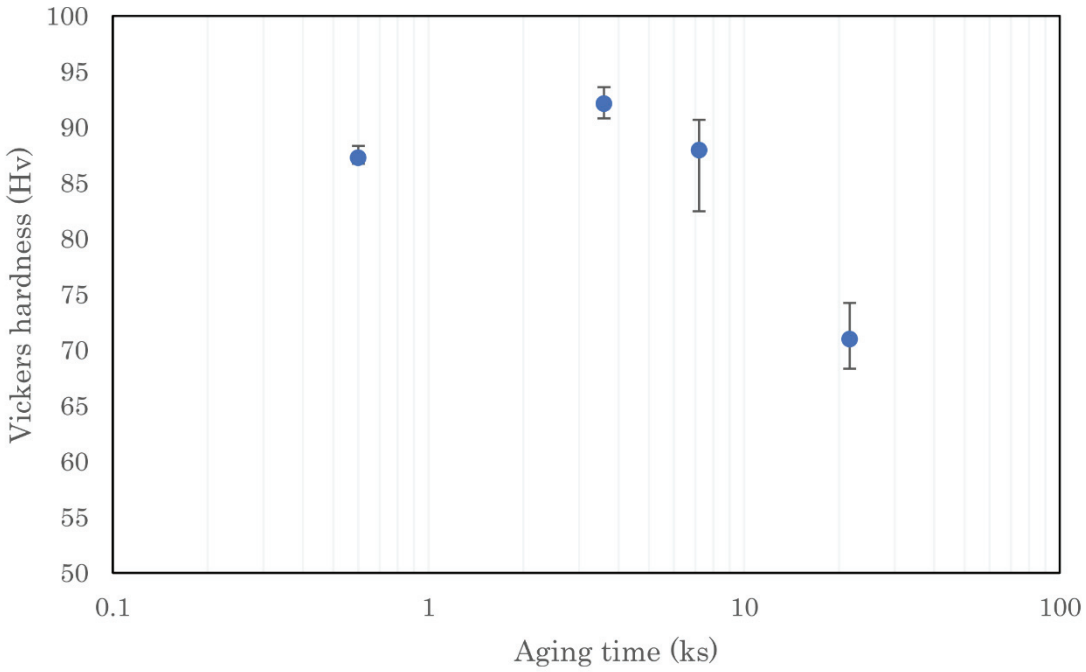


Fig. 2.6 Isothermal aging-hardness curve of Al-4%Si-0.5%Mg

### 2.4.2 Microstructures and binarization

The binarized microstructural images are shown in Fig. 2.7. Because the number of images used in the analysis is very large, an example of a binarized image from each process is shown here. Comparing the results in Fig. 2.7, there are significant differences between the microstructural images obtained by free casting and those obtained by other solution annealing and aging treatments, and it can be inferred that

they can be discriminated successfully. However, the solution annealing and aging images do not show significant differences.

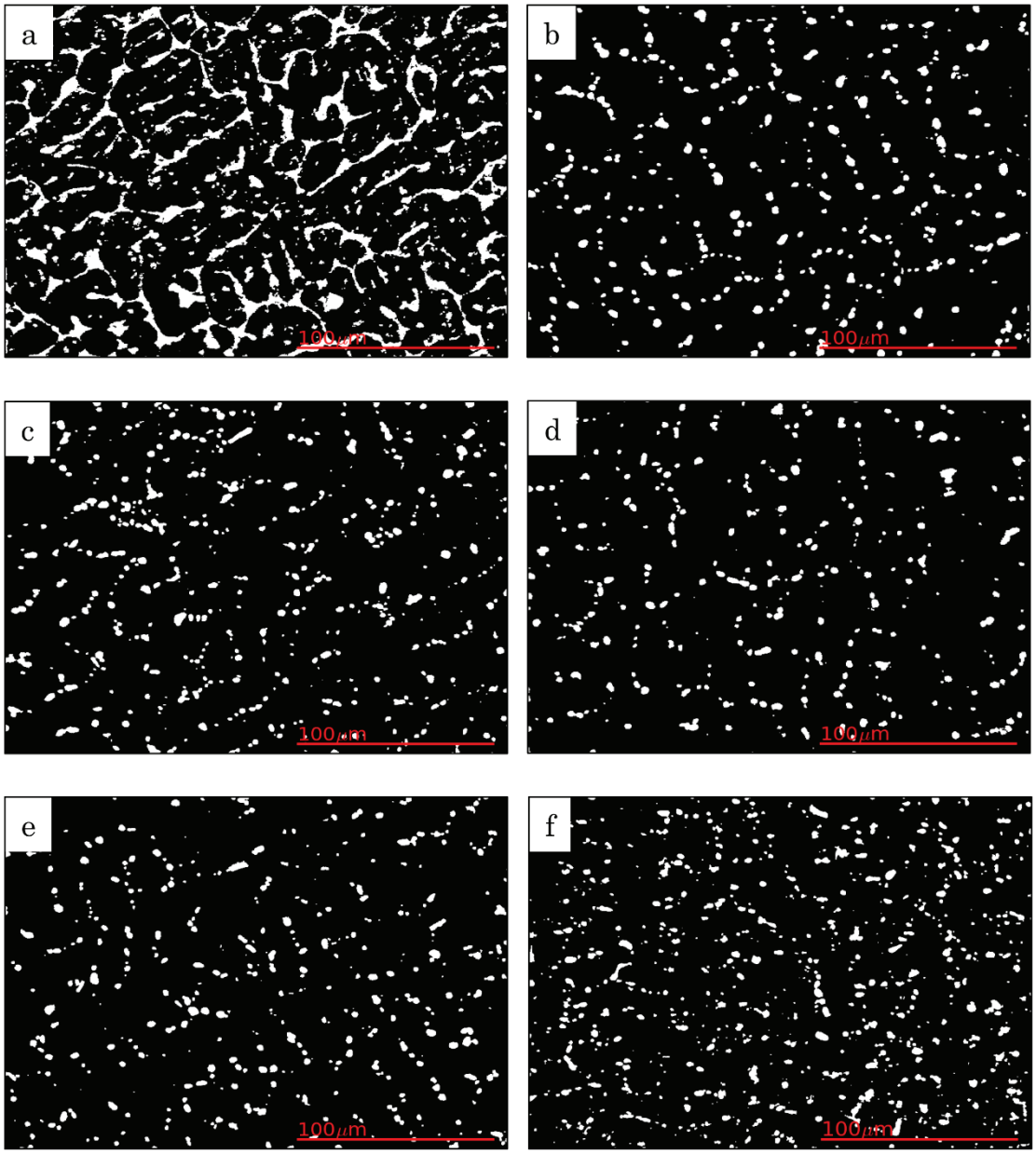


Fig. 2.7 Binary image of microstructure (a) after casting, (b) solution treatment, (c) aging treatment (0.6 ks), (d) aging treatment (3.6 ks), (e) aging treatment (7.2 ks), and (f) aging treatment (21.6 ks).

### 2.4.3 Classification results

Table 2.4-2.9 and Table 2.10-2.12 show the results of the two classification results using SVC and RFC for each of the conditions shown in Table 2.3, and the results for each test size for the solution annealing treatment and each aging treatment, respectively. Comparing the results in Tables 2.4-2.12, it can be said that the discrimination is possible because the classification rate is very high in the case of casting free and other treatments, regardless of which classifier is used, as can be inferred from the images of the experimental results. However, the rate of classification between solution annealing and each aging treatment was not high.

Fig. 2.6 shows that the hardness peaked at about 7.2 ks of aging time and then softened due to over aging, suggesting that aging precipitation occurred with aging treatment and then precipitated particles grew by Ostwald growth as the aging time progressed. However, the reason why the classification rate did not change as the aging time progressed is that the strengthening mechanism due to aging precipitation and the growth of particles due to over-aging could not be detected in the OM (400x) images because there were no significant differences in the binarized images. Another reason may be that the number of images provided as training data for classification was only 60, so machine learning was not able to properly recognize the number of features at each processing stage.

Therefore, Table 2.4-2.12 shows that the classification rate using statistics tended to be higher in the case of identification by SVM than in the case of classification by frequency distribution and statistics, respectively. This indicates that in the classification using SVM, statistical values detect differences in features for each treatment after the solution treatment better than frequency distributions. Since the frequency distribution uses the raw data obtained as it is, the amount of data is considerably larger than that using the statistics, and overlearning is considered to have occurred. On the other hand, no significant difference was observed when RF was used. This is because RF is one of the ensembles learning methods and has characteristics that make it more difficult to overlearn than SVM. Furthermore, when we focused on

the classification results obtained by changing the Test size, the classification rate tended to be higher when the Test size was smaller overall. This is thought to be due to the fact that a smaller Test size can handle a larger number of images as training data. Next, a comparison of the classification rates among the classifiers shows that the RFC-based classifier has better classification accuracy overall. Therefore, it can be said that RFC is more useful in the classification of organizations at each stage of T6 processing, as in this study.

Table 2.4 Classification results using SVM (R-frequency).

| | As cast | Solution treatment | Aging treatment (0.6 ks) | Aging treatment (3.6 ks) | Aging treatment (7.2 ks) |
|---|---|---|---|---|---|
| As cast | — | — | — | — | — |
| Solution treatment | 95.0 | — | — | — | — |
| Aging treatment (0.6 ks) | 100 | 50.0 | — | — | — |
| Aging treatment (3.6 ks) | 100 | 60.0 | 60.0 | — | — |
| Aging treatment (7.2 ks) | 100 | 55.0 | 60.0 | 60.0 | — |
| Aging treatment (21.6 ks) | 100 | 35.0 | 75.0 | 50.0 | 40.0 |

Table 2.5 Classification results using SVM under condition 1 (Test size 0.3).

| | As cast | Solution treatment | Aging treatment (0.6 ks) | Aging treatment (3.6 ks) | Aging treatment (7.2 ks) |
|---|---|---|---|---|---|
| As cast | — | — | — | — | — |
| Solution treatment | 100 | — | — | — | — |
| Aging treatment (0.6 ks) | 98.3 | 71.1 | — | — | — |
| Aging treatment (3.6 ks) | 99.4 | 60.5 | 62.8 | — | — |
| Aging treatment (7.2 ks) | 100 | 66.7 | 68.3 | 47.8 | — |
| Aging treatment (21.6 ks) | 100 | 61.7 | 64.5 | 47.2 | 45.0 |

Table 2.6 Classification results using SVM under condition 1 (Test size 0.1).

| | As cast | Solution treatment | Aging treatment (0.6 ks) | Aging treatment (3.6 ks) | Aging treatment (7.2 ks) |
|---|---|---|---|---|---|
| As cast | — | — | — | — | — |
| Solution treatment | 100 | — | — | — | — |
| Aging treatment (0.6 ks) | 100 | 70.0 | — | — | — |
| Aging treatment (3.6 ks) | 100 | 67.1 | 68.3 | — | — |
| Aging treatment (7.2 ks) | 100 | 66.7 | 60.0 | 61.7 | — |
| Aging treatment (21.6 ks) | 100 | 65.0 | 71.7 | 40.0 | 50.6 |

Table 2.7 Classification results using RF (R-frequency).

| | As cast | Solution treatment | Aging treatment (0.6 ks) | Aging treatment (3.6 ks) | Aging treatment (7.2 ks) |
|---|---|---|---|---|---|
| As cast | — | — | — | — | — |
| Solution treatment | 100 | — | — | — | — |
| Aging treatment (0.6 ks) | 100 | 60.0 | — | — | — |
| Aging treatment (3.6 ks) | 100 | 75.0 | 70.0 | — | — |
| Aging treatment (7.2 ks) | 100 | 50.0 | 60.0 | 60.0 | — |
| Aging treatment (21.6 ks) | 100 | 60.0 | 70.0 | 50.0 | 50.0 |

Table 2.8 Classification results using RF under condition 1 (Test size 0.3).

| | As cast | Solution treatment | Aging treatment (0.6 ks) | Aging treatment (3.6 ks) | Aging treatment (7.2 ks) |
|---|---|---|---|---|---|
| As cast | — | — | — | — | — |
| Solution treatment | 100 | — | — | — | — |
| Aging treatment (0.6 ks) | 99.4 | 84.4 | — | — | — |
| Aging treatment (3.6 ks) | 100 | 81.1 | 62.7 | — | — |
| Aging treatment (7.2 ks) | 100 | 73.9 | 55.0 | 49.4 | — |
| Aging treatment (21.6 ks) | 100 | 75.0 | 65.6 | 43.3 | 43.3 |

Table 2.9 Classification results using RF under condition 1 (Test size 0.1).

| | As cast | Solution treatment | Aging treatment (0.6 ks) | Aging treatment (3.6 ks) | Aging treatment (7.2 ks) |
|---|---|---|---|---|---|
| As cast | — | — | — | — | — |
| Solution treatment | 100 | — | — | — | — |
| Aging treatment (0.6 ks) | 100 | 86.7 | — | — | — |
| Aging treatment (3.6 ks) | 100 | 86.7 | 50.0 | — | — |
| Aging treatment (7.2 ks) | 100 | 78.3 | 55.0 | 43.3 | — |
| Aging treatment (21.6 ks) | 100 | 73.3 | 63.4 | 43.3 | 49.4 |

Table 2.10 Classification results using SVC under condition 2 (Test size 0.3).

| | As cast | Solution treatment | Aging treatment (0.6 ks) | Aging treatment (3.6 ks) | Aging treatment (7.2 ks) |
|---|---|---|---|---|---|
| As cast | — | — | — | — | — |
| Solution treatment | 100 | — | — | — | — |
| Aging treatment (0.6 ks) | 100 | 69.5 | — | — | — |
| Aging treatment (3.6 ks) | 100 | 66.1 | 54.4 | — | — |
| Aging treatment (7.2 ks) | 100 | 68.3 | 60.0 | 50.6 | — |
| Aging treatment (21.6 ks) | 100 | 67.8 | 60.0 | 57.2 | 57.8 |

Table 2.11 Classification results using SVC under condition 2 (Test size 0.1).

| | As cast | Solution treatment | Aging treatment (0.6 ks) | Aging treatment (3.6 ks) | Aging treatment (7.2 ks) |
|---|---|---|---|---|---|
| As cast | — | — | — | — | — |
| Solution treatment | 100 | — | — | — | — |
| Aging treatment (0.6 ks) | 100 | 66.8 | — | — | — |
| Aging treatment (3.6 ks) | 100 | 63.3 | 55.0 | — | — |
| Aging treatment (7.2 ks) | 100 | 66.7 | 63.3 | 58.3 | — |
| Aging treatment (21.6 ks) | 100 | 61.7 | 61.7 | 50.0 | 60.0 |

Table 2.12 Classification results using RFC under condition 2 (Test size 0.3).

| | As cast | Solution treatment | Aging treatment (0.6 ks) | Aging treatment (3.6 ks) | Aging treatment (7.2 ks) |
|---|---|---|---|---|---|
| As cast | — | — | — | — | — |
| Solution treatment | 100 | — | — | — | — |
| Aging treatment (0.6 ks) | 100 | 80.6 | — | — | — |
| Aging treatment (3.6 ks) | 100 | 83.3 | 63.3 | — | — |
| Aging treatment (7.2 ks) | 100 | 77.8 | 62.2 | 53.9 | — |
| Aging treatment (21.6 ks) | 100 | 77.8 | 63.9 | 50.0 | 46.7 |

Table 2.13 Classification results using RFC under condition 2 (Test size 0.1).

| | As cast | Solution treatment | Aging treatment (0.6 ks) | Aging treatment (3.6 ks) | Aging treatment (7.2 ks) |
|---|---|---|---|---|---|
| As cast | — | — | — | — | — |
| Solution treatment | 100 | — | — | — | — |
| Aging treatment (0.6 ks) | 100 | 83.3 | — | — | — |
| Aging treatment (3.6 ks) | 100 | 83.3 | 63.4 | — | — |
| Aging treatment (7.2 ks) | 100 | 83.3 | 60.0 | 60.0 | — |
| Aging treatment (21.6 ks) | 100 | 76.7 | 61.7 | 51.7 | 38.3 |

Table 2.12 Classification results using RFC under condition 2 (Test size 0.3).

| | As cast | Solution treatment | Aging treatment (0.6 ks) | Aging treatment (3.6 ks) | Aging treatment (7.2 ks) |
|---|---|---|---|---|---|
| As cast | — | — | — | — | — |
| Solution treatment | 100 | — | — | — | — |
| Aging treatment (0.6 ks) | 100 | 80.6 | — | — | — |
| Aging treatment (3.6 ks) | 100 | 83.3 | 63.3 | — | — |
| Aging treatment (7.2 ks) | 100 | 77.8 | 62.2 | 53.9 | — |
| Aging treatment (21.6 ks) | 100 | 77.8 | 63.9 | 50.0 | 46.7 |

### 2.4.4 PCA results

The results of PCA are discussed below. Figures 2.8-2.12 show the PCA results for the castings with high classification rates and the other treatment stages. The first principal component contributes approximately 97% and the second principal component approximately 3% in this analysis. Thus, it can be seen that most of the information on classification is condensed in the first principal component alone. Therefore, we will focus on the first principal component in our discussion. The scatter plots of the principal component scores show that the scores of each pair of principal components are generally separated. The results in Figs. 2.8-2.12 indicate that the mean and standard deviation of IMFP are considered to contribute to the classification rate. Fig. 2.20 shows a comparison of the mean value and standard deviation of IMFP for the solution annealed and aged 10 minutes. This can be attributed to the spheronization of the eutectic Si phase due to the effect of solution annealing, as shown in Fig. 2.7. In other words, the IMFP value, which is the free path length, is larger in the solution-treated microstructure than in the as-cast microstructure because gaps are created between the eutectic Si due to this effect.

The PCA results comparing the solution annealed microstructures with the microstructures from the other treatments and the PCA results for each aging treatment are shown in Figs. 2.13-2.16 and 2.17-2.19. The contribution ratio and cumulative contribution ratio graphs shown in Figs. 2.13-2.16 and 2.17-2.19 indicate that the first main classification rate was higher for the combinations that did not have a high classification rate. The contribution ratio and cumulative contribution ratio graphs shown in Figs. 2.13-2.16 and 2.17-2.19 indicate that the first principal component contributes approximately 80% and the second principal component contributes approximately 20% for the combinations that did not obtain a high discrimination ratio. Therefore, it can be seen that most of the information on classification is reduced by the first and second principal components alone. Therefore, we will discuss the first and second principal components. Figures 2.13-2.19 show that the scatter plots of the

principal component scores do not show any bias in the scores of each pair of principal components for each sample. Looking at the feature values contributing to each principal component, the first principal component is the mean value of IMFP, and the second principal component is the variance value of LN2DR. Fig. 2.21 shows a comparison of the measured values of these features. Fig. 2.21 shows that there is no bias in the measured values of the feature values that contribute to classification in each sample. Therefore, machine learning is not able to recognize and classify the trend of the feature values well in the classification of the microstructures after solution annealing treatment.

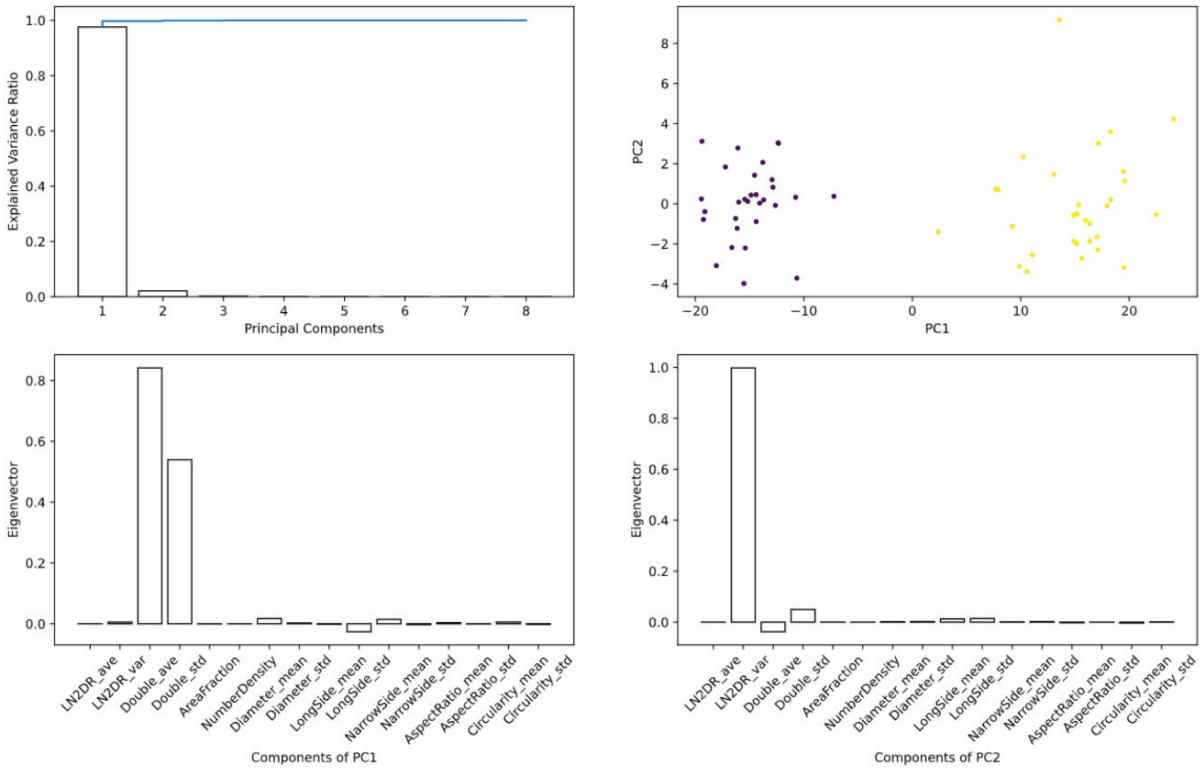


Fig. 2.8 Principal component analysis results for the combination of alloy as cast and after solution treatment.

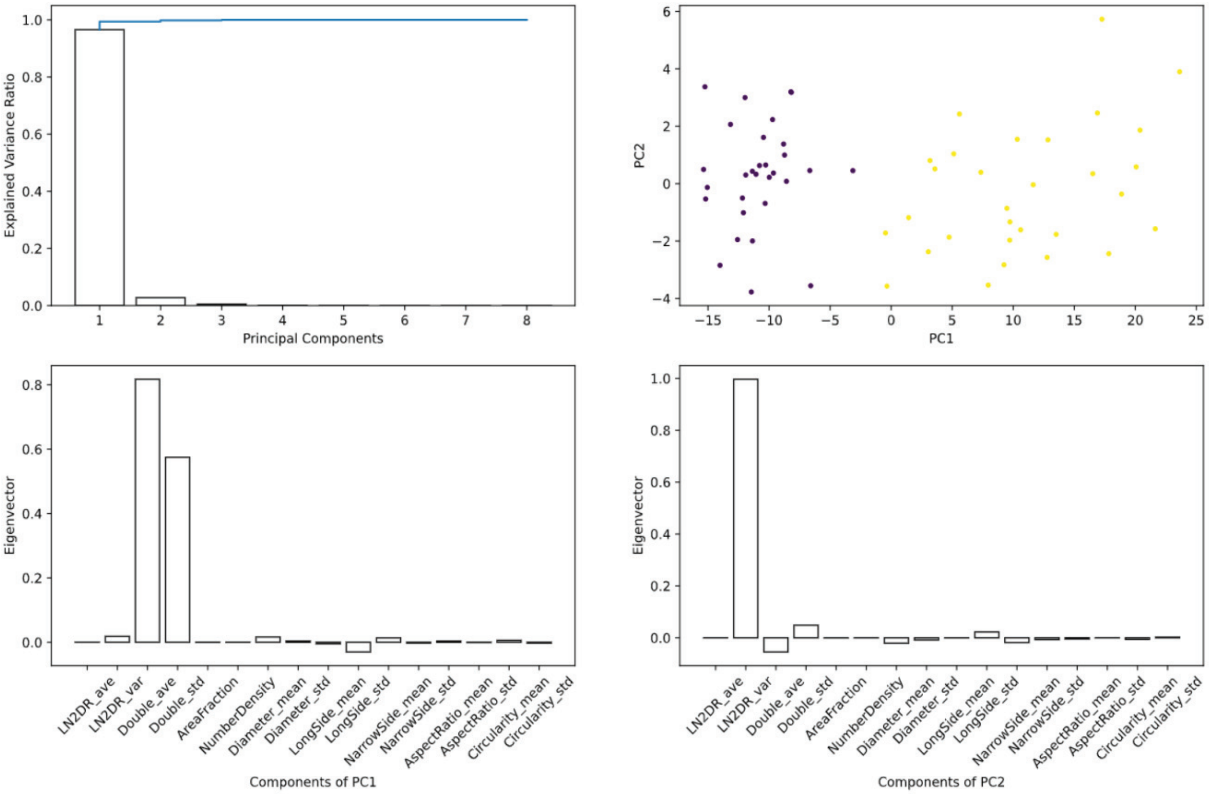


Fig. 2.9 Principal component analysis results for the combination of alloy as cast and after aging treatment (0.6 ks).

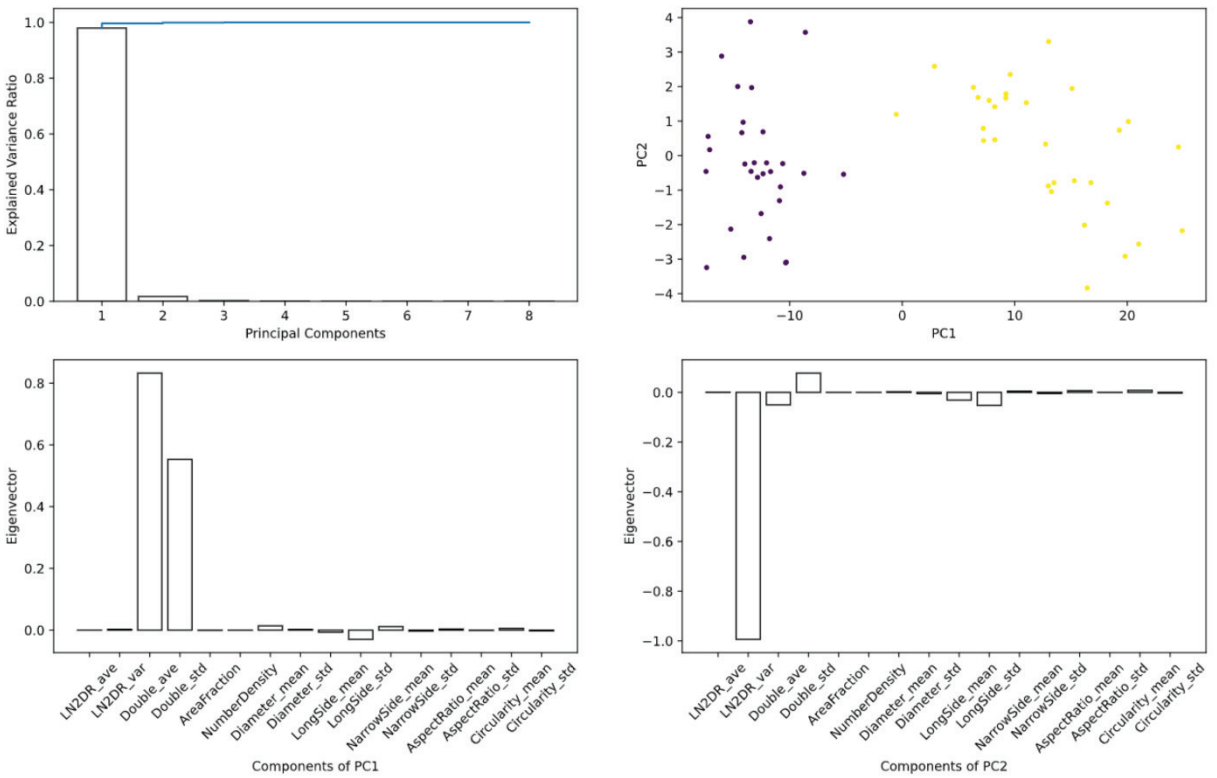


Fig. 2.10 Principal component analysis results for the combination of alloy as cast and after aging treatment (3.6 ks).

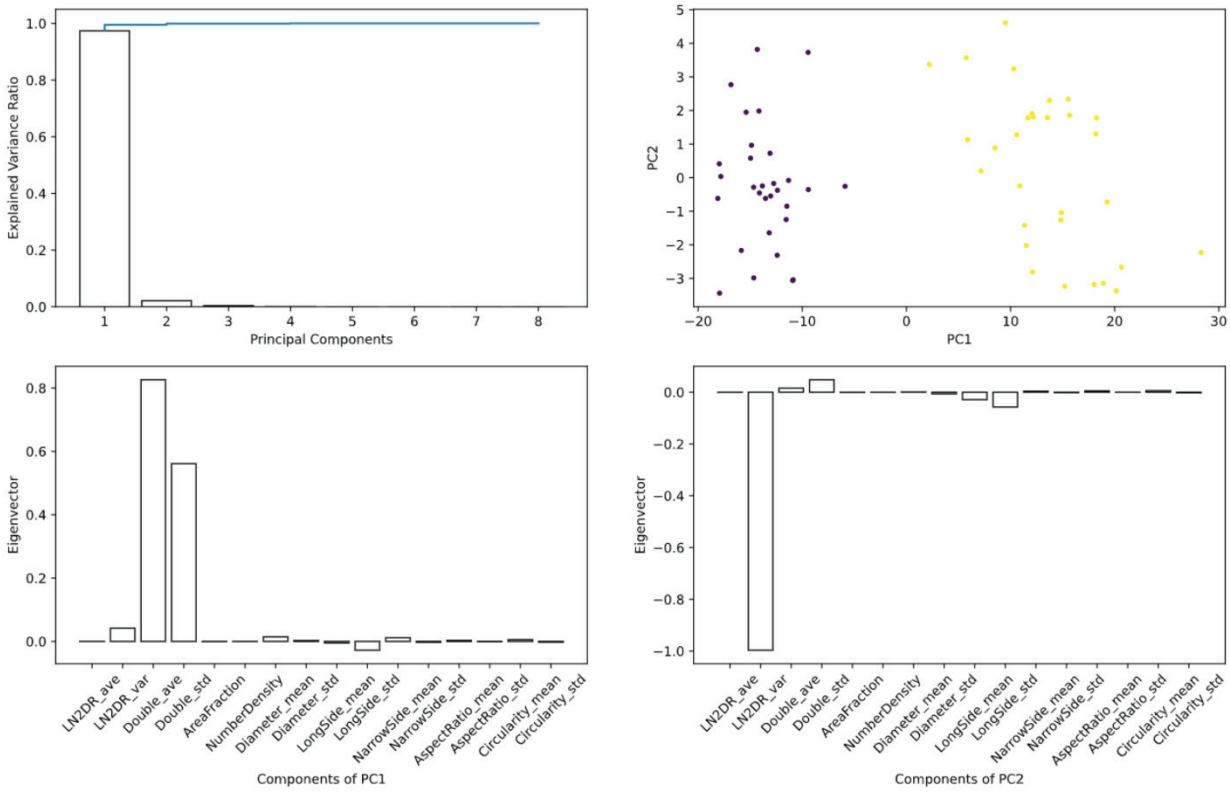


Fig. 2.11 Principal component analysis results for the combination of alloy as cast and after aging treatment (7.2 ks).

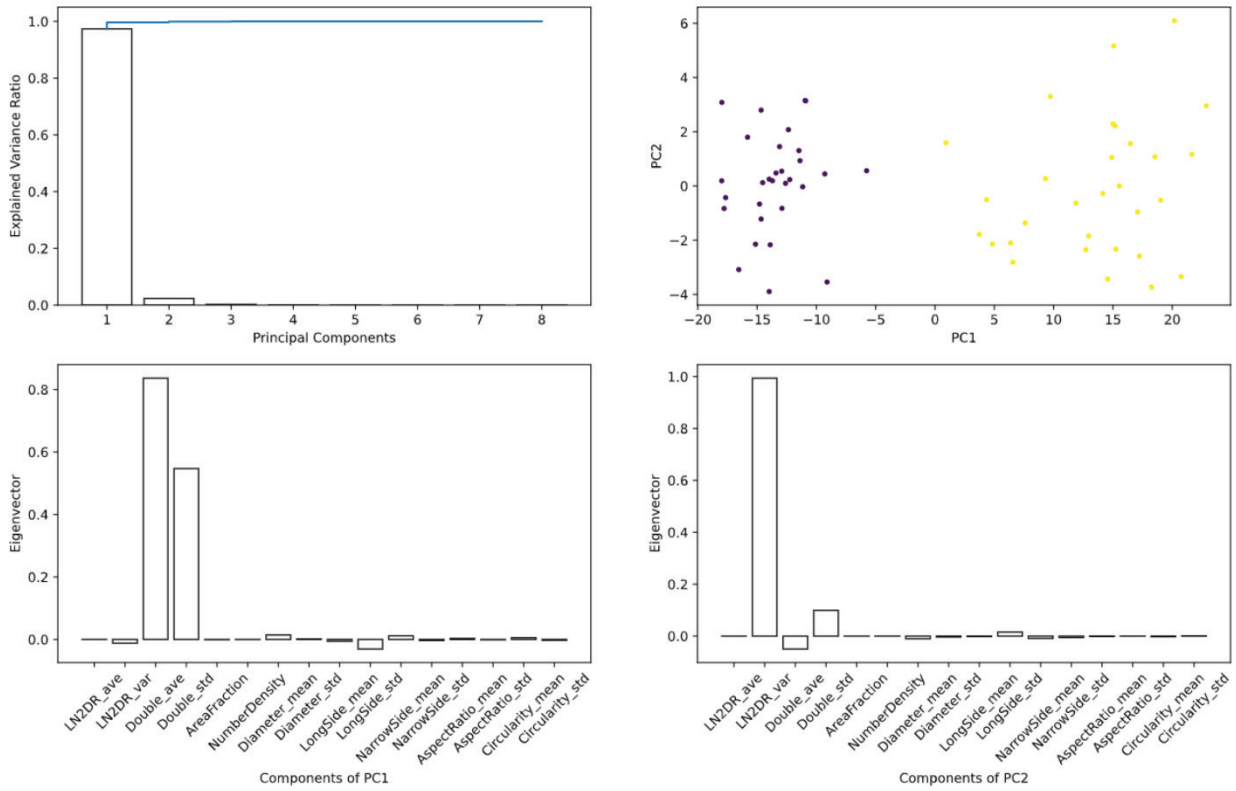


Fig. 2.12 Principal component analysis results for the combination of alloy as cast and after aging treatment (21.6 ks).

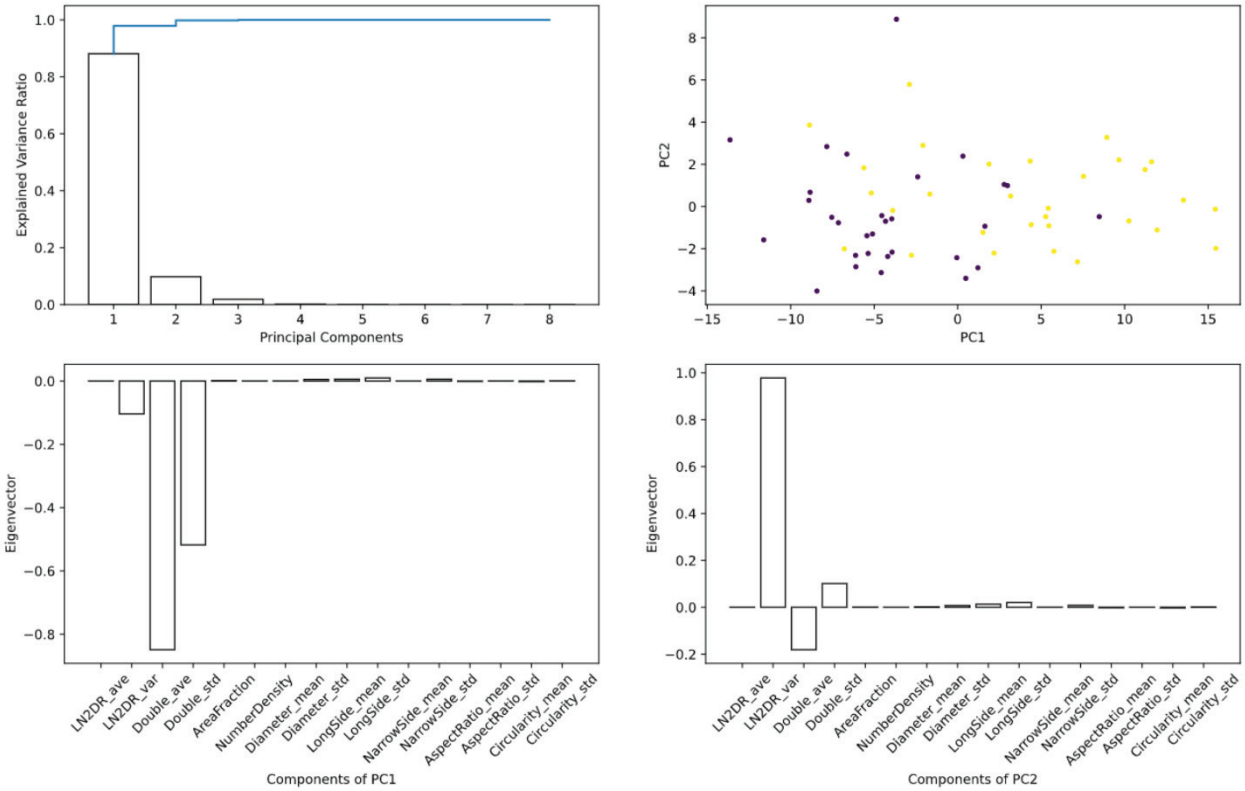


Fig. 2.13 Principal component analysis results for the combination of alloy after solution treatment and aging treatment (0.6 ks).

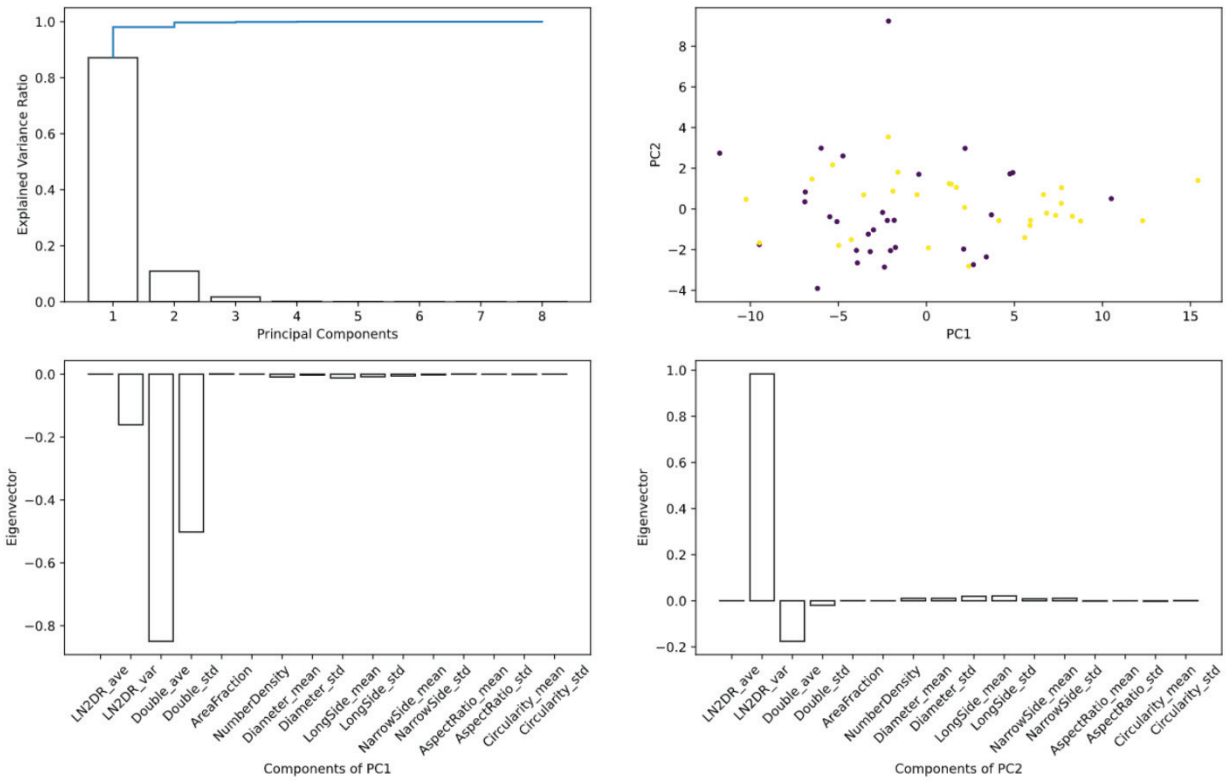


Fig. 2.14 Principal component analysis results for the combination of alloy after solution treatment and aging treatment (3.6 ks).

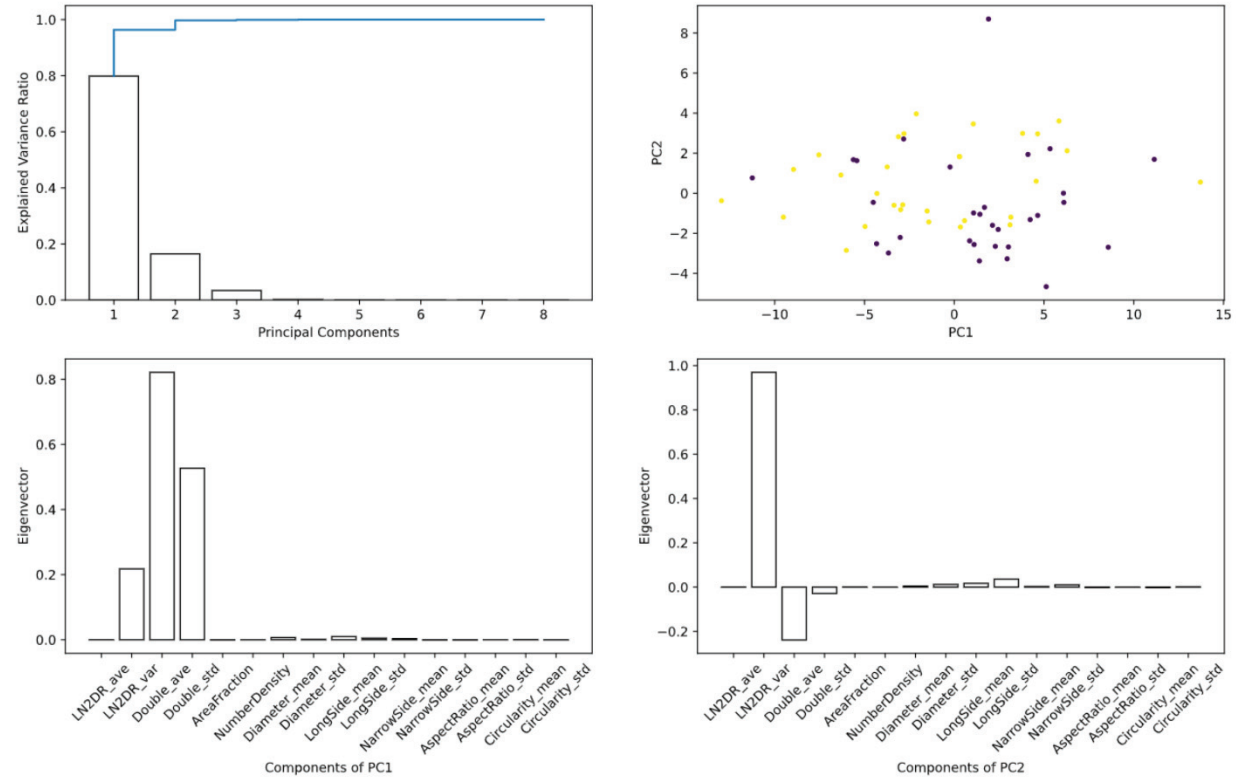


Fig. 2.15 Principal component analysis results for the combination of alloy after solution treatment and aging treatment (7.2 ks).

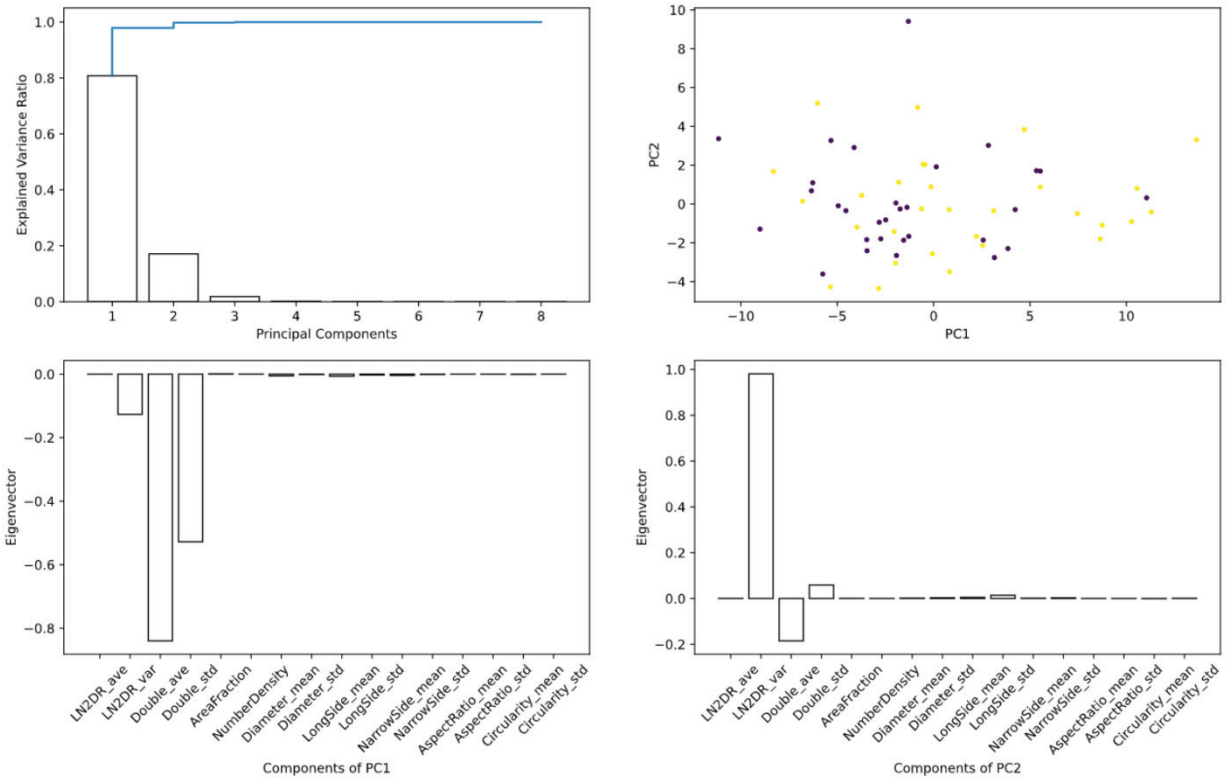


Fig. 2.16 Principal component analysis results for the combination of alloy after solution treatment and aging treatment (21.6 ks).

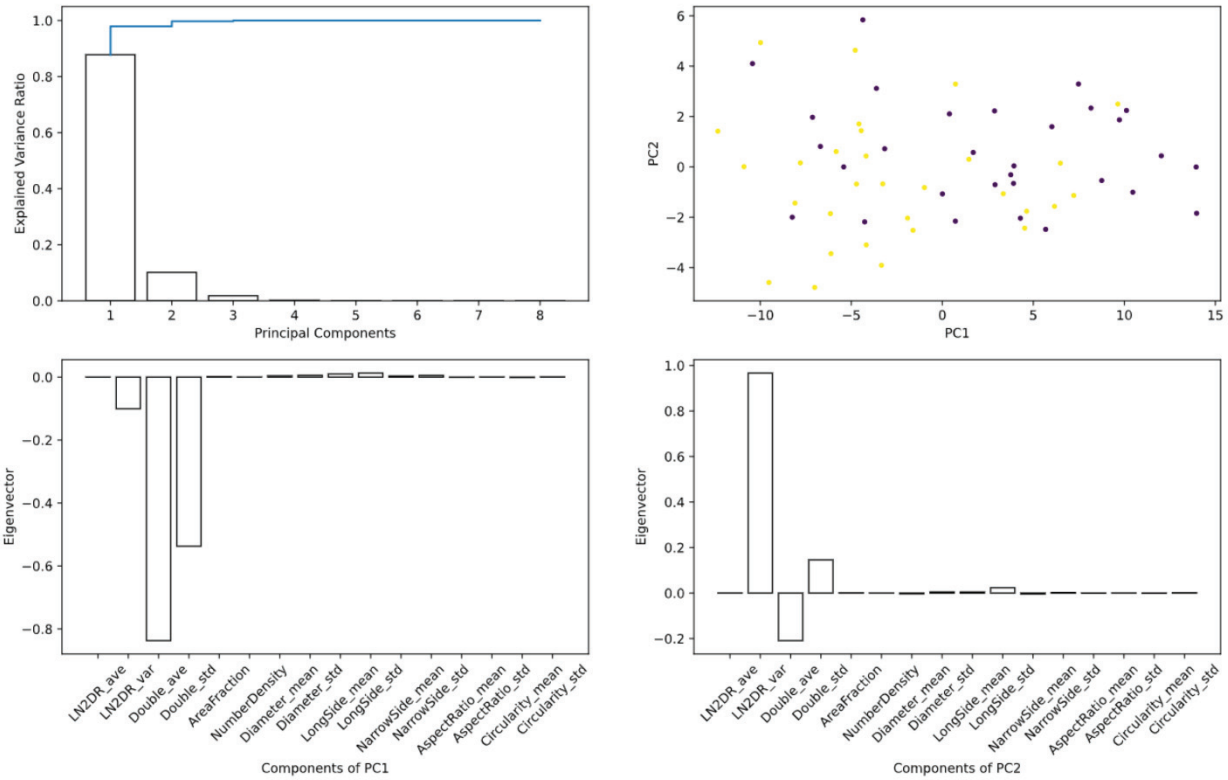


Fig. 2.17 Principal component analysis results for the combination of alloy after aging treatment (0.6 ks) and aging treatment (21.6 ks).

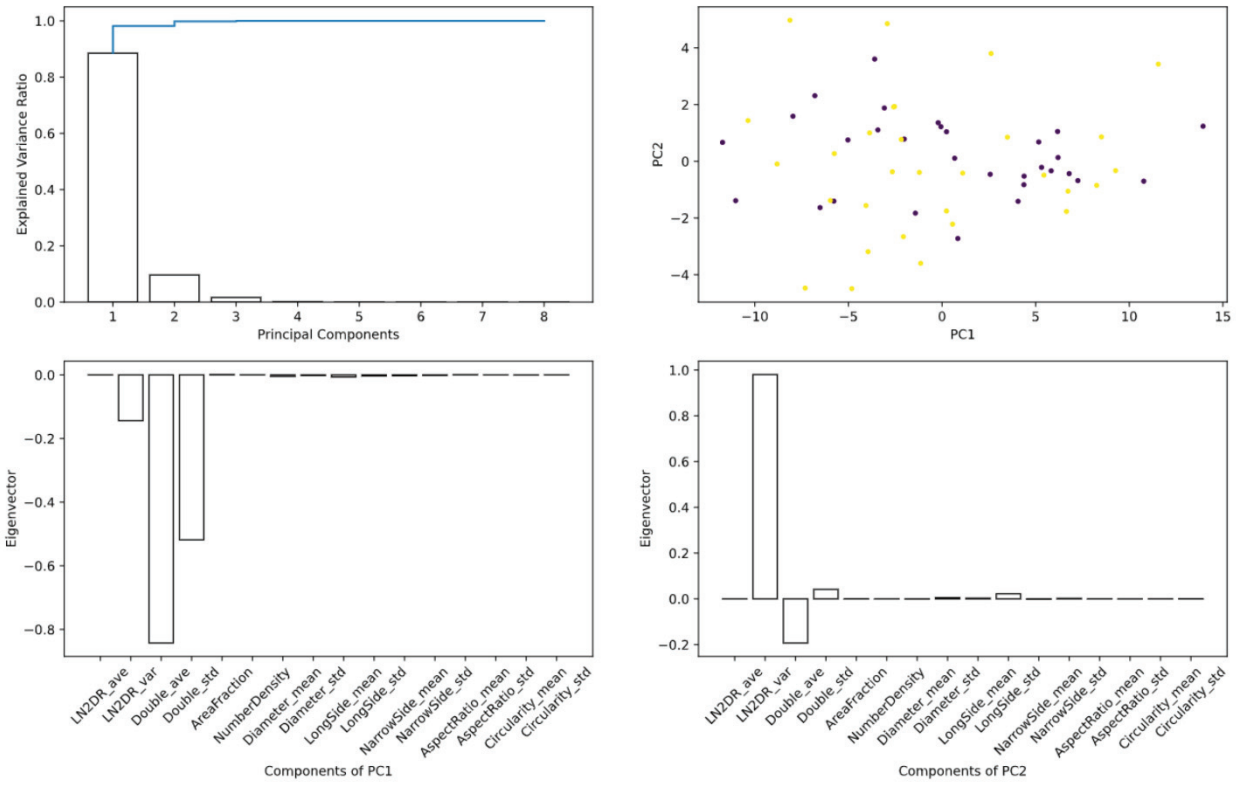


Fig. 2.18 Principal component analysis results for the combination of alloy after aging treatment (3.6 ks) and aging treatment (21.6 ks).

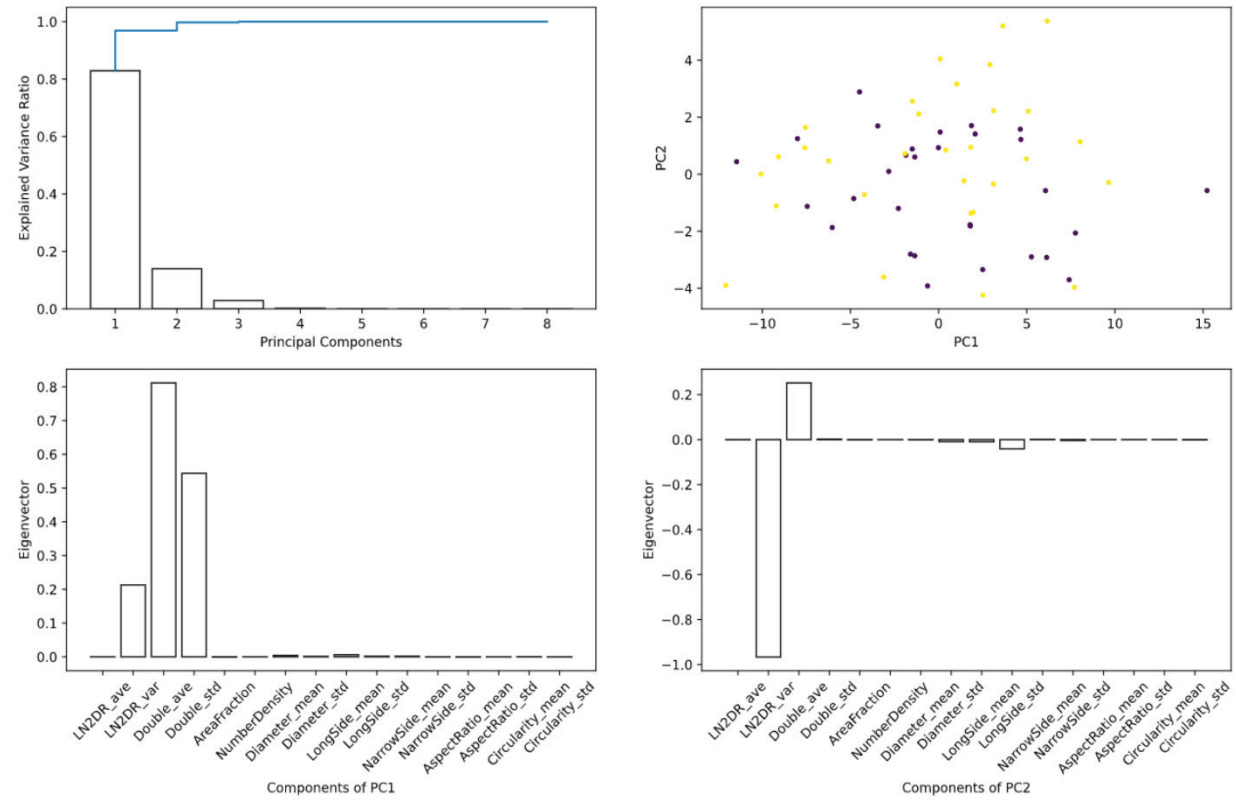


Fig. 2.19 Principal component analysis results for the combination of alloy after aging treatment (7.2 ks) and aging treatment (21.6 ks).

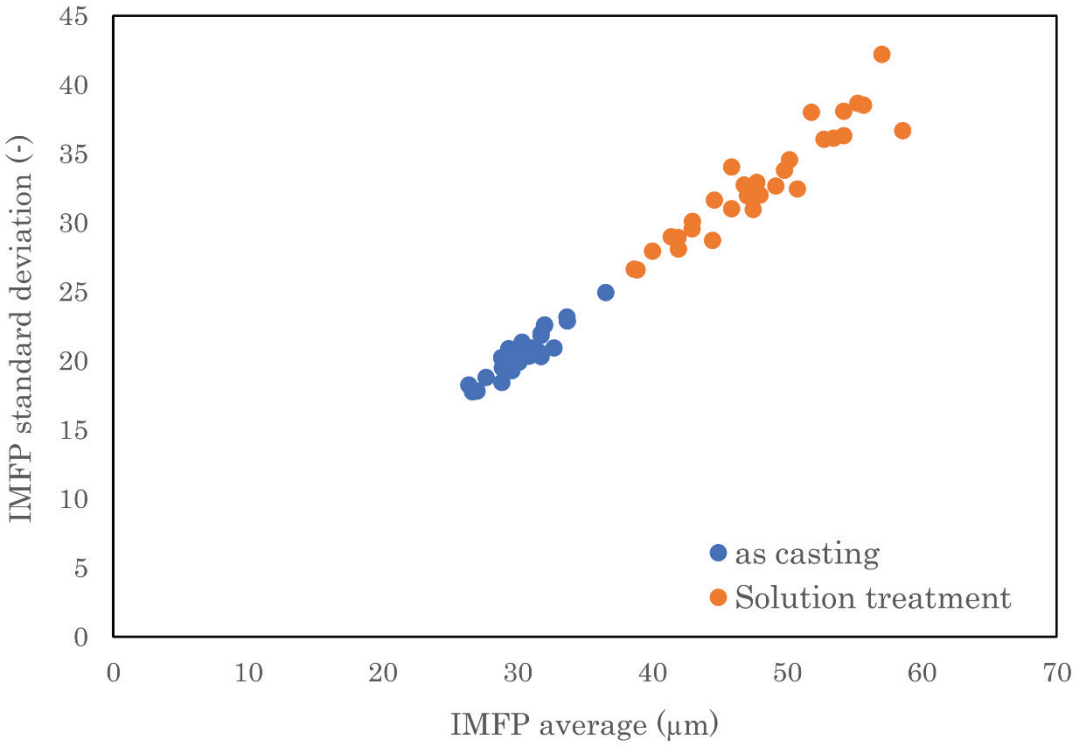


Fig. 2.20 Relationship between average of IMFP and standard deviation of IMFP Double in after as cast and aging treatment (0.6 ks).

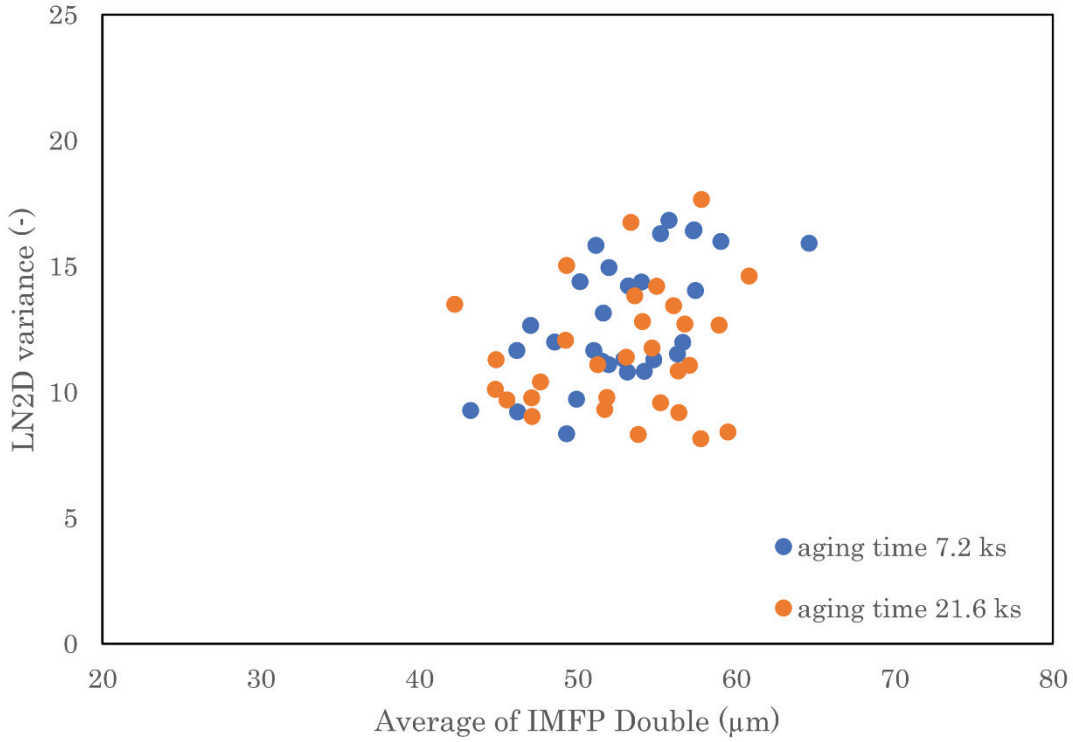


Fig. 2.21 Relationship between LN2D variance and average of IMFP Double in after aging treatment (7.2 ks) and aging treatment (21.6 ks).

## 2.5 Summary

In this chapter, we attempted to apply a machine learning-based image classification technique to classify microstructures at each stage of the T6 process. The Al-4 %Si-0.5 %Mg alloy was subjected to cast, solution treatment, and aging times of 0.6, 3.6, 7.2, and 21.6 ks, respectively. PCA was performed on each of the classification results to investigate the influence of the features on the classification. The results obtained are summarized as follows.

(1) A classification rate of 100% accuracy was obtained when comparing the microstructures from the casting and other T6 process stages. The feature values that contributed significantly to the classification were the average value and standard deviation of IMFP. This is because the solution treatment causes the eutectic Si-phase to become spherical that leading to the increase of the IMFP value, which is the free path length.

(2) In the case of classification using SVM, the classification rate was generally higher when statistical data were used. This is thought to be due to overlearning when the histogram data (frequency distribution of the features) is applied. Comparing the algorithms used for classification, the classification rate was higher when Random Forest was used as a classifier than SVM.

## Reference


1) C. Cortes and V. Vapnik, *Machine learning*, 1995, **20**, 273-297.

2) B. Scholkopf and A. J. Smola, *Learning with kernels: support vector machines, regularization, optimization, and beyond*, MIT press, 2018.

3) A. Liaw and M. Wiener, *R news*, 2002, **2**, 18-22.

4) R. Koker, N. Altinkok and A. Demir, *Materials & design*, 2007, **28**, 616-627.

5) M. Shabani, M. Alizadeh and A. Mazahery, *Fatigue & Fracture of Engineering Materials & Structures*, 2011, **34**, 1035-1040.

6) B. Hkdh, *ISIJ international*, 1999, **39**, 966-979.

7) A. Mangal and E. A. Holm, *Integrating Materials and Manufacturing Innovation*, 2018, **7**, 87-95.

8) T. M. Mitchell and T. M. Mitchell, *Machine learning*, McGraw-hill New York, 1997.

9) S. Lloyd, *IEEE transactions on information theory*, 1982, **28**, 129-137.

10) G. E. Hinton and S. Roweis, *Advances in neural information processing systems*, 2002, **15**.

11) L. Van der Maaten and G. Hinton, *Journal of machine learning research*, 2008, **9**.

12) K. Sugio, Y. Momota, D. Zhang, H. Fukushima and O. Yanagisawa, *Materials Transactions*, 2007, **48**, 2762-2767.

13) K. Sugio, S. Furukawa, T. Kengai, J. Tabata and G. Sasaki, *Materials Science Forum*, 2014, **783-786**, 240-245.

14) N. Cristianini and J. Shawe-Taylor, *An introduction to support vector machines and other kernel-based learning methods*, Cambridge university press, 2000.

15) B. E. Boser, I. M. Guyon and V. N. Vapnik, in *Proceedings of the fifth annual workshop on Computational learning theory*, 1992, pp. 144-152.

16) P. H. Chen, C. J. Lin and B. Schölkopf, *Applied Stochastic Models in Business and Industry*, 2005, **21**, 111-136.

17) L. Breiman, *Machine learning*, 2001, **45**, 5-32.

18) L. Breiman, J. H. Friedman, R. A. Olshen and C. J. Stone, *Classification and regression trees*, Routledge, 2017.

19) S. Wold, K. Esbensen and P. Geladi, *Chemometrics and intelligent laboratory systems*, 1987, **2**, 37-52.

# *Chapter 3*

# Microstructural Classification of Al-Si Alloy Casting at Different Cooling Rates with Machine Learning Techniques

## 3.1 Introduction

The microstructures of metallic material have a crucial impact on their properties. Therefore, the analysis of microstructure is one of the most important objects in the analysis of metallic materials.[1, 2] Traditionally, the classification of microstructure is mostly accomplished manually by human specialists, which will give rise to uncertainties because of the subjectivity. With the development of computer technology in recent years, various intelligent image analysis methods have emerged, providing new methods for microstructure analysis. As a result, there have been many attempts at classification and characterization of the microstructures by using machine learning techniques and related technology,[3-12] for the purpose of improving the accuracy and efficiency of microstructure analysis compared to the traditional methods.

Jessica Gola *et al.*[8] used data mining methods to demonstrate how to determine varying steel structures of two-phase steels though the evaluation of their morphological parameters. In the work of Seyed M. Azimi *et al.*[6] they proposed a Deep Learning method for microstructural classification in the examples of certain microstructural constituents of low carbon steel, and their system achieved a very high classification accuracy of more than 90%. Dmitry S. Bulgarevich *et al.*[7] reported a novel and extremely effective approach of pattern recognition in optical microscopic images of steels, that can do reliable and automated segmentation of typical steel microstructures based on a Random Forest statistical algorithm of machine learning. This method can help to handle the large volumes of image data in a short time for quality control and for the quest of new steels with desirable properties.

There have been many excellent achievements in the research of identifying and classifying the microstructure of steel. But the related research on aluminum alloy, which is a structural material as important as steel, is not much. The morphology and distribution of second phase particles play an important role in the mechanical properties of casting aluminum alloys.

In the previous work, we have defined a 2-dimensional local number, LN2D, and suggested the quantitative method to evaluate the particle spatial distribution by using the relative frequency distributions of LN2D.[13, 14] This method has been used to evaluate the spatial distributions of all SiC particles and the delaminated SiC particles in the Al-SiC composites, for the purpose of investigating the effect of the volume fraction of second-phase particles on the distribution of damaged particles and its relation to the tensile deformation behavior.[15, 16]

And we also proposed a statistical method to evaluate the mean free path of dislocation motion by using image processing, which is called image mean free path (IMFP), and investigated the relationship between the measured mean free path and mechanical properties of Al-Si casting alloys.[17]

In this work, we attempted to classify the microstructures of aluminum-silicon alloys at different cooling rates by using these originally developed methods and machine learning techniques, hope to help improve the accuracy and efficiency of microstructural analysis for quality control and for the design of new aluminum alloys with desirable properties.

## 3.2 Experimental process and material

The flow chart of the experimental process using machine learning techniques is illustrated in Fig. 3.1. The material used in this experiment was Al-7%Si-0.3%Mg (wt%) alloy, casting by the mixture of pure aluminum, Al-24.3%Si (wt%) and Al-10%Mg (wt%) ingots. Three samples solidified in different cooling rates were casting in a copper mold. After the preparation and polishing of samples, a large number of images of samples microstructures were taken by optical microscopy. Before the later steps, the image binarization has to be accomplished first. In the next stage, the features representing the morphology and distribution of second phase particles could be extracted from the binary images. Finally, the implement of classification process can be carried out by using the classifiers of SVM and Random Forest, based on the features extracted.

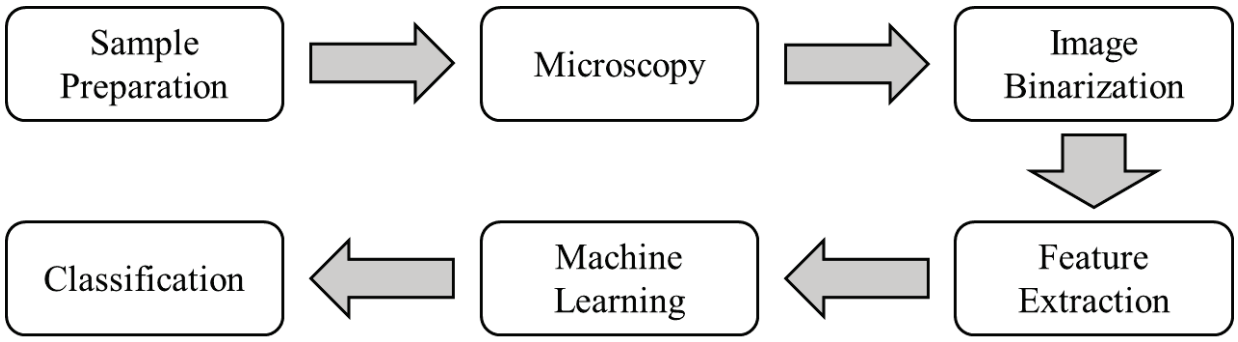


Fig. 3.1 The flow chart of experimental process in this work.

### 3.2.1 Casting process

A copper mold that can be heated up was used to make the samples solidify in different cooling rates. Three sample ingots were cast in the copper mold when it was not heated (room temperature), heated up to 80°C and heated up to 140°C, respectively. The sample 1 was solidified in the mold heated up to 140°C, the sample 2 was solidified in the mold heated up to 80°C, and the sample 3 was solidified in the mold when it was not heated. A HIOKI machine of model LR8431 with a K-type thermocouple was used to record

the temperature change with time during the casting process, so that the cooling curves, by which cooling rates can be calculated, can be drawn.

### 3.2.2 Microstructural characterization and machine learning process

For the characterization of microstructures of three samples, the samples were cut though the cross-section from the long strip sample ingots. The specimens were ground with 400 to 2000 grit SiC abrasive paper, and then polished carefully by using 3 and 1 μm diamond suspension into a smooth mirror surface, in order to prevent the influences of scratches in later process. Hundreds of microstructure images of each sample will be shot by 400x optical microscopy in the central area of observation surface, preparing for the later treatment. The resolution of each image was 1280 x 960 pixel.

The details of following image binarization, feature extraction, and classification phase have been discussed in Chaper 2.

### 3.2.3 Mechanical properties test

The tensile tests were carried out by a Shimadzu tensile testing machine with a load of 2500kgf at a stretching speed of 0.5mm/min. Vickers hardness tests were performed on the central area of cross-section of the casting sample ingots using a load of 3kgf holding for 10 s.

## 3.3 Results and Discussions

### 3.3.1 Cooling curves

The measured cooling curves of three samples were shown in the Fig. 3.2. The cooling rate can be defined by dT/dt computed from the approximately straight-line portion during the later stages of primary dendrite growth. The calculated cooling rates of three samples were 5.7 K/s, 8.0 K/s and 9.5 K/s, respectively. The sample 1 gained the lowest cooling rate, while the sample 3 obtained the highest cooling rate. But the gaps between the samples were not large.

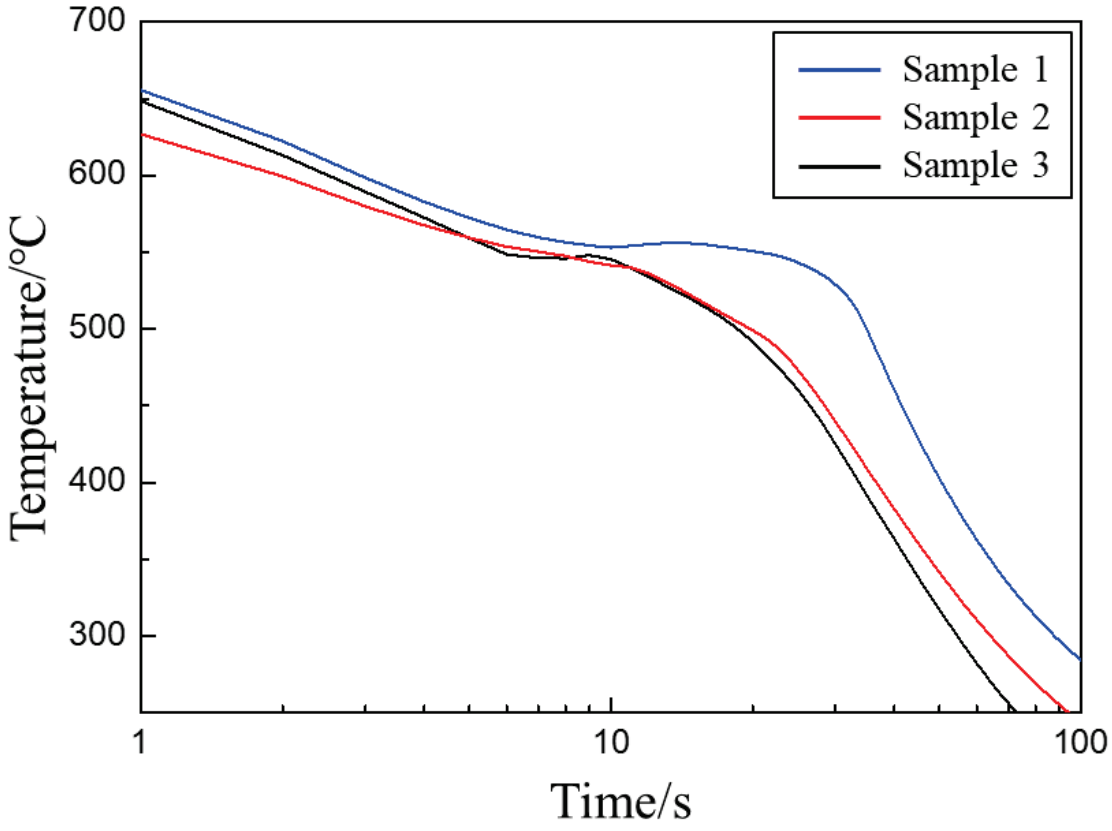


Fig. 3.2 The measured cooling curves of three samples.

### 3.3.2 Microstructures and mechanical properties

The microstructures of samples taken by optical microscopy was shown in Fig. 3.3, which were classic microstructures of Al-Si-Mg alloys. Microstructure analysis with dendrite arm spacing (DAS) is traditionally used in the Al-Si alloys. Rui CHEN *et al.*[18] found that secondary dendritic arm spacing of Al-Si-Mg alloy is very sensitive to cooling rate, and the size of SDAS decreases with the increase of cooling rate. Besides, the decrement of the size of second phase particles and DAS of Al-Fe-Si alloy with increasing cooling rate was reported by B. Dutta *et al.*[19] But in our work, it could be noticed that because of the approximate cooling rates, the microstructures of three samples were similar, which resulted in the classification of the microstructures was difficult by traditional methods.

The mechanical properties of samples were also proved the slight difference between three samples, which was shown in Fig. 3.4. Both the ultimate tensile strength and the average hardness of the samples were increased with the increase of cooling rates. The reason why the change in mechanical properties was so slight should be the approximate cooling rates of samples.

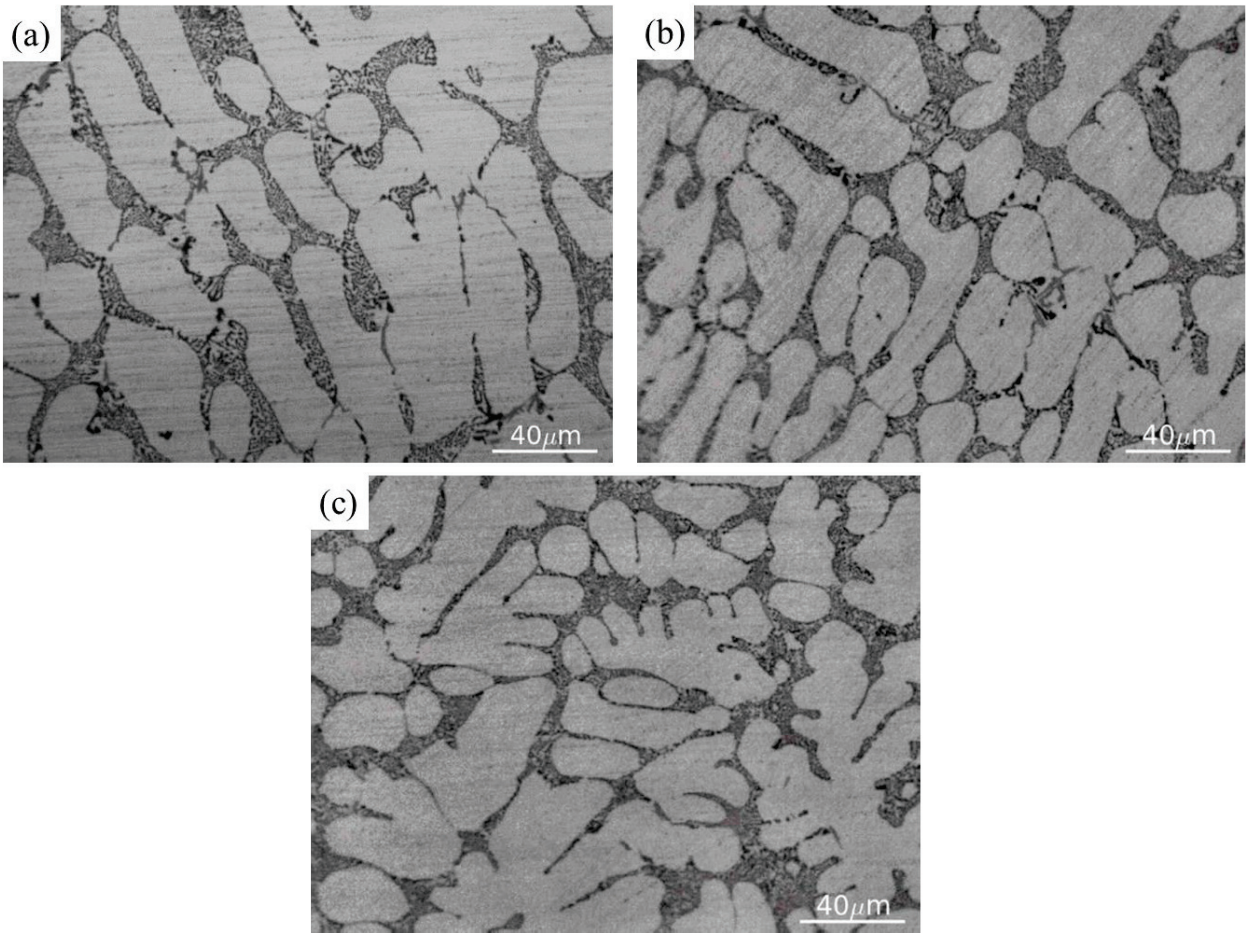


Fig. 3.3 Images of microstructures of Sample 1 (a), Sample 2 (b), and Sample 3 (c).

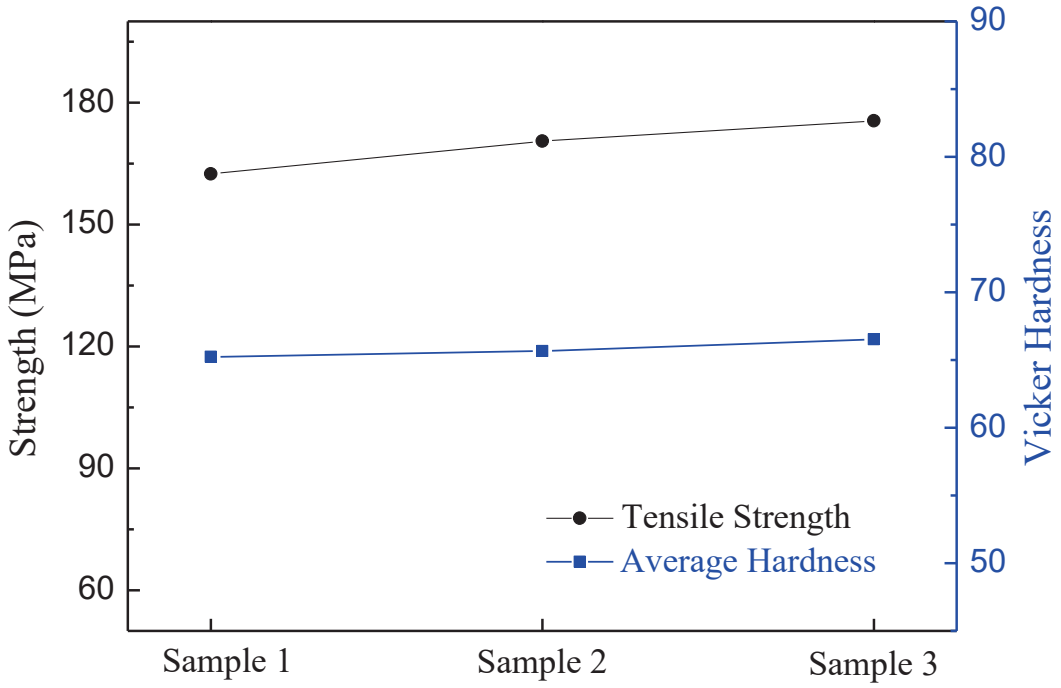


Fig. 3.4 Mechanical properties of the three samples.

### 3.3.3 Principal component analysis

We did the principal component analysis (PCA), trying to find out the difference of microstructures between the samples. The result was shown in Fig. 3.4, from where we can find that the most effective components were $LN2DR_{var}$ (Variance of LN2DR), $Long\ Side_{std}$ (standard deviation of Long Side), and $Narrow\ Side_{std}$ (standard deviation of Narrow Side), respectively. The variance of LN2DR ($LN2DR_{Var}$), average value of Long Side, Narrow Side ($Long\ Side_{Av}$ and $Narrow\ Side_{Av}$), and standard deviation of Long Side and Narrow Side ($Long\ Side_{std}$ and $Narrow\ Side_{std}$) of three samples were tested, and the results were shown in Table 3.1.

Table 3.1 The variance of LN2DR, average values of Long Side and Narrow Side, as well as standard deviation of Long Side and Narrow Side of three samples.

| | $LN2DR_{Var.}$ | $Long\ Side_{Av.}$ (μm) | $Long\ Side_{std.}$ | $Narrow\ Side_{Av.}$ (μm) | $Narrow\ Side_{std.}$ |
|---|---|---|---|---|---|
| Sample 1 | 20.06 | 8.22 | 12.45 | 4.45 | 6.75 |
| Sample 2 | 24.46 | 9.27 | 16.70 | 5.05 | 9.28 |
| Sample 3 | 28.13 | 8.31 | 17.93 | 4.59 | 10.59 |

The difference of values of $Long\ Side_{Av}$ and $Narrow\ Side_{Av}$ are almost negligible, demonstrating the similarity of the particle size between the samples. And it can be noticed that the difference of $LN2DR_{Var}$, $Long\ Side_{std}$ and $Narrow\ Side_{std}$ are much bigger, and have the increasing trends with the increase of cooling rates. As we know that the cooling rate will affect the nucleation and growth of eutectic phase particles. A higher cooling rate will accelerate the nucleation of aluminum and the eutectic phase, thereby making the eutectic phase particles in the eutectic region finer and dense. A shorter solidification time may result in a decrease in the uniformity of the microstructure. Although a slower cooling rate will result in a coarser crystal, a longer solidification time will increase the uniformity of the eutectic region. These may

explain that the average rate of Long Side and Narrow Side of the samples had very small differences, but standard deviation of which were obvious and increased with the cooling rates.

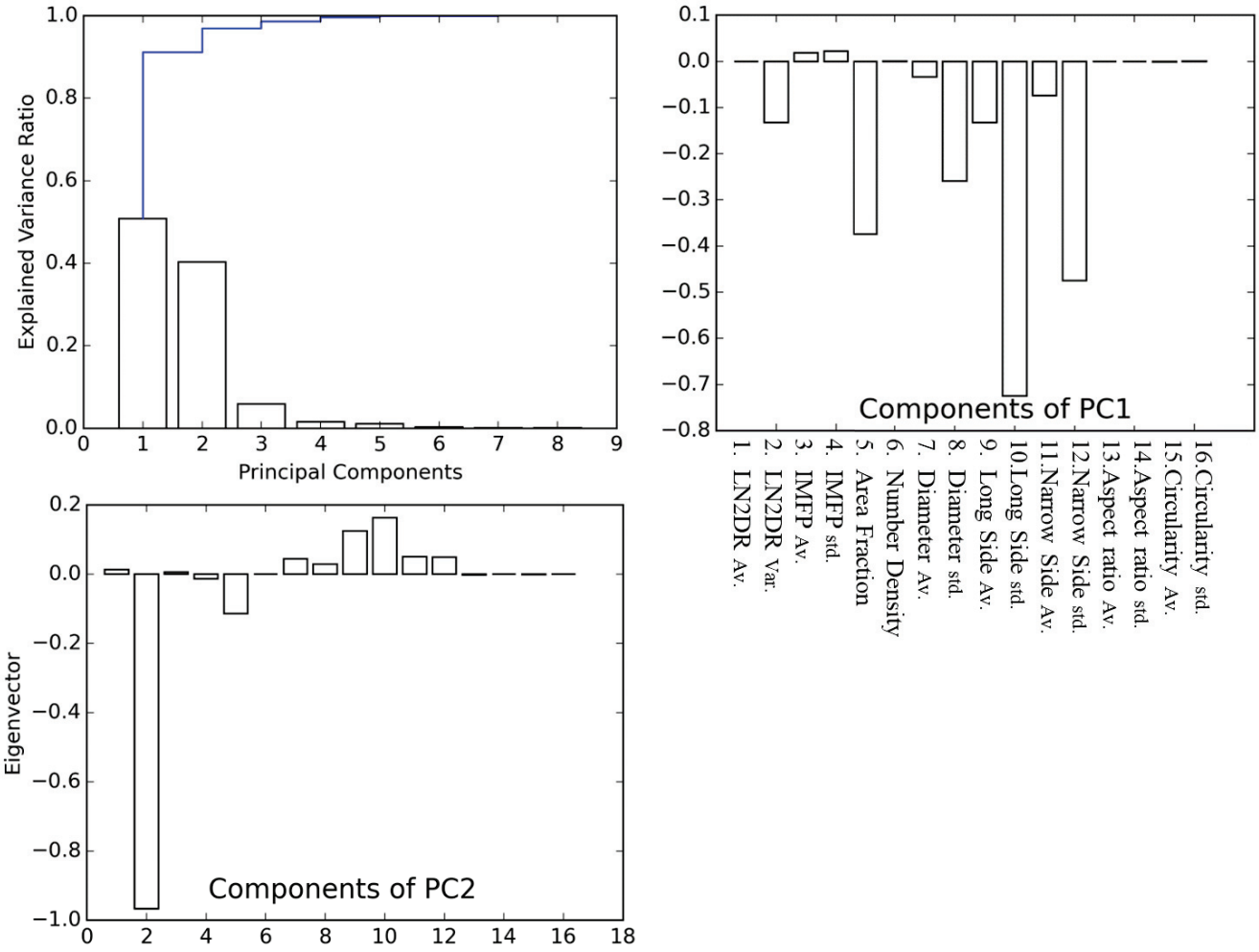


Fig. 3.5 The principal component analysis (PCA) of the samples, using 40 images for each sample.

### 3.3.4 Classification results and discussions

The number of images used for the training data was 80 (40 images of each sample), and the number used for the test data was 20 (10 images of each sample). And 4 groups of test data were set, while the result was the average rate of 4 tests to reduce the interference of special factors. We tested 2 sets of data for contrast, Sample 1 versus 2 and Sample 1 versus 3, respectively. The difference between Sample 1 and 3 was bigger than which between Sample 1 and 2. The result of classification was shown in Table 3.2. It can be noticed that the classification rate reached a high level of 80~90%. When using the histogram data, the classification rate of Random Forest was higher, while using the statistical data, the accuracy of SVM was higher. Besides, the classification rate of Sample 1 versus 3 was always higher than Sample 1 versus 2. The bigger difference of the cooling rates will cause the bigger difference of microstructures. As what we mentioned above, the standard deviation of some features was increased with the cooling rates. Therefore, appearance of the higher classification rates should be predictable.

And in this work, we want to figure out whether the number of micrographs for training will affect the result. Increasing the number of sample images can make the feature values more consistent with the features of the entire sample, but it will also increase processing time and reduce efficiency. Therefore, we hope to find the number of images most suitable for training data. And for this reason, we did the classification rate change with number of images in training data, the number was increased from 20 to 140. The results of classification rate change with number of images using in training data were shown in Fig. 3.6. Fig. 3.6 (a) and (b) were the results of using histogram data. The classification rate of Random Forest was increased when the number of training data increased to 60, and then dropped slightly. Fig. 3.6 (c) and (d) were the results of using statistical data. The classification rate was also increased when the number of training data raised to 60 and 80, furthermore, the classification rate of SVM had an overall increment of about 5~10%, got the highest rate. Based on these, it can be inferred that

60 or 80 should be a suitable number for training. When using the statistical data and SVM as the classifier, the highest accuracy in classification could be obtained in this work.

Table 3.2 The classification rate of three samples using different data type and classifier.

| Sample | Histogram Data | | Statistical Data | |
|---|---|---|---|---|
| | SVM | RF | SVM | RF |
| 1 *vs.* 2 | 70.00 | 85.75 | 82.50 | 81.75 |
| 1 *vs.* 3 | 85.00 | 87.75 | 90.00 | 84.75 |

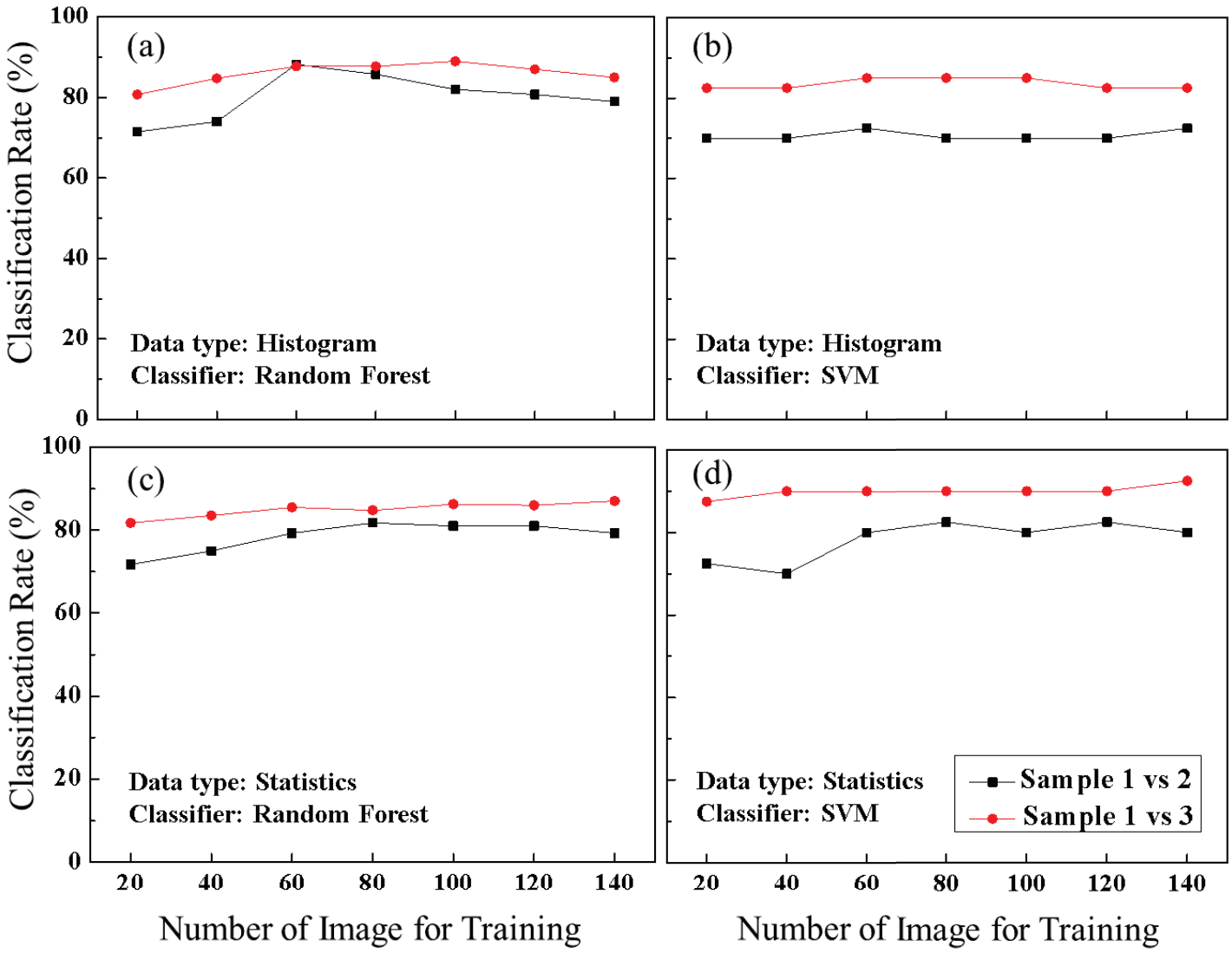

Fig. 3.6 The classification rates change with number of images used for training data.

## 3.4 Summary

In this chapter, the Al-7%Si-0.3%Mg alloys were solidified in a copper mold at three different cooling rates. The classification of the microstructures was accomplished by using machine learning techniques. The results were summarized as follows.

(1) The microstructures of the samples were similar because of the approximate cooling rates, so originally developed machine learning-based image classification techniques were used to detect the difference between the microstructures of the samples. The mechanical properties of the three samples were slightly increased with the increase of cooling rates, proving the differences between the samples.

(2) The classification of the microstructures was accomplished by using machine learning techniques, and high classification rates of about 80% to 90% were obtained. The classification rate was highest when using the statistical data and using SVM as classifier. Besides, the classification rate was higher when the difference of cooling rates of samples was bigger. In order to get the highest classification rate in shortest time, a suitable number of images for training was 60 to 80 during the machine learning process in this study.

## Reference


1) W. D. Callister Jr and D. G. Rethwisch, *Fundamentals of materials science and engineering: an integrated approach*, John Wiley & Sons, Hoboken, 2020.

2) E. Sjölander and S. Seifeddine, *Journal of Materials Processing Technology*, 2010, **210**, 1249-1259.

3) H. M. Tanveer, H. M. T. Mustafa, W. Asif, M. Ahmad, M. A. Javed and M. Ahmad, *science and engineering*, 2015, **1**, 3.

4) J. P. Papa, R. Y. M. Nakamura, V. H. C. de Albuquerque, A. X. Falcão and J. M. R. S. Tavares, *Expert Systems with Applications*, 2013, **40**, 590-597.

5) A. Chowdhury, E. Kautz, B. Yener and D. Lewis, *Computational Materials Science*, 2016, **123**, 176-187.

6) S. M. Azimi, D. Britz, M. Engstler, M. Fritz and F. Mucklich, *Scientific reports*, 2018, **8**, 2128.

7) D. S. Bulgarevich, S. Tsukamoto, T. Kasuya, M. Demura and M. Watanabe, *Scientific reports*, 2018, **8**, 1-8.

8) J. Gola, D. Britz, T. Staudt, M. Winter, A. S. Schneider, M. Ludovici and F. Mücklich, *Computational Materials Science*, 2018, **148**, 324-335.

9) B. Ma, X. Ban, H. Huang, Y. Chen, W. Liu and Y. Zhi, *Symmetry*, 2018, **10**, 107.

10) K. Tsutsui, H. Terasaki, T. Maemura, K. Hayashi, K. Moriguchi and S. Morito, *Computational Materials Science*, 2019, **159**, 403-411.

11) Z.-L. Wang and Y. Adachi, *Materials Science and Engineering: A*, 2019, **744**, 661-670.

12) J. Gola, J. Webel, D. Britz, A. Guitar, T. Staudt, M. Winter and F. Mücklich, *Computational Materials Science*, 2019, **160**, 186-196.

13) K. Sugio, Y. Momota, D. Zhang, H. Fukushima and O. Yanagisawa, *Materials Transactions*, 2007, **48**, 2762-2767.

14) K. Sugio, Y. Momota, D. Zhang, H. Fukushima and O. Yanagisawa, *Materials Transactions*, 2007, **48**, 2768-2777.

15) D. Zhang, K. Sugio, K. Sakai, H. Fukushima and O. Yanagisawa, *Materials Transactions*, 2007, **48**, 171-177.

16) D. Zhang, K. Sugio, K. Sakai, H. Fukushima and O. Yanagisawa, *Materials Transactions*, 2008, **49**, 661-670.

17) K. Sugio, S. Furukawa, T. Kengai, J. Tabata and G. Sasaki, *Materials Science Forum*, 2014, **783-786**, 240-245.

18) R. Chen, Y.-f. Shi, Q.-y. Xu and B.-c. Liu, *Transactions of Nonferrous Metals Society of China*, 2014, **24**, 1645-1652.

19) B. Dutta and M. Rettenmayr, *Materials Science and Engineering: A*, 2000, **283**, 218-224.

# *Chapter 4*

# Microstructural Classification of Unmodified and Strontium Modified Al-Si Casting Alloys with Machine Learning Techniques

## 4.1 Introduction

In recent years, reducing vehicle weight has become increasingly important based on legislation and environmental pressures on the automotive industry, which increasingly requires the production of lighter, more fuel-efficient vehicles with lower emissions. Al-Si casting alloys have been used commercially to produce important components such as engine blocks because of their high strength-to-weight ratio, excellent castability and corrosion resistance, and especially good mechanical properties under heat treatment conditions.[1)] High fatigue strength and good wear resistance are key properties for the life of engine blocks. Eutectic silicon particle size and morphology are thought to have an important influence on fatigue crack expansion behavior, and finer eutectic silicon particles are effective in improving fatigue crack expansion resistance.[2)]

The eutectic Si in untreated cast Al-Si alloys is usually in a plate-like morphology and coarse. Among the various methods to refine the size and morphology of eutectic Si, modification of cast Al-Si alloys by additive of modification elements is a common and easy to implement method, and has been widely used in industrial production for a long time.[3)] Many modifier elements such as Sb[4-6)], Sr[7-12)], Y[13)] and rare earth elements (Eu, Nd, Yb, etc.)[14-16)] have been shown to refine and improve the eutectic silicon phase in Al-Si casting alloys. Sr is one of the most commonly used modifiers, and the addition of Sr results in a fully modified fibrous eutectic-Si morphology.[17)]

Due to the effect of the modification on the eutectic silicon, the microstructures of the Al-Si alloy changes after the modification, which will eventually lead to changes in the mechanical properties of the alloy. Microstructural analysis is one of the most important parts in materials science. With the development of computer technology, more image analysis methods are available for microstructural analysis, which can significantly improve the efficiency of the process. In the present study, machine learning techniques were used to classify the microstructures of Al-Si-Mg alloys before and after Sr modification, and our original developed methods were used to quantitively analyze the

size and distribution of eutectic silicon in the matrix of the alloys before and after modification, and we also tried to relate these features, which represent the characteristics and distribution of the second phase, to the mechanical properties of the material.

## 4.2 Experimental process and material

### 4.2.1 Sample preparation

The material used in this experiment was Al-7%Si-0.3%Mg (wt%) casting alloy, and the alloy was modified with 0.01% and 0.02% (wt%) Sr by adding a certain amount of Al-10%Sr (wt%) master alloy. The molten alloy was well stirred and injected into a copper mold heated to 140 degrees Celsius and cooled naturally to room temperature in air, and the measured cooling rate was 5 K/s. The samples were rectangular in shape, and the core of the middle section of the casting was taken and cut into rectangles with a cross-section of about 10×10 mm for subsequent microstructure photography and mechanical property testing.

The cross section of the unmodified and modified samples was polished with waterproof abrasive paper and diamond grinding paste to observe the microstructure, and several microstructure photographs with 500x magnification were taken with an optical microscope for machine learning and classification. The resolution of each image was 1280 x 960 pixels.

### 4.2.2 Machine learning process

The machine learning process was shown in Chapter 2. The image data will be randomly divided into 2 parts, one part for training, and the other part for test. The original images will be turned into binary images though brightness adjustment, filtering and thresholding. Next, we use our software to measure various features that represent the morphological structure and distribution of second-phase particles on the binary images. The program detects the center of gravity, area, perimeter, and circumferential rectangle of each second-phase particle automatically, and measures the IMFP and the LN2D of each image. IMFP and LN2D are our originally developed methods to quantitatively analyze the distribution of second phase particles.

After the preprocessing, the data of extracted features, including histogram data and statistical data, will be used to train the model and a classifier will be used for the

classification. Histogram data is the relative frequency of the features, while statistical data is average values and standard deviation of the features. Two kinds of classifiers, SVM and random forest, were used in this work. Finally, we derive the accuracy of the classification by counting the number of correct ones in the test data as a percentage of the total.

### 4.2.3 Mechanical properties test

The tensile tests were carried out by a Shimadzu tensile testing machine with a load of 1000kgf at a stretching speed of 0.5mm/min. The dimensions of the tensile specimen are shown in the Fig. 4.1, which is a sheet tensile specimen with a thickness of 1 mm along the length of the rectangular specimen.

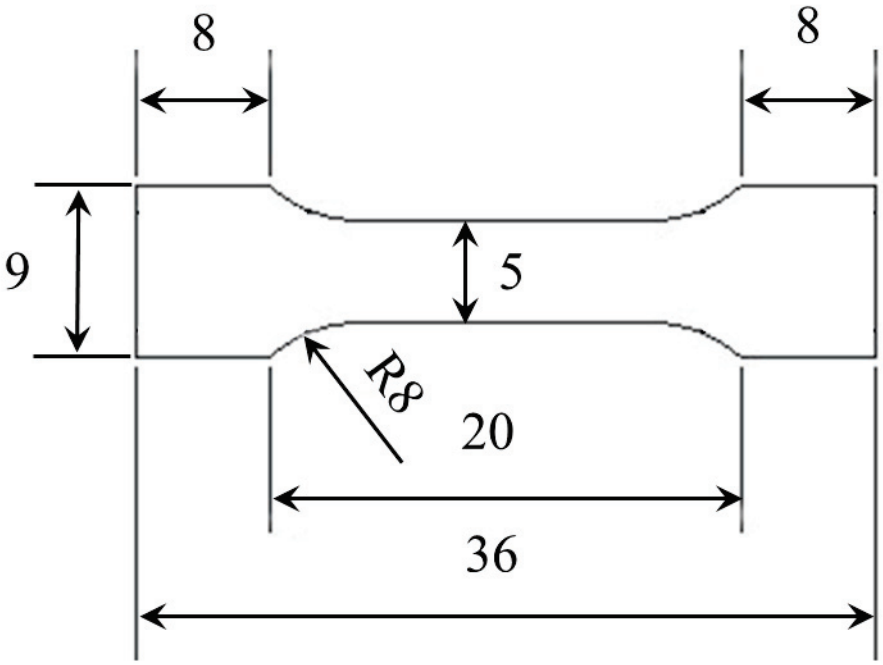


Fig. 4.1 The dimensions of the tensile specimen.

## 4.3 Results and Discussions

### 4.3.1 Microstructures

The Fig. 4.2 (a), (c) and (e) shown the microstructures of unmodified, 0.01% Sr and 0.02% Sr modified samples taken by optical microscopy in the magnification of 500 times, respectively. It could be noticed that more large areas of eutectic Si structures and finer eutectic Si particles could be found in the microstructures after modification. And the micrographs of the samples after binarization were shown in the Fig. 4.2 (b), (d) and (f), respectively. The black part of the binarized image was the aluminum matrix, and the white part was the second phase. It could be seen that the binarized image reproduced the morphological details of the second phase particles and their distribution in the matrix relatively well, which can extract feature quantities from binary images to describe the microstructural features more accurately.

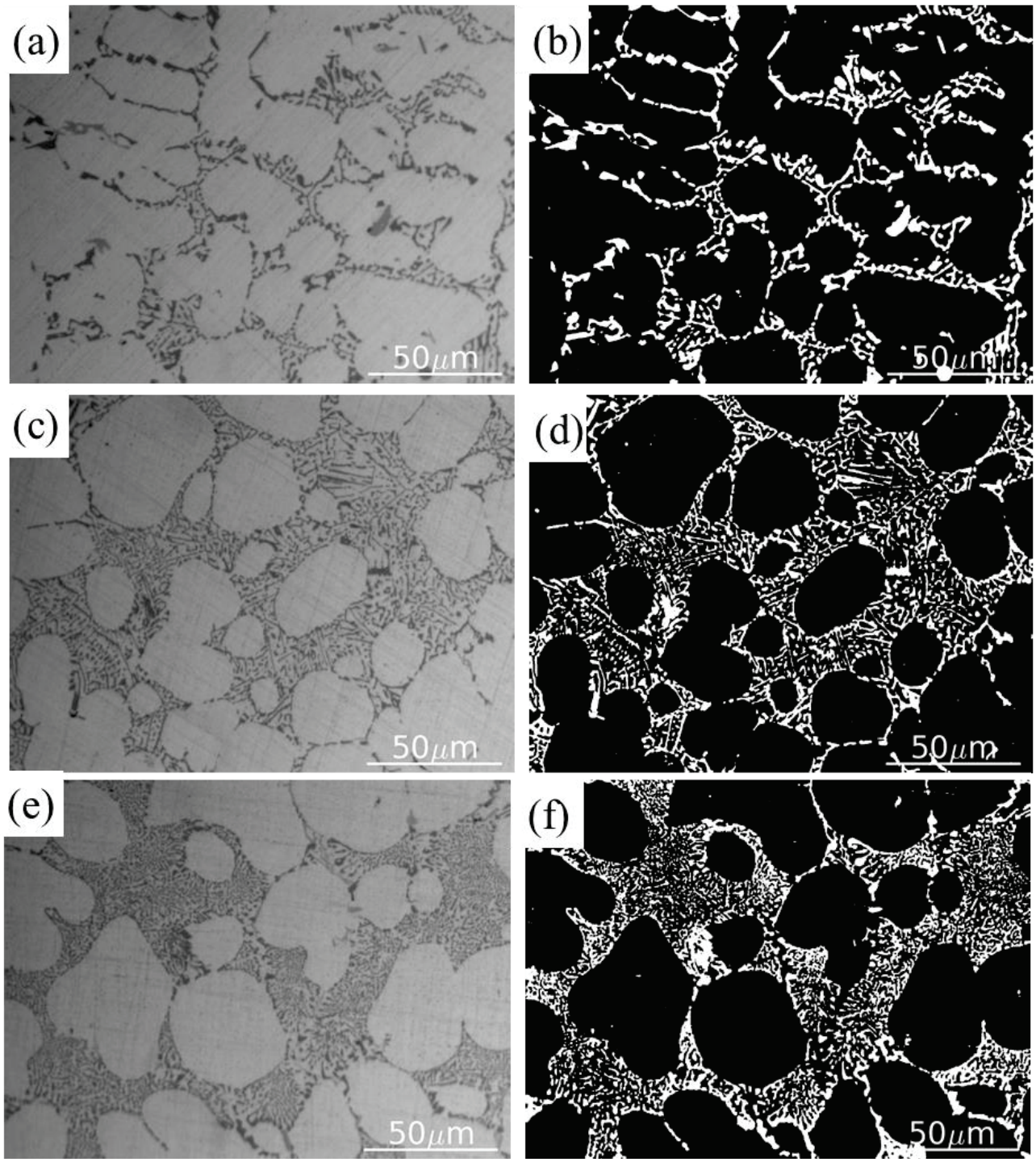


Fig. 4.2 The microstructural images and binarized images of the samples.

### 4.3.2 Classification

In our previous work,[18] we have concluded that 60-80 images using for training was suitable for this kind of material in machine learning process. More images in training data will spend more time on learning, especially on feature extraction process, which will lead to a decrement of machine learning efficiency.

The classification rates change of unmodified and Sr modified samples with number of images for training was tested, the number of which increased from 20 to 80. The results of random forest were shown in Fig. 4.3. It could be noticed that the data type (histogram or statistics) didn't have much effect on the accuracy, while the classification rates were increased with more images for training. It can be concluded that 60 was a suitable number for training to get the highest accuracy and efficiency. Therefore, the classification rates of modified samples were much lower than the rates between unmodified and modified ones. Classification rates of unmodified and modified samples reached 85% to 90% accuracy, but the rates of modified samples only reached 60% to 70% accuracy. The similarity of morphology and distribution of eutectic Si phase in the modified samples lead to no large difference of the features, which may be the reason caused the low accuracy of classification. The results of SVM when using the statistical data was shown in Fig. 4.4. The accuracy of 0.01%Sr modified and unmodified samples was still around 85% to 90%, but the classification rates of 0.02%Sr modified and unmodified samples reached the highest level in all the classification results.

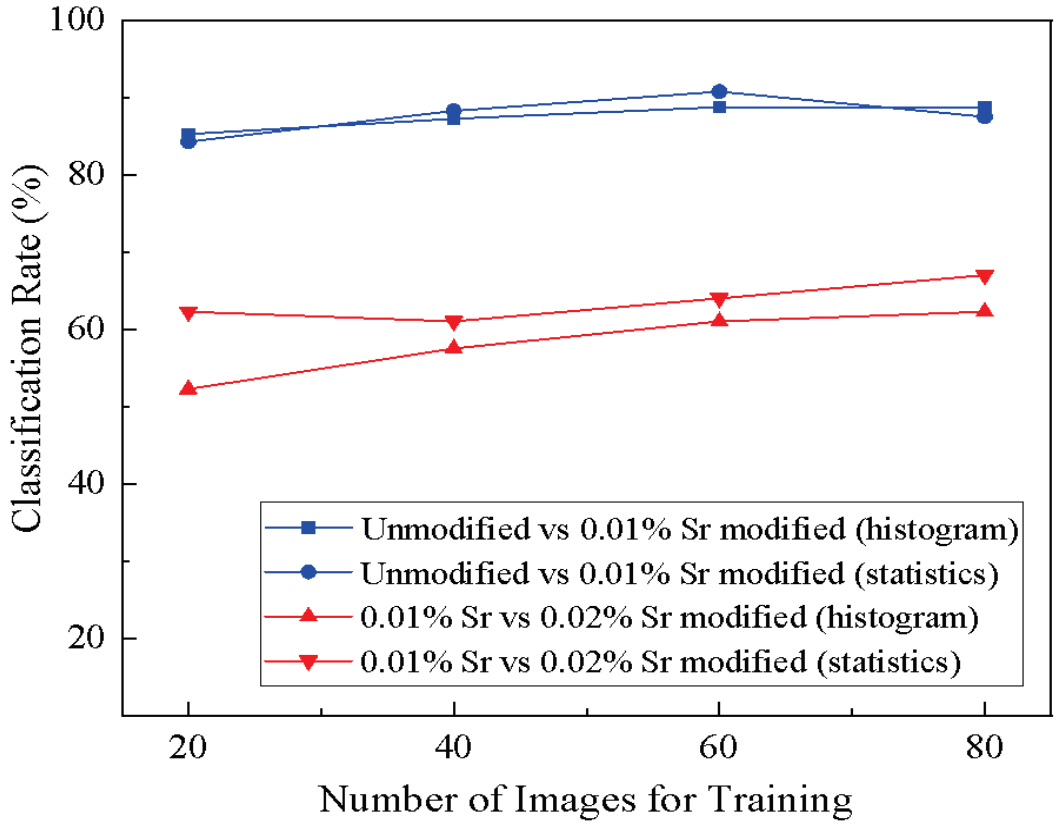


Fig. 4.3 The classification results of random forest.

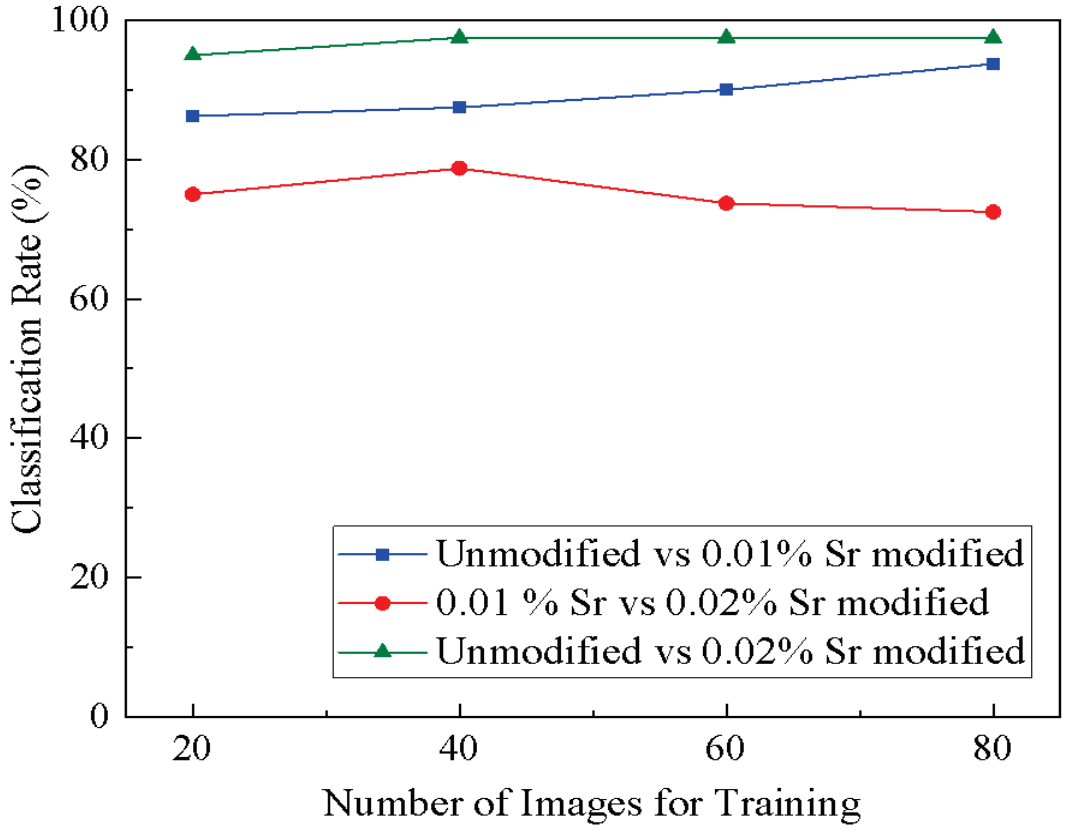

Fig. 4.4 The classification results of SVM using statistical data.

In order to more clearly compare the results obtained using the two classifiers, the classification results using 60 images for training were listed in Table 4.1. Although the classification accuracy of modified samples had increased when using SVM as classifier, it was still the lowest. The accuracy of classification between 0.01%Sr modified and unmodified samples slightly increased when using Random Forest as classifier, compared to the SVM results. Notably, when using statistical data, the SVM achieved an impressive 97.5% classification rate for unmodified and 0.02%Sr modified samples, which was the highest in all the classification results.

Table 4.1 The classification rates of the classifiers using different types of data, when using 60 images for training.

| Classifier | Modified sample | Histogram data | | Statistical data | |
|---|---|---|---|---|---|
| | | Unmodified | 0.01%Sr | Unmodified | 0.01%Sr |
| SVM | 0.01%Sr | 82.50 | — | 90.00 | — |
| | 0.02%Sr | 90.00 | 72.50 | 97.50 | 73.75 |
| Random Forest | 0.01%Sr | 88.75 | — | 90.75 | — |
| | 0.02%Sr | 90.00 | 61.00 | 89.75 | 64.00 |

### 4.3.3 PCA results and discussion

The results of PCA, the goal of which is to extract the most important information from the data table, were shown in Fig. 4.5. The results of PCA shown that $LN2DR_{var}$ (Variance of LN2DR) was the first principal component during the classification. This indicated that the spatial distribution of the second phase particles has an important effect on differentiating the microstructures of the samples before and after the modification. This is also consistent with previous observations on microstructural images.

Therefore, we used the training data to measure the values of $LN2DR_{var}$ for the three samples. Considering the effect of the modification on the refinement of the second-phase particles, we also measured the average values of Diameter, which is the equivalent circle diameter of the second phase particle, representing the particle size of eutectic Si in samples. The values of $LN2DR_{var}$ and average values of Diameter of the samples were shown in the Fig. 4.6. It could be easily found that the values of $LN2DR_{var}$ were increased with more additive of Sr.

Sr modification significantly increased the value of $LN2DR_{var}$, resulting in a large difference between the unmodified and modified samples. In contrast, for the modified samples, although the value of $LN2DR_{var}$ increases with more Sr additions, the overall difference is not significant, which leads to a lower level of classification rates for the modified samples. Besides, it can be found that this difference increased with the number of images used for measurement, and since $LN2DR_{var}$ was the first principal component during the classification, this could be the reason for the increment in classification accuracy with the increase in the number of images used for training.

From the measurement results of the Diameter average, it can be noticed that the modification did refine the size of the second phase particles, but the average size difference before and after the modification was less than one micron, which is too small compared to the huge difference that appears in the values of $LN2DR_{var}$, so the contribution of the feature values representing the size of the second phase particles to the classification is very small.

Usually there are 3 kinds of 2-dimensional arrangement types of the gravity centers,[19] the schematic diagram of which were shown in Fig. 4.7. During the measurement of LN2DR, the measurement circle will be located at a random point of the image, while the measurement will repeat at least one million times. The average value of LN2DR is always 7, and a lower variance value of which indicates a more uniform particle distribution. Fig. 4.7 (a) is a hexagonal closest ordering, that the distribution of particles is perfectly uniform, and in this situation, the value of $LN2DR_{var}$ equal to 0.5. And then the random distribution and clustering arrangement. The $LN2DR_{var}$ value of

clustering arrangement is higher than that of random distribution. It was found that the modification made the arrangement of the eutectic-Si particles from random to clustering distribution, which lead to an increment of $LN2DR_{var}$ value.

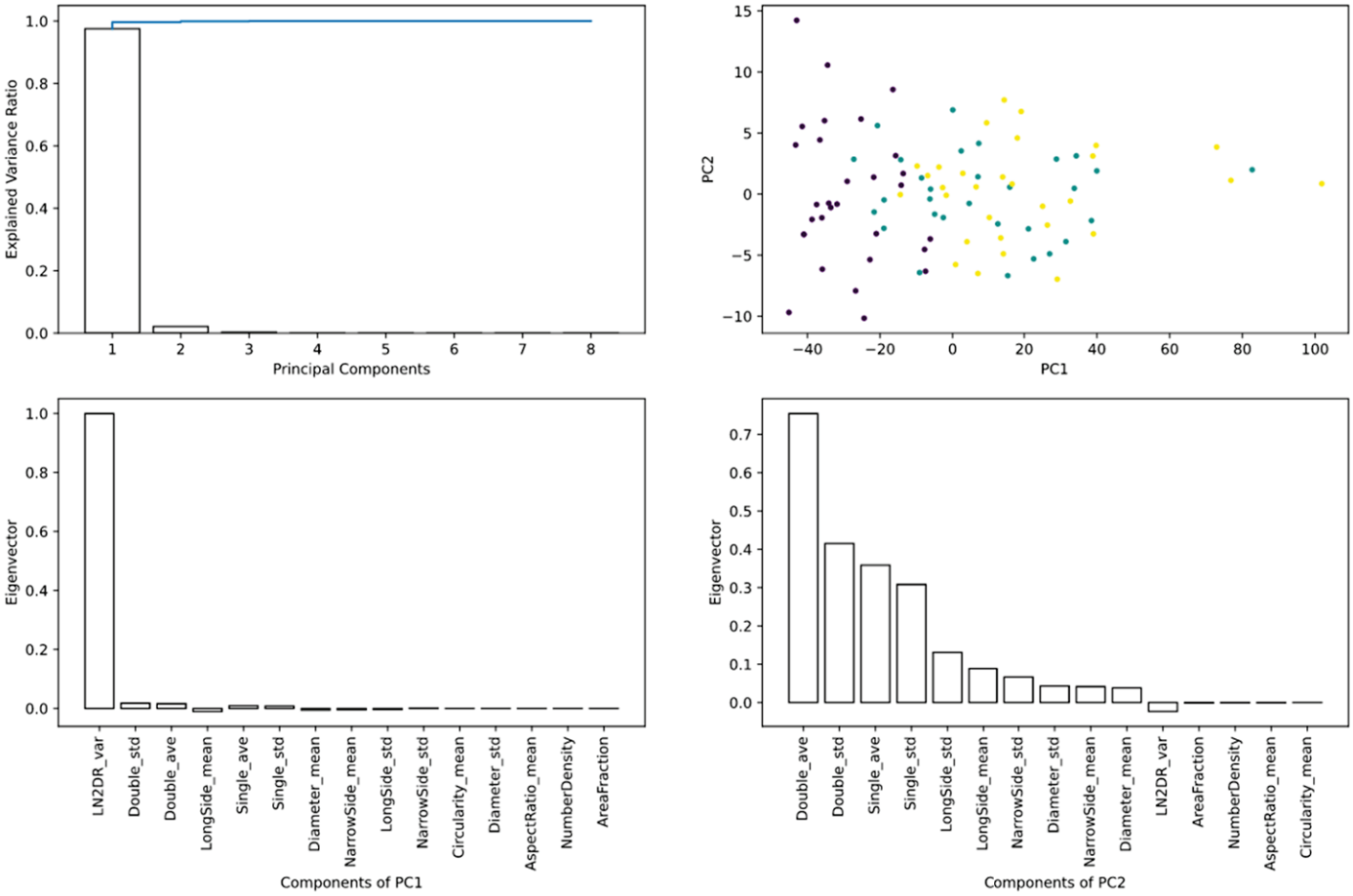


Fig. 4.5 The principal component analysis results of the samples, using 30 images of each sample.

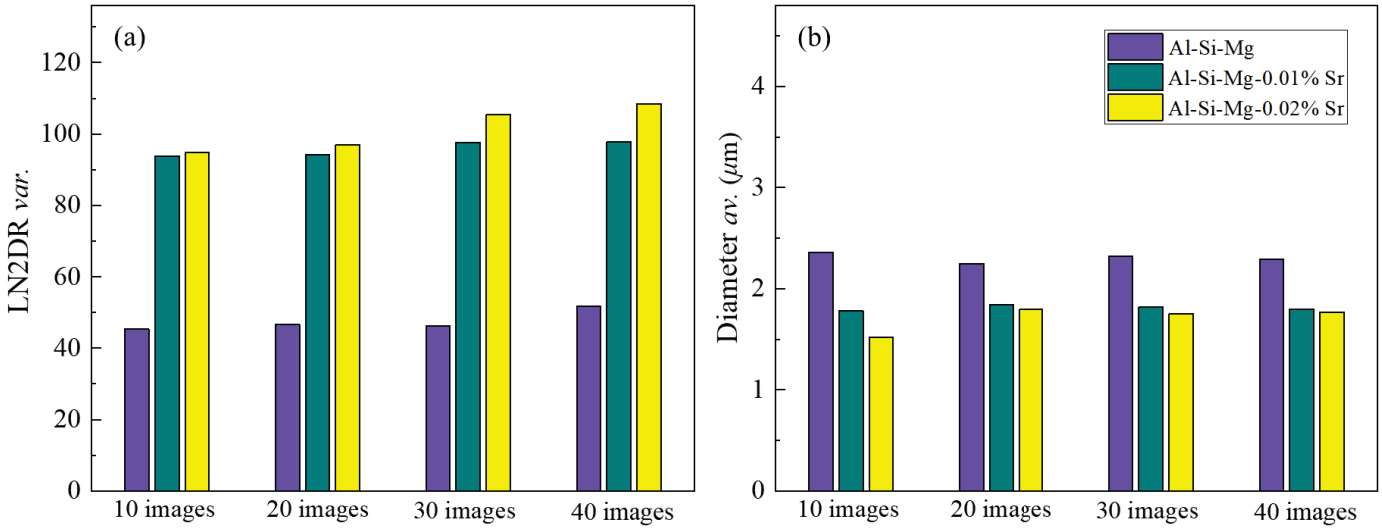


Fig. 4.6 Change of (a) LN2DR variance values and (b) average values of Diameter with the number of images for training.

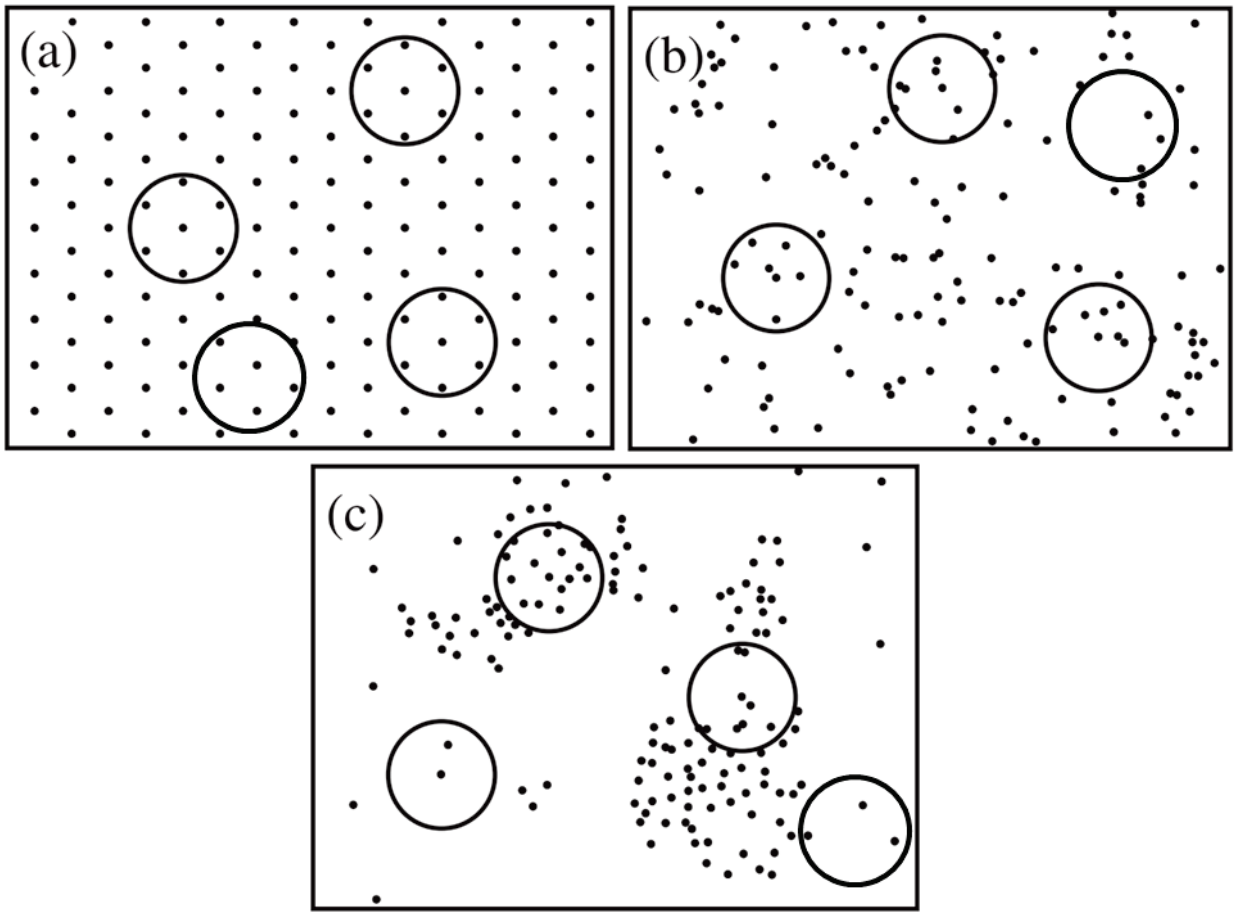


Fig. 4.7 Three 2-dimensional arrangement types of gravity center, (a) hexagonal closest ordering, (b) random and (c) clustering arrangement.

### 4.3.4 Tensile Properties

The stress-strain curves of the samples were shown in Fig. 4.8. After the modification, the tensile properties of the alloy were significantly increased. The tensile strength, 0.2% proof stress and elongation of the samples were shown in Fig. 4.9. All of these properties increased with more addition of Sr. The tensile strength increased over 100 MPa, and 0.2% proof stress increased about 50 MPa after modification. Besides, the elongation of the samples was even two to three times higher than before the modification. It indicated that Sr modification not only improved the tensile properties of the Al-Si-Mg casting alloy, but also greatly increased the ductility of the alloy, which is a greater advantage than work-hardening and other strengthening methods.

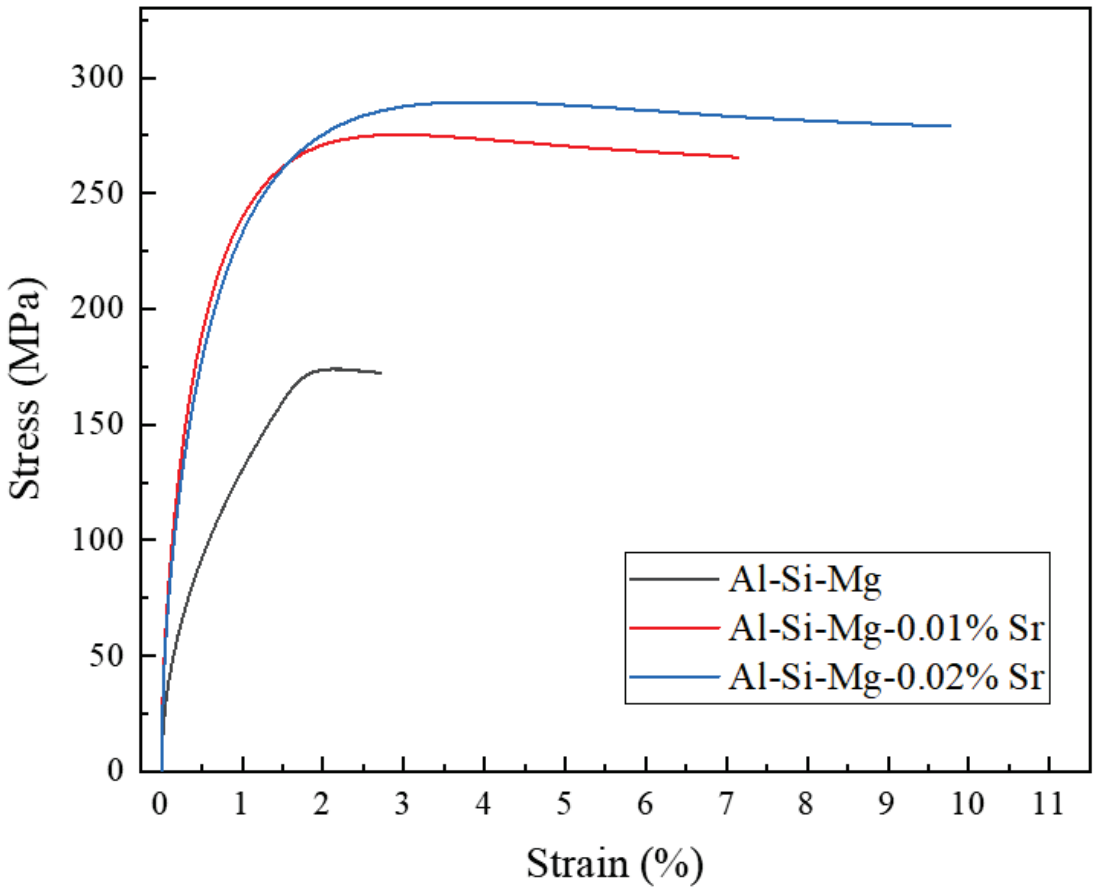


Fig. 4.8 Stress-strain curves of the samples.

### 4.3.5 Correlation between microstructural features and tensile properties

A database system that we are developing to integrate data from the processing parameter, microstructural features and properties of materials, with all the functionality previously developed, was used attempting to find a possible relationship between microstructural features and mechanical properties. Fig. 4.10 shown the correlation matrix for each parameter in this work. It was found that there was a strong correlation between $LN2DR_{var}$ to tensile properties, whose correlation rate was 0.7 of 1.0, and the correlation rate between mean of Diameter and tensile properties was 0.5 of 1.0. The minimum and average values of Diameter were negatively correlated with the tensile properties, which means that the finer the size of the second phase can improve the tensile properties of the alloy. The role of Sr modification is to refine the eutectic silicon phase to improve the mechanical properties of the Al-Si casting alloy. So, this result is consistent with the experimental results. And $LN2DR_{var}$ is positively correlated with the tensile properties, because $LN2DR_{var}$ is the first principal component and increased with the addition of Sr, which is consistent with the increase of tensile properties. However, it is still worth discussing and further investigating about why the increase of $LN2DR_{var}$ lead to the enhancement of tensile properties.

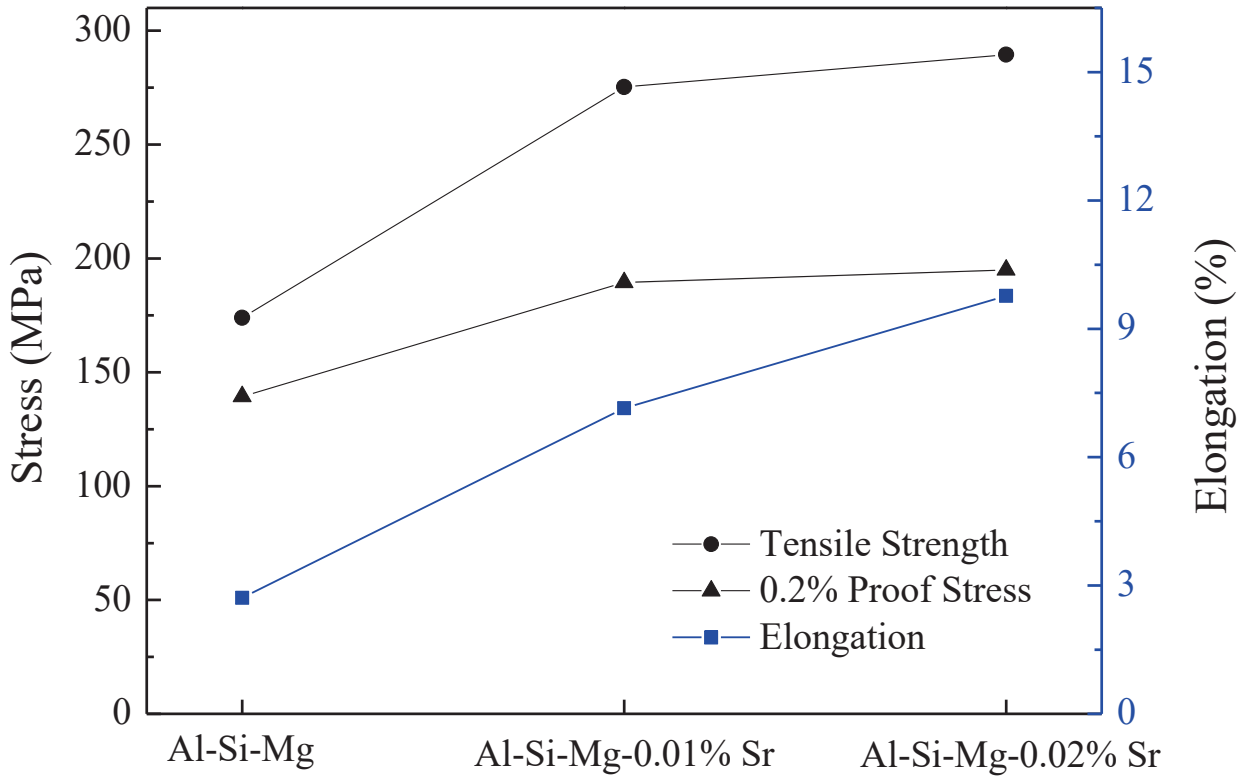


Fig. 4.9 The tensile properties of unmodified and Sr modified samples.

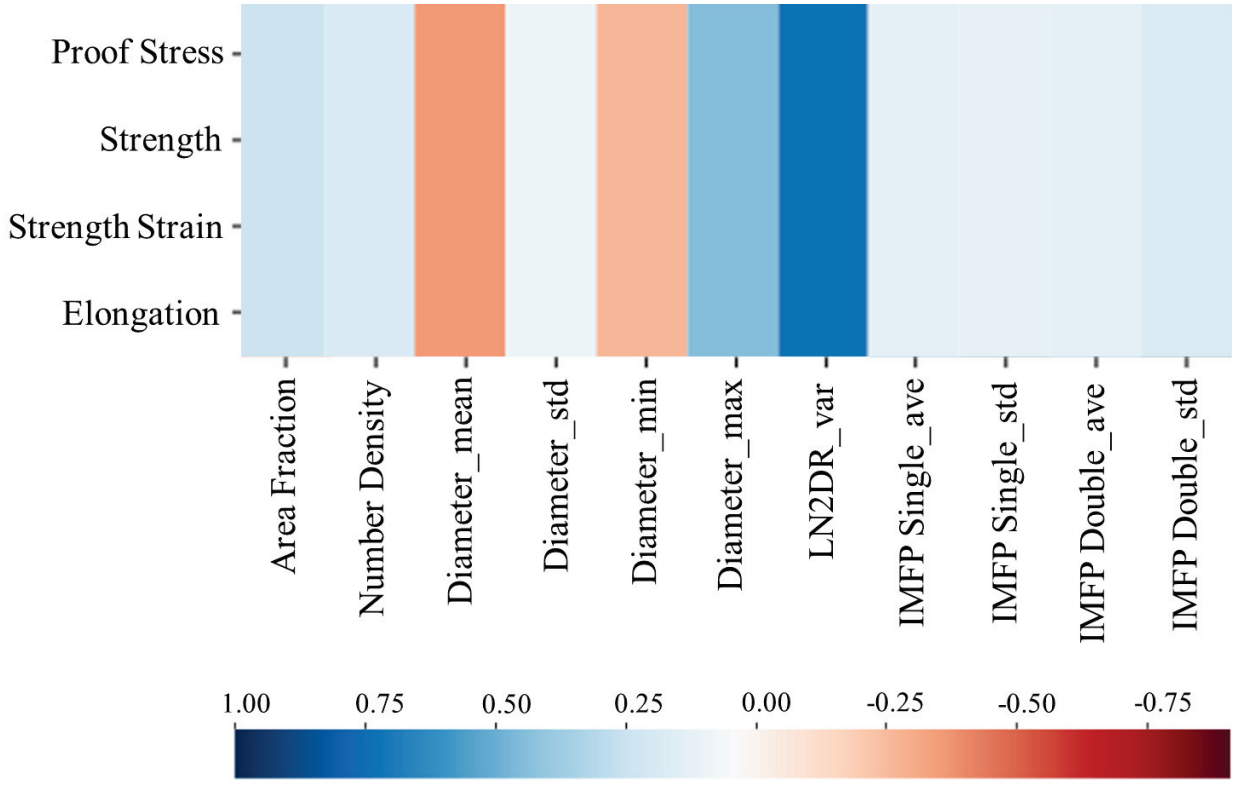


Fig. 4.10 The correlation matrix of the microstructural features and mechanical properties.

## 4.4 Summary

In this chapter, the Al-7%Si-0.3%Mg casting alloys (wt%) were solidified and modified with the additive of Sr. The microstructural classification of the samples and quantitative analysis of the eutectic Si-phase changes before and after modification were accomplished by machine learning-based image classification techniques. The results were summarized as follows.

(1) The large areas of eutectic-Si structure and finer eutectic-Si particles could be found in the microstructures of the samples after modification.
(2) The classification rate of unmodified and 0.02% Sr modified samples reached the highest point of 97.5% accuracy when using the statistical data and SVM as classifier. The results of PCA shown that LN2DRvar was the first principal component during the classification, which indicated the importance of second phase distribution on differentiating the microstructures of the samples before and after the modification. The modification changed the arrangement of the eutectic-Si particles from random to clustering distribution, which lead to a significantly increment of LN2DRvar value.
(3) The tensile properties of the samples were significantly increased after modification because of the refinement effect of Sr to the eutectic-Si phase. Therefore, the feature Diameter was negatively correlated to tensile properties. The feature LN2DRvar was the first principal component and increased with more addition of Sr, which reflected the distribution change of eutectic Si phase before and after Sr modification. However, it is still worth discussing and further investigating about why the increase of LN2DRvar lead to the enhancement of tensile properties.

## Reference


1) H. Ye, *Journal of Materials Engineering and Performance*, 2003, **12**, 288-297.

2) S. Kumai, J. Hu, Y. Higo and S. Nunomura, *Keikinzoku*, 1995, **45**, 198-203.

3) A. Mazahery and M. O. Shabani, *Jom*, 2014, **66**, 726-738.

4) N. Fatahalla, M. Hafiz and M. Abdulkhalek, *Journal of Materials Science*, 1999, **34**, 3555-3564.

5) S. Farahany, A. Ourdjini, M. Idrsi and S. Shabestari, *Thermochimica Acta*, 2013, **559**, 59-68.

6) O. Uzun, F. Yılmaz, U. Kölemen and N. Başman, *Journal of alloys and compounds*, 2011, **509**, 21-26.

7) M. Haque and M. Maleque, *Journal of Materials Processing Technology*, 1998, **77**, 122-128.

8) S. Derin, U. Aybarç and Y. Birol, *International Journal of Metalcasting*, 2017, **11**, 688-695.

9) M. Timpel, N. Wanderka, G. V. Kumar and J. Banhart, *Ultramicroscopy*, 2011, **111**, 695-700.

10) Q. Wang and C. Davidson, *Journal of materials science*, 2001, **36**, 739-750.

11) B. Closset and J. Gruzleski, *Metallurgical Transactions A*, 1982, **13**, 945-951.

12) M. Timpel, N. Wanderka, R. Schlesiger, T. Yamamoto, N. Lazarev, D. Isheim, G. Schmitz, S. Matsumura and J. Banhart, *Acta Materialia*, 2012, **60**, 3920-3928.

13) G. Mao, H. Yan, C. Zhu, Z. Wu and W. Gao, *Journal of Alloys and Compounds*, 2019, **806**, 909-916.

14) C. Xu, Q. Jiang, Y. Yang, H. Wang and J. Wang, *Journal of alloys and compounds*, 2006, **422**, L1-L4.

15) K. Nogita, S. D. McDonald and A. K. Dahle, *Materials Transactions*, 2004, **45**, 323-326.

16) J. Li, X. Wang, T. Ludwig, Y. Tsunekawa, L. Arnberg, J. Jiang and P.

Schumacher, *Acta Materialia*, 2015, **84**, 153-163.

17) K. Nogita, H. Yasuda, M. Yoshiya, S. McDonald, K. Uesugi, A. Takeuchi and Y. Suzuki, *Journal of Alloys and Compounds*, 2010, **489**, 415-420.

18) Z. Qiu, K. Sugio and G. Sasaki, *Materials transactions*, 2021, MT-MBW2020002.

19) D. Zhang, K. Sugio, K. Sakai, H. Fukushima and O. Yanagisawa, *Materials Transactions*, 2007, **48**, 171-177.

# *Chapter 5*

# Conclusions

The final purpose of the present research is to develop a system that uses machine learning to analyze the interrelationships among processes, microstructures, and material properties. This study focuses on microstructural analysis with the help of machine learning techniques, in order to help improve the accuracy and efficiency of this process. In this study, we attempted to classify the microstructures of Al-Si casting alloy at different stages of the T6 heat treatment process, Al-Si alloy casting at different cooling rates, and after Sr modification treatment by machine learning techniques, and quantitatively analyze the morphology and distribution of eutectic Si-phase particles using our originally developed methods. The conclusions of this thesis are summarized as follows:

1. The study on microstructural classification of Al-Si casting alloy after aging treatment (Chapter 2).

A machine learning-based image classification technique was attempted to be applied to the classification of microstructures of Al-4 %Si-0.5 %Mg alloy at each stage of the T6 heat treatment process. A classification rate of 100% accuracy was obtained when comparing the microstructures from the casting and other T6 process stages. The feature values that contributed significantly to the classification were the average value and standard deviation of IMFP. This is because the solution treatment causes the eutectic Si-phase to become spherical that leading to the increase of the IMFP value, which is the free path length. In the case of classification using SVM, the classification rate was generally higher when statistical data were used. This is thought to be due to

overlearning when the histogram data (frequency distribution of the features) is applied. Comparing the algorithms used for classification, the classification rate was higher when Random Forest was used as a classifier than SVM.

2. The study on microstructural classification of Al-Si alloy casting at different cooling rates (Chapter 3).

The Al-7%Si-0.3%Mg alloys were solidified in a copper mold at three different cooling rates. The microstructures of the samples were similar because of the approximate cooling rates, so originally developed machine learning-based image classification techniques were used to detect the difference between the microstructures of the samples. The mechanical properties of the three samples were slightly increased with the increase of cooling rates, proving the differences between the samples.

The classification of the microstructures was accomplished by using machine learning techniques, and high classification rates of about 80% to 90% were obtained. The classification rate was highest when using the statistical data and using SVM as classifier. Besides, the classification rate was higher when the difference of cooling rates of samples was bigger. In order to get the highest classification rate in shortest time, a suitable number of images for training was 60 to 80 during the machine learning process in this study.

3. The study on microstructural classification of unmodified and strontium modified Al-Si casting alloys (Chapter 4).

The Al-7%Si-0.3%Mg casting alloys (wt%) were solidified and modified with the additive of Sr. The microstructural classification of the samples and quantitative analysis of the eutectic Si-phase changes before and after modification were accomplished by machine learning-based image classification techniques. The large areas of eutectic-Si structure and finer eutectic-Si particles could be found in the microstructures of the samples after modification.

The classification rate of unmodified and 0.02% Sr modified samples reached the highest point of 97.5% accuracy when using the statistical data and SVM as classifier. The results of PCA shown that LN2DRvar was the first principal component during the

classification, which indicated the importance of second phase distribution on differentiating the microstructures of the samples before and after the modification. The modification changed the arrangement of the eutectic-Si particles from random to clustering distribution, which lead to a significantly increment of LN2DRvar value.

The tensile properties of the samples were significantly increased after modification because of the refinement effect of Sr to the eutectic-Si phase. Therefore, the feature Diameter was negatively correlated to tensile properties. The feature LN2DRvar was the first principal component and increased with more addition of Sr, which reflected the distribution change of eutectic Si phase before and after Sr modification. However, it is still worth discussing and further investigating about why the increase of LN2DRvar lead to the enhancement of tensile properties.

# Papers and Proceedings

1. **Zixiang Qiu,** Kenjiro Sugio*, and Gen Sasaki. Classification of Microstructures of Al–Si Casting Alloy in Different Cooling Rates with Machine Learning Technique, Materials Transactions, Vol. 62 (2021), No. 6 pp. 719-725. (Chapter 3)
2. **Zixiang Qiu**, Kenjiro Sugio, Gen Sasaki. Microstructural Classification of Unmodified and Strontium Modified Al-Si-Mg Casting Alloys with Machine Learning Techniques. 17th Japan International SAMPE Symposium and Exhibition (JISSE-17), December 1-3, 2021, Tokyo, Japan. (Chapter 4)
3. **Zixiang Qiu**, Kenjiro Sugio*, and Gen Sasaki. Microstructural Classification of Unmodified and Strontium Modified Al-Si-Mg Casting Alloys with Machine Learning Techniques, Materials Transactions, Vol. 64 (2023), No. 1 pp. 171 to 176. (Chapter 4)

# Presentations

1. **Zixiang Qiu**, Kenjiro Sugio, Gen Sasaki. Microstructural Classification of Unmodified and Strontium Modified Al-Si-Mg Casting Alloys with Machine Learning Techniques. 17th Japan International SAMPE Symposium and Exhibition (JISSE-17), December 1-3, 2021, Tokyo, Japan.
2. **Zixiang Qiu**, Kenjiro Sugio and Gen Sasaki. Classification of Microstructures of Al-Si-Mg alloys with Machine Learning Technique. 2019 年 8 月 第 11 回 軽金属学会 中国四国支部 講演大会 岡山, 日本.
3. **Zixiang Qiu,** Kenjiro Sugio, Gen Sasaki. Classification of Microstructures of Al-Si Casting Alloy in Different Solidification Rates with Machine Learning Technique. 2020 年 9 月 日本金属学会 秋期講演大会 Web 開催.
4. **Zixiang Qiu,** Kenjiro Sugio, Gen Sasaki. Microstructural Classification of Unmodified and Strontium Modified Al-Si-Mg Casting Alloys with Machine Learning Techniques. 2021 年 9 月 日本金属学会 秋期講演大会 オンライン開催.
5. **Zixiang Qiu,** Kenjiro Sugio, Gen Sasaki. Microstructural Classification of Sr Modified Al-Si-Mg Casting Alloy Solidified at Different Cooling Rates with Machine Learning Techniques. 2022 年 3 月 日本金属学会 春期講演大会 東京大学駒場キャンパス、ポスターセッション(オンライン開催).

# Acknowledgement

First of all, I would like to give my thanks to Hiroshima University, for the Higashihiroshima Campus with its beautiful natural environment, complete facilities, and lovely staff. I spent my doctoral period in an inclusive, rigorous, and international academic atmosphere. I would like to thank JASSO and Kumahira Co., Ltd. for providing me with the scholarship. Additionally, I would like to thank the Japanese government and the Japanese private sector for the various grants given during the epidemic of COVID-19. Without these supports, it would have been no easy to complete my doctoral dissertation.

I would like to show my deepest gratitude to my supervisor, Associate Professor Kenjiro Sugio, who has provided me with valuable guidance in every stage of the writing of this thesis. He gave me great help to overcome all the difficulties during the research. Without his enlightening instruction, impressive kindness and patience, I could not have completed my thesis. In addition, he gave me a lot of opportunities to present my research which is a valuable experience in my life and gives me the confidence to face the coming challenge.

I am also greatly indebted to Professor Gen Sasaki, for providing me with many valuable comments during my doctoral period, which were of great help to my doctoral dissertation. Next, I would like to express my heartfelt thanks to Professor Kazuhiro Matsugi, Associate Professor Yongbum Choi, and Associate Professor Zhefeng Xu for their useful advice on this thesis.

Then, my thanks are extended to the past and present students of the Material Physics Laboratory, especially Tomoki Katayama, Yan Zhao, and Wenchuang Liu, for their enthusiastic help to me. And my special thanks to my good friend Ruiqiang Wang, who helped me a lot in modifying my thesis.

Last but not least, my gratitude also extends to my family for their endless love and selfless support, and to my girlfriend for her selfless company and encouragement during the writing of this thesis. Without them, I would not have made it this far in my education.